Transport Behavior of Tailored Carbon Nanomembranes

Dissertation

Faculty of Physics
Bielefeld University

submitted by

Raphael Dalpke

Bielefeld, July 20, 2020

Committee

Prof. Dr. Armin Gölzhäuser
Prof. Dr. Dario Anselmetti

Dedicated to the beloved ones whose time had already come

Acknowledgements

First of all, I want to thank Prof. Dr. Armin Gölzhäuser for giving me the opportunity to explore the fascinating topic of carbon nanomembranes under his supervision.

I appreciate that Prof. Dr. Dario Anselmetti was willing to be the second reviewer of the present thesis.

PD Dr. André Beyer guided me through my doctoral studies. His door was open at all times and I could always rely on his unconditional support. Thank you.

The contributions of Dr. Berthold Völkel with his efforts to maintain the equipment and to solve the daily (technical) issues were indispensable for the success of this thesis. Beside that he took care of my physical well-being by providing the buns for our weekly breakfast on Fridays, which served as a casual gathering for (scientific) discussions.

Further I want to express gratitude to my cooperation partners, especially Prof. Dr. Karl-Josef Dietz and Anna Dreyer from Plant Biochemistry and Physiology of the Faculty of Biology of Bielefeld University as well as Nicole Wutke from the Max Planck Institute for Polymer Research in Mainz, without whom many of the presented results would not have been possible.

I appreciated the support and advice of Dr. Nikolaus Meyerbröker from CNM Technologies GmbH during my time in the laboratory. Sometimes it was necessary to speak in the same language from chemist to chemist to address a particular problem.

Special thanks to Riko Korzetz who was always available for inspirational conversations and patient when teaching me “some” physics and mathematics - even after the eighth hour had already passed.

Dr. Daniel Emmrich and Dr. Yang Yang were always there to help me with their expertise concerning the HIM or the permeation measurements. Thanks a lot.

A pleasant working atmosphere is vital to succeed. My office crew, the complete working group of Physics of Supramolecular Systems and Surfaces, and our former secretary Karin Lacey gave me the feeling to be part of one big (research) family. I really enjoyed my time in the group and I will not forget it.

Of course I want to express gratitude to my family, friends, and especially to M, who encouraged me to stay on track and not to surrender even when my motivation touched the bottom.

Last but not least, I would like to thank all those whom I have inadvertently missed to mention. Please forgive me.

Contents

1. Introduction to the Thesis

According to the United Nations, the earth was populated by 7.7 billion people in the middle of the year 2019. Although the world's population growth rate declined to 1.1 per cent per year in the time period of 2015 to 2020 and it is predicted to continuously drop even further, the majority - meaning 52 % - of the population increase between 2019 and 2050 is believed to occur in countries of sub-Saharan Africa, which will have the largest population until the end of this century. [1] Consequently, there will be an emerging demand on both water [2] and energy. In 2019, the Africa Energy Outlook published by the International Energy Agency already pointed out that by 2040 additional 580 million Africans will move from the countryside into the cities further pushing the urbanization and thus the energy consumption of the continent. Considering the anthropogenic climate change, it would be reasonable to cover as much as possible of the arising demands by sustainable and energy-efficient processes. [3]

This brief excursion underlines the importance of the development of appropriate technologies and materials. One way to improve the performance of existing processes is to incorporate membranes with certain properties. [4] In the so-called field of membrane separation processes [5], the nanometer-thin and mechanically stable carbon nanomembranes [6] are promising candidates for an efficient usage. The range of the permeating species and the performance of the membrane itself are predetermined by the original structure of the chosen precursor molecule [7], which is utilized for the formation of the carbon nanomembrane. The semipermeable carbonaceous membrane combines an outstanding water permeance with a high selectivity. [8] Besides water, only a limited amount of other gases or vapors are able to pass through the carbon nanomembrane, whereas ions are rejected. [8–10] This property makes the carbon nanomembrane attractive for instance to produce drinking water in a more energy-efficient way.

The objectives of the present thesis are to find new ways to alter and monitor the properties of carbon nanomembranes in order to facilitate the screening for efficient custom-made separation membranes. Therefore, it was investigated how well-known carbon nanomembranes can be functionalized with proteins in order to alter their properties. Furthermore, the application of radioactive tracers to characterize the membrane's selectivity in aqueous solutions was explored to provide a reliable and sensitive method for monitoring the permeating compounds through carbon nanomembranes. Additionally, structurally different molecular building blocks were utilized for the fabrication of carbon nanomembranes to expand the knowledge of the available set of precursor molecules and thus to gain access to different membranes' properties.

The present thesis has three chapters treating the needed scientific background knowledge. First, the carbon nanomembranes themselves are introduced and subsequently some fundamental descriptions for transmembrane separation processes are given. To allow the reader to follow the conducted experiments, the utilized instruments and techniques are outlined. The subsequent three result chapters present the findings of the performed investigations, where each chapter deals with one of the three aforementioned different issues with respect to carbon nanomembranes. Every single chapter is going to introduce the respective current state of research and provides a summary of the results independently from each other in order to guarantee clarity. The main part is going to be finalized by the overall conclusion and outlook of the thesis.

2. From Molecular Self-Assembly to Carbon Nanomembranes (CNMs)

The term self-assembly covers, generally speaking, the spontaneous and convergent formation of an organized arrangement from a disordered system resulting from the specific and local interactions between its individual components. Self-assembly occurs over eight orders of magnitude ranging from the centimeter to ångström scale in dispersive systems down to quantum dots. [11, 12]

The phenomenon of molecular self-assembly deals, as already indicated by the name, with the assembly of molecules in the nanometer range. [12] Bigelow *et al.* [13] reported the formation of oleophobic films on surfaces from solution back in 1946. However, it took nearly four decades until the self-assembled monolayers (SAMs) attracted great interest. Today, SAMs have been intensively studied, those made from alkanethiolates on gold being the most prominent example. [14] The general structure of a densely-packed SAM is given in figure 2.1. The precursor molecules consist of three different parts: A surface-active head group, which is primarily responsible for the binding to the surface, a spacer, which defines the thickness and the intrinsic properties of the SAM, and a terminal group, which governs the self-assembled monolayers' surface properties. [14, 15] One excellent overview on the numerous different SAM systems is given by Love *et al.* [15]. Self-assembled monolayers have a wide applicability in the fields of device development, material science and nanotechnology ranging from fundamental research to the manipulation of properties and the construction of nanomaterials. [14–19]

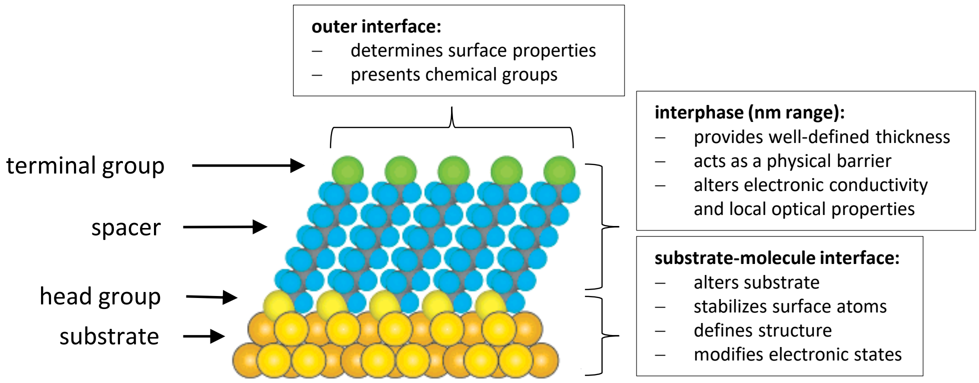

Figure 2.1.: Generalized illustration of an ideal self-assembled monolayer using the example of alkanethiolates on Au(111). The anatomy and characteristics of the SAM are highlighted. Reprinted and adapted with permission from Love *et al.* [15]. Copyright 2005 American Chemical Society. Adaptions taken from Turchanin and Gölzhäuser [20].

In 2005 Eck *et al.* [21] reported the fabrication of free-standing nanosheets made from aromatic self-assembled monolayers. After the formation process the supported monolayer was irradiated with low energy electrons (100 eV) leading to cross-linking between the precursor molecules and thus to the generation of a nanosheet as displayed in figure 2.2 . Later, in 2010, those nanosheets were termed carbon nanomembranes (CNMs). [22] The development of a generalized route for the fabrication of CNMs [7] and a suitable transfer protocol [22, 23], which enables the transfer to any arbitrary material, pushed the investigation of this novel molecularly thin material. The investigation of the mechanical [23–25] and electrical properties [26–29] of carbon nanomembranes characterize it as a stable and insulating material. Furthermore, CNMs can be converted to nanocrystalline graphene. [30–33] These qualities make carbon nanomembranes a promising candidate for sensory and electronic devices. CNMs also exhibit chemical resistance [34]. By utilizing precursor molecules with specific chemical moieties, the possibility of further chemical functionalization [34–38] is given. Consequently, carbon nanomembranes can serve as templates for a subsequent synthesis on a nanometer scale. The determination of the permeation of gaseous and liquid substances through CNMs reveal its potential use in separation processes. [8–10, 39–42] For obtaining a further overview of the research on carbon nanomembranes it is referred to the reviews from Turchanin and Gölzhäuser [6, 20].

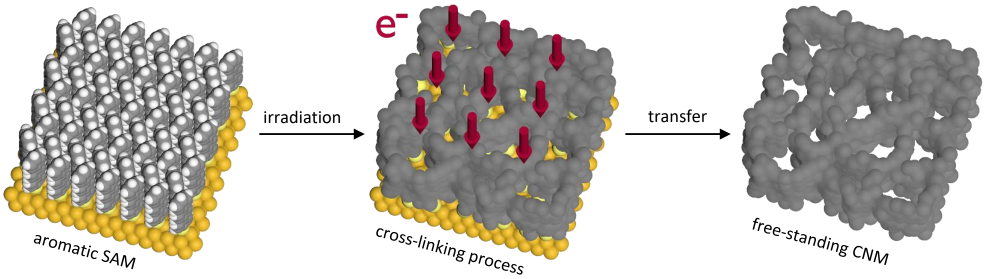

Figure 2.2.: An aromatic SAM is irradiated with low energy electrons and cross-links to a CNM, which can be detached from the surface and transferred to an arbitrary substrate. Reprinted and adapted from Yang *et al.* [10]. Copyright 2020. Published by Wiley-VCH Verlag GmbH & Co. KGaA, Weinheim.

The occurring processes during the formation of a CNM are still not completely clarified, but it is believed that the cross-linking is dominated by dissociative electron attachment (DEA). In figure 2.3 the major steps are shown. Secondary electrons are ejected due to the irradiation with either electromagnetic radiation, ions or electrons. By capturing an electron, the precursor molecule forms a transition negative ion, which leads to the rupture of C-H bonds. Cross-linking with a neighbor molecule follows and self-quenching occurs. [43]

However, the existence of a stable carbon nanomembrane as shown in figure 2.4 is only reported for self-assembled monolayers from aromatic building blocks although recently Neumann *et al.* [44] successfully obtained CNMs by utilizing hybrid aliphatic-aromatic precursor molecules. Waske *et al.* [45] inves-

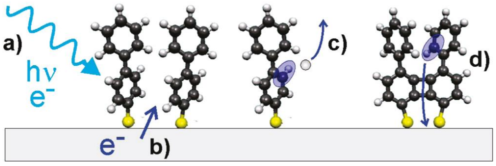

Figure 2.3.: Schematic representation of the different steps involved in the cross-linking of aromatic SAMs: (a) irradiation, (b) emission of secondary electrons, (c) dissociation of C-H bonds, (d) self-quenching of electronically excited partially linked molecules. Reprinted with permission from Turchanin *et al.* [43]. Copyright 2009 American Chemical Society.

tigated the cross-linking of aliphatic, cycloaliphatic and aromatic SAMs and compared their respective resist properties. The experiments indicated that the cyclic nature of the molecules is the key characteristic to balance the cross-linking and defragmentation during the irradiation process. Several studies on linear aliphatic precursor molecules were done but they were all ambiguous as to whether a stable network could be formed. [46–49] Even though Schmidt *et al.* [50] reported the conversion of an alkanethiolate SAM on a gold surface into "*a 'sealed', extensively cross-linked, chemically inhomogeneous hydrocarbon film*" (reprinted with permission from Schmidt *et al.* [50]. Copyright 2019 American Chemical Society.) in 2019, so far no attempts were made to examine the possible existence of carbon nanomembranes on the basis of these findings.

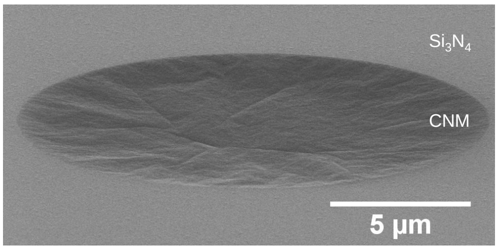

Figure 2.4.: Helium ion microscopic image (secondary electron mode, tilt angle: ∼ 75°) of a free-standing CNM suspended over an orifice in the Si_3N_4 support. Reprinted and adapted with permission from Yang *et al.* [8]. Copyright 2018 American Chemical Society.

3. Fundamentals of Transmembrane Separation Processes

In this chapter some basic theories with respect to transport across membranes and related characteristics are abridged. First, the essential concept of diffusion is presented. Two mechanisms which are relevant for the present thesis - namely the Knudsen diffusion and Weber's disc - are outlined. The second section deals with quantities which are commonly related in the description of transmembrane separation processes.

3.1. Diffusion

Above absolute zero temperature the entropy-driven random molecular motion spatially transporting matter within a system to approach an uniform equilibrium state is called diffusion. [51, 52] Mathematical descriptions of this phenomenon in dilute and isotropic substances are given by Fick's laws of diffusion. In one dimension, the first law as shown in equation (3.1) states that the flux F is proportional to the concentration gradient of the diffusing substance along one spatial direction $\partial C/\partial x$. The constant of proportionality D is denoted as the diffusion coefficient. The negative algebraic sign is caused by the fact that diffusion occurs in the opposite direction of the concentration gradient. [52]

$$F = -D\frac{\partial C}{\partial x} \tag{3.1}$$

Displayed in equation (3.2), Fick's second law of diffusion relates the temporal change of the concentration $\partial C/\partial t$ with the second derivative of the concentration's one-dimensional location dependence $\partial^2 C/\partial x^2$ assuming a constant diffusion coefficient. [52]

$$\frac{\partial C}{\partial t} = D\frac{\partial^2 C}{\partial x^2} \tag{3.2}$$

3.1.1. Knudsen Mechanism

Considering defined geometries and conditions, Fick's laws of diffusion can be applied to different issues. Assuming that the molecules' mean free path is much greater than the diameter of a straight and cylindrical pore, the diffusion can be described by the Knudsen mechanism. If the length of the pore is much larger than the pore's diameter, the Knudsen diffusion coefficient D_K and accordingly the flux F are directly linked with the square root of the inverse molar mass M as shown in equation (3.3). The absolute temperature, the radius of the pore, and the gas constant are represented by T, r, and R, respectively. [51]

$$F \sim D_K = r\sqrt{\frac{32RT}{9\pi M}} \tag{3.3}$$

If the length of the pore is much smaller than the pore's diameter, the escape of matter through an orifice into the vacuum also depends on the square root of the inverse molar mass, which is in accordance with Graham's law of effusion. Assuming an ideal gas, the rate of effusion Φ_{eff} in equation (3.4) is simply the product of the collision flux Z_W and the area A_0 of the hole. The Avogadro constant is indicated by N_A and the pressure by p. [53]

$$\Phi_{\text{eff}} = Z_W A_0 = \frac{p\,N_A\,A_0}{\sqrt{2\pi M\,RT}} \tag{3.4}$$

3.1.2. Weber's Disc

In aqueous solutions Fick's second law of diffusion can be applied to characterize the position-dependent concentration through an orifice in a thin film as illustrated in figure 3.1. Originally known as Weber's disc, it described the electric field around a disc-shaped electrode. For the treatment of the opening the diffusion's law is expressed in cylindrical coordinates using the variables r and z. The boundary conditions in equation (3.5) were used to derive the expression for calculating the position-dependent concentration C as shown in equation (3.6). The bulk concentration is represented by C_0 and the radius of the orifice is defined as a. [52, 54, 55]

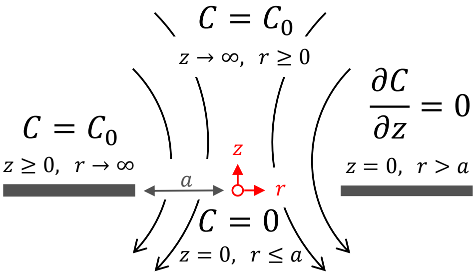

Figure 3.1.: Schematic illustration of the diffusion through an orifice in a cylindrical coordinate system (z, r) according to Cussler [55]. The local and bulk concentrations and the radius of the opening are represented by C, C_0, and a respectively.

$$\begin{aligned} C &= 0, & z &= 0, & r &\leq a \\ \partial C/\partial z &= 0, & z &= 0, & r &> a \\ C &= C_0, & z &= \infty, & r &\geq 0 \\ C &= C_0, & z &\geq 0, & r &= \infty \end{aligned} \tag{3.5}$$

$$C = C_0 - \frac{2C_0}{\pi} \arcsin\left(\frac{2a}{\sqrt{z^2 + (a+r)^2} + \sqrt{z^2 + (a-r)^2}}\right) \tag{3.6}$$

In the middle of the orifice the concentration is zero due to the first-listed boundary condition. This was initially done to keep the mathematical effort of finding a solution relatively low. However, considering the point symmetry with respect to the origin, the boundary condition is modified to $C = 0.5\,C_0$, $z = 0$, $r \leq a$. Consequently, the prefactor of the result in equation (3.6) is altered by a factor of two, because the corresponding gradient is half as large as before: $2C_0/\pi$ reduces to C_0/π without affecting the rest of the expression. Using the altered description for the location dependence of the concentration, the concentration gradient $\partial C/\partial z$ can be calculated. As an example, the solution for the gradient at the position $z = 0$ is shown in equation (3.7). [52, 54, 55]

$$\left.\frac{\partial C}{\partial z}\right|_{z=0} = \frac{C_0}{\pi}\frac{1}{\sqrt{a^2 - r^2}} \tag{3.7}$$

3.2. Permeance and other Characteristics

Several transport mechanisms rely diffusion. Nevertheless, some of them are classically not described by the aforementioned characteristic parameters. One of these special cases is the size-selective molecular sieving. A material with narrowly distributed pores only allows the passage of components exhibiting a smaller diameter than the size of the material's pores. Larger molecules are blocked and thus generating the sieving effect. [51, 56] In order to compare the performance of different membranes the following characteristics are widely used. The permeance P specifies the amount of substance permeating through the membrane per unit area, time and pressure. It is defined as the fraction of the molar flux F and the applied pressure difference Δp as shown in equation (3.8). The advantage of this definition is that the membrane's thickness does not need to be known. [57, 58]

$$P = \frac{F}{\Delta p} \tag{3.8}$$

The permeance of gas molecules is sometimes displayed as a function of the kinetic diameter. Following equation (3.9) it can be determined by employing the molecules' mean free path λ and the number density n. The mean free path indicates the averaged covered distance of a gas molecule until it will most likely collide with another one. The kinetic diameter d is the corresponding collision cross-section and can be interpreted as its apparent size. [56, 59–61]

$$d^2 = \frac{1}{\sqrt{2}\pi \, \lambda \, n} \tag{3.9}$$

The membrane's ability to separate two substances i and j from each other is described in terms of its selectivity α, which is simply the ratio of the respective permeances as shown in equation (3.10). [57, 58]

$$\alpha_{ij} = \frac{P_i}{P_j} \tag{3.10}$$

However, membrane processes also suffer from some weaknesses, which in general decrease their overall performance. For selective membranes a well-known issue is concentration polarization. Close to the interface of the membrane the concentration of the passing species is depleted on the feed side, where the substances to be separated were supplied, and increased on the permeate side, where the not retained species accumulate. Subsequently, this leads to a reduced transmembrane flux. One simple possibility to weaken this effect is to apply stirring in order to approach homogeneity. [56, 62, 63]

4. Instruments and Techniques

In this chapter the used instruments and the related techniques are briefly presented, following an alphabetic sequence. Its purpose is to show the fundamental principles, in order to gain a basic understanding for the method. Equations have been deliberately omitted and only inserted where they were needed to support the written explanations. Consequently, the methods are not described in full detail and it is referred to the quoted literature to acquire a deeper understanding.

4.1. Atomic Force Microscopy (AFM)

The atomic force microscope is an imaging technique allowing the analysis of surfaces on an atomic level. [64] A sharp tip mounted on a cantilever acts as the probe and scans the sample. The cantilever's deflection is monitored by a focused laser beam, which was aligned to it in advance. The deflection is caused by the displacement of the cantilever depending on the probe-sample interactions. [65, 66]

An AFM can be operated in a static or dynamic mode. The most famous example for a static mode is the contact mode in which the tip and the sample are in a repulsive contact with each other. Either the deflection (constant force) or the tip-sample distance (constant height) can be fixed. In order to achieve this, the respectively other parameter is permanently readjusted and recorded during the scanning process. Some dynamic modes are the non-contact mode and the intermittent contact (tapping) mode. In the former one the tip does not touch the specimen. Instead, the cantilever oscillates at its eigenfrequency close to the surface. The distance is readjusted to compensate the occurring frequency shifts due to attractive tip-sample interactions. In the intermittent contact (tapping) mode the cantilever is operated close to its resonance frequency and periodically touches the sample's surface with an interplay between attractive and repulsive forces. The amplitude of the oscillation is kept constant by adjusting the height. In all modes, it is possible to simultaneously read out additional acquisition channels to collect information, for instance, about the lateral force (contact mode) or the phase (dynamic modes). [67, 68]

By performing bulge tests on samples suspended over a hole the AFM can be used for the extraction of mechanical properties. From the observation of the cantilever's deflection h at known pressures $P(h)$ the Young's modulus E and the residual stress σ_0 can be calculated using the Beam's equation (4.1). The thickness t and the radius a of the material need to be known. The prefactors for spherical samples are defined as $c_1 = 4$, $c_2 = 8/3$ and the Poisson's ratio for amorphous polymers is estimated to be $\nu = 0.35$. [23, 25, 69, 70]

$$P(h) = c_1 \frac{\sigma_0 t}{a^2} h + c_2 \frac{Et}{a^4(1-\nu)} h^3 \tag{4.1}$$

The mechanical characterization was done by Florian Paneff using a NT-MDT NTEGRA PNL system with a self-build sample holder [23, 70]. The author measured specimens of free-standing alkanethiol films and mixed samples consisting of alkanethiol and oligophenylthiol SAMs on gold, employing the same system. Niklas Biere performed the imaging of the surface topology of pure alkanethiol samples on a gold surface with a RHK Technology UHV 7500 system equipped with a R9 controller and a liquid nitrogen flow cryostat. The data were processed with Gwyddion 2.55 [71].

4.2. Confocal Laser Scanning Microscopy (CLSM)

Fluorescence is one type of luminescence where the absorption of light excites the fluorophore into a higher electronic singlet state and causes the emission of radiation on a 10^{-8} s timescale. [72] Fluorescence images with a high spatial resolution can be obtained by using a confocal microscope in which a laser is routinely utilized as the source of radiation. [73] The specimen is virtually divided into several smaller areas which were illuminated and scanned in a certain sequence within different focus planes (optical sectioning). By using point illumination and a pinhole in front of the detector only information from an object within the respective focus plane will lead to a signal. The complete sample is reconstructed at the end of the measurement. [74]

An inverted CLSM, model LSM 780 with integrated FCS, from Zeiss operated by Anna Dreyer has been employed for the measurements.

4.3. Contact Angle Goniometry (CAG)

The observation of contact angles θ is a method to gain information about the wetting properties of a surface with respect to a certain liquid. If $\theta = 0$ ° the liquid spreads on the surface (“complete wetting”). The terms “wetting” and “non wetting” are used for contact angles $\theta < 90$ ° and $\theta > 90$ °, respectively. When using the sessile drop method, a droplet is placed on a surface and imaged by a camera from the side. The drop is illuminated by a light source, which is located behind it. Camera, drop and light source are in one line. Thus, the droplet appears dark and the shape can clearly be distinguished from which the contact angle can be derived. [75]

For the imaging process a self-build telescopic contact angle goniometer [76] was used. The taken images were processed with ImageJ 1.52a [77] using the contact angle plugin [78]. The shape of the drop was fitted with an ellipse best-fit and the contact angle was calculated.

4.4. Gas Permeation Measurements

The exploration of the substance-specific permeance through a material provides information about its applicability, for instance to separation processes [8], and can lead to a better understanding of the involved transport mechanisms [9, 42]. Experimental approaches for the determination of a species' permeance use a pumped vacuum chamber which is separated by the material of interest into a feed and permeate compartment. The feed side is filled with a certain amount of gas which will permeate through the specimen and be detected by a mass spectrometer. [79–81]

According to equation (4.2) [41] the permeance P of each gaseous species was calculated by dividing its flow rate Q through the free-standing sample area A and the applied feed pressure p_{feed}. A prerequisite for the validity of the equation is a well-evacuated permeate side.

$$P = \frac{Q}{A\, p_{\text{feed}}} \tag{4.2}$$

The gas permeation experiments were done by Daniil Naberezhnyi and Petr Dementyev using an improved design of the original self-built permeation system described by Yang *et al.* [8]. A detailed description of the experimental procedure and the upgraded system is given by Dementyev *et al.* [41]. Briefly, a HAL V RC PIC-RGA 1001 quadrupole mass spectrometer from Hiden Analytical was employed for the signal detection. The feed pressure was measured by a gas-independent Baraton$^{\text{TM}}$ capacitance manometer, model 626C52MCE9, from MKS Instruments Incorporation.

4.5. Gravimetric Analyses

Standard test methods, which allow good reproducibility and comparability of the results, have been developed to unify the approaches for the determination of material properties. [82] The permeance of substances through a material can be investigated by the mass loss experiment from ASTM International [83], which is briefly described in the following paragraph. [8, 40]

A container is filled with a defined amount of a liquid and the material to be tested is mounted on top of the container. The set-up is put into a controlled environment regarding the temperature and the partial pressure of the liquid. Due to a pressure difference between inside (high partial pressure) and outside the container (low partial pressure) the liquid permeates through the material. The record of the mass loss by a balance after certain time periods allows to quantify the permeance.

The permeance P can be calculated by using equation (4.3) [8], where Δm is the mass loss through the specimen's area A over a defined time period Δt. The molecular weight of the liquid is described by M. The pressure difference is represented by the term $p(T)^*_{liq}\,(1-\phi)$. At a constant temperature T the vapor pressure inside is the saturation vapor pressure $p(T)^*_{liq}$. Outside ϕ is the ratio of the liquid's partial to the saturation vapor pressure. In the case of water ϕ is equal to the relative humidity RH.

$$P = \frac{\Delta m}{M \cdot A \cdot \Delta t \cdot p(T)^*_{liq}\,(1-\phi)} \tag{4.3}$$

The basic container design from Yang *et al.* [8, 40] was modified to achieve a reusable set-up as shown in figure 4.1. The sample part can be detached from the container. This allows multiple measurements of one sample with different liquids and the possibility to check it for defects or contaminations by microscopic methods. Thus, the specimen's cleanliness and intactness are ensured. Copper or Teflon gaskets, which are comparable to a CF flange system, are used to seal the container. The technical drawings [84] were made by the mechanical workshop of Bielefeld University and detailed schemes are attached to appendix A. However, the experimental procedure by Yang *et al.* [8, 40] has been conserved.

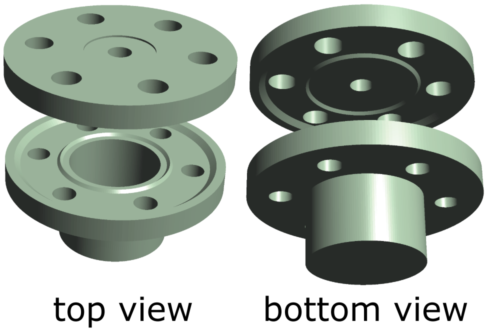

Figure 4.1.: Modified container design based on Yang *et al.* [8, 40] for performing mass loss experiments: The container can be reused due to the use of gaskets comparable to CF flange systems. Samples can be tested by several liquids and checked by microscopic methods. The technical drawings [84] were made by the mechanical workshop of Bielefeld University.

Each container was filled with 400 µl Millipore water (Super-Q$^{\mathrm{TM}}$ 4, Merck Millipore). The experiments were performed in a Shel Lab 1445-2 gastight oven from Sheldon Manufacturing Incorporated at a constant temperature of $T = (30 \pm 0.1)\,°\mathrm{C}$. Anhydrous lithium chloride (Fisher Scientific U.K. Limited, laboratory reagent grade) was used to guarantee a constant low relative humidity environment of RH = 15 % inside of the oven. The mass loss was oberserved by using a ME36S-OCE (Sartorius Aktiengesellschaft, sensitivity: 1 µg) microbalance. For the evaluation the molecular weight and the vapor pressure of water are defined to be $M = 18.015268\ \mathrm{g\,mol^{-1}}$ [85] and $p\,(30\,°\mathrm{C})^{*}_{H_2O} = 42.4$ mbar [86].

4.6. Helium Ion Microscopy (HIM)

The helium ion microscope uses the noble gas helium as an imaging gas. The ion beam is produced by a gas field ionization source (GFIS). The collimated helium ion beam scans over the sample, which leads to the generation of secondary electrons (SE). These are detected and their counts are used for generating an image. If backscattered helium ions are observed, different elements and thus materials can be identified. [87] Insulating samples can be imaged by the alternating scanning with the ion and an electron beam, which compensates the positive charge of the scanned area. [88] The HIM can also be operated in the transmission mode. In this mode either the transmitted helium ions are directly detected [89] or the transmitted beam hits a metal surface and generates SE, which are then collected [90]. The helium ion beam can be focused to a minimum size of 0.25 nm [91]. More detailed information on helium ion microscopy are given, for instance, by Hlawacek and Gölzhäuser [92].

An Orion Plus helium ion microscope from Zeiss was used and the measurements were performed by Daniel Emmrich and Michael Westphal.

4.7. Isothermal Titration Calorimetry (ITC)

A chemical reaction can either be exothermic or endothermic, which means that heat is released or uptaken. These small energetic changes can be detected by the isothermal titration calorimetry. A stirred reference (e.g. buffer solution) and sample cell (e.g. buffer solution plus first reactant) are inside an evacuated container surrounded by an adiabatic shielding and kept at the same constant temperature. Subsequent injections of the second reactant (titrant) will cause a change in the power needed for each heater to keep the two cells at the same temperature. Exothermic reactions decrease the needed power, whereas endothermic lead to an increase. [93, 94]

The ITC measurements were done by Anna Dreyer using a MicroCal VP-ITC system equipped with a MicroCal ThermoVac from Malvern Instruments GmbH.

4.8. Liquid Scintillation Counting

Radioactive decay provides ionizing radiation, which can be absorbed by a fluorophore. The subsequent emission of photons due to the excitation is called scintillation. [95] A photomultiplier tube converts the emitted photons into an electrical output signal. Tritium or hydrogen-3 (^{3}H), carbon-14 (^{14}C) and phosphorous-32 (^{32}P) are low energy beta emitters. If these are used as tracer species, the scintillation counting must take place in the liquid phase due to the limited penetration power of the radiation to ensure spatial proximity between the radioactive material and the fluorophore. [96]

Anna Dreyer handled the radioisotopes from Hartmann Analytic GmbH and acquired the time-dependent tracer counts by utilizing a 1900 CA Tri-Carb liquid scintillation (Packard Instrument Company Incorporated) with the LSC universal scintillation cocktail Rotiszint® eco plus from Carl Roth GmbH & Co. KG.

4.9. Nuclear Magnetic Resonance Spectroscopy (NMR)

An atom has a certain nuclear spin, which causes the splitting of its energy states into distinguishable levels when an external magnet field is applied. [97] Transitions between the energy levels are induced by using radio waves with the right frequency. [98] The so-called Larmor frequency depends on the nucleus, the applied external magnetic field, the chemical environment, and spin-spin-couplings. The energy absorption is detected and generates a characteristic NMR signal. The evaluation of those resonance signals allows to resolve the chemical structure of the sample. [99] Thus, nuclear magnetic resonance spectroscopy is powerful and crucial technique in chemistry. [98]

The NMR experiments were performed at the Max Planck Institute for Polymer Research in Mainz on behalf of Nicole Wutke.

4.10. Optical Microscopy

In an optical microscope the concept of geometrical optics is used to gain an enlarged view of the specimen. [100] In the present thesis, the specimens were measured in reflection. Operating in the bright field mode, the reflection of light by the sample causes the contrast. When using the dark field illumination, only light which is diffracted by the specimen can be seen and thus providing the information. [100, 101] The interference of two beams polarized perpendicular to each other is employed for the Nomarski interference contrast where in principle the comparison of the two displaced images leads to the generation of the final image. The right alignment of the used analyzer facilitates colored images by the extinction of certain wavelengths. The technique is also known as differential interference contrast (DIC). [100–102]

An Olympus BX51 system equipped with the components BX51TRF, TH4-200, U-DICR, U-AN360-3, U-25LBD, U-PO3, U-TV1X-2, C5060-ADU, and with an Olympus C-5060 camera has been used to obtain the images via the software Olympus DP-Soft 5.0.

4.11. Reflection-Absorption Infrared Spectroscopy (RAIRS)

The absorption of infrared radiation by the specimen is the fundamental process of this spectroscopy method. This occurs when the frequencies of the structural-dependent vibration of the sample and the infrared radiation oscillate in resonance. However, a vibration can only be seen if a change in the dipole moment occurs. [103, 104]

In RAIRS a metallic surface, which reflects the absorbed infrared irradiation, is used, leading to an increased amplitude at high incidence angles, but suffering from a lack of detection of vibrations which dipole moments are not perpendicular to the surface. [105] There is a small amount of sample material when an adsorbed monolayer on a metal surface is examined. To detect the slight change in the infrared radiation, a sensitive detector like a mercury cadmium telluride detector (MCT) is necessary, where electrons are excited from the valence into the conduction band due to the photoelectric effect and thus providing an electrical output signal. [105, 106] Fourier transformation (FT) can be used to record the full range of the infrared absorption in a short time or to gain a better signal-to-noise ratio (multiplex advantage) compared to a dispersive spectrometer. [107] For instance: inside a Michelson interferometer the optical path difference of the broad-band infrared radiation is altered by splitting the light into two beams. One is heading towards an immovable mirror and the other one towards a non-stationary mirror. Interference between the two rays occurs when they recombine. In the space domain, the resulting interferogram shows the signal intensity as a function of the optical path difference (distance). By applying a FT, the interferogram is converted into the wavenumber domain generating the complete spectrum with the signal intensity as a function of the frequency. [107, 108] A photoelastic modulator (PEM) [109] splits the linear polarized radiation into two linear polarized waves and introduces a time-dependent phase shift, which allows the distinction of the specimen's vibrations from the surroundings. [110] When using those components the full name of the technique expands to Fourier transform polarization-modulated reflection-absorption infrared spectroscopy (FT-PM-RAIRS). The working principle is briefly described in the subsequent paragraph.

A FT-PM-RAIRS works like the following: Leaving the interferometer, the infrared radiation is first linearly polarized. Afterwards the PEM modulates the phase shift of the radiation between $\Delta\lambda = \pm\lambda/2$. At certain times this leads to purely parallel (p-polarized) or perpendicular polarized (s-polarized) waves with respect to the plane of incidence. A lock-in amplifier couples the detector with the PEM, resulting in a signal detection only when pure p- or s-polarized radiation occurs. The polarized light is reflected twice: at the surroundings-adsorbate and at the adsorbate-metal interface (figure 4.2). The purely s-polarized light will be canceled in the vicinity of the metal surface due to a phase shift of 180° and thus only provides information about the surroundings. The p-polarized light on the other hand carries information from the adsorbate and the surroundings. By subtracting the data of the p-polarized and the s-polarized light, the pure information from the adsorbate are accessible, which means that the reference and the sample spectrum are taken simultaneously from the same area. [109–113]

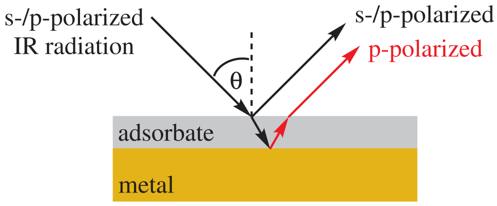

Figure 4.2.: RAIRS reflection processes: Alternating s- and p-polarized IR radiation is reflected at the surroundings-adsorbate and at the adsorbate-metal interface. Only the p-polarized light provides information from the surroundings and the adsorbate, whereas the s-polarized radiation exclusively carries the information from the surroundings. Modified according to Greenler [111].

A FT-PM-RAIRS system composed of a Vertex70 and a PMA50 module from Bruker equipped with a Rocksolid$^{\mathrm{TM}}$ interferometer and a MCT detector (limit of sensitivity 700 cm^{-1}), a DSP lock-in amplifier (model SR830, Stanford Research Systems, SRS), and a PEM-90$^{\mathrm{TM}}$ photoelastic modulator from Hinds Instruments has been used. Processing was done with the optics user software OPUS 5.5 [114]. The peak assignment based on the references [103, 115–119].

4.12. Scanning Electron Microscopy (SEM)

Electrons are utilized in a scanning electron microscope as the information carrier. A focused electron beam (primary electrons, PE) scans over the sample, which leads to the emission of secondary electrons (SE). These are detected and used for the the generation of an image. Insulating samples can hardly be imaged because of charging effects. For instance, an induced negative charge cannot be compensated. [120]

A Helios Nanolab 600 scanning electron microscope (Field Electron and Ion Company, FEI) was employed by Björn Büker.

4.13. Transmission Electron Microscopy (TEM)

The transmission electron microscope utilizes electrons for the generation of an image. An electron beam is focused on a thin sample (typically 5-500 nm when using 100 keV electrons) and the transmitted electrons are detected. The contrast is generated by the interaction of the electrons with the specimen. [121] Therefore it can become quite challenging to image inhomogeneous samples with a thickness of around one nanometer.

A JEM-2200 FS transmission electron microscope from Japan Electron Optics Laboratory (Jeol) was operated by Inga Ennen. The image processing in terms of contrast enhancement and resolution optimization was done by the subsequent use of DigitalMicrograph® 3.X [122] and GIMP 2.10.14 [123]. The pores were highlighted and evaluated with Gwyddion 2.55 [71]. The determination of the effective sample area was done by using ImageJ 1.52a [77].

4.14. Ultraviolet-Visible Spectroscopy (UV-Vis)

According to some definitions, the wavelength of ultraviolet-visible light ranges from 200 nm to 800 nm. The absorption of radiation in this spectral range causes electronic transitions in the specimen. Valence electrons get excited and change from a bonding into an antibonding molecular orbital (e.g. $\pi \longrightarrow \pi^*$). In a dual beam UV-Vis spectrophotometer the light is split into two individual beams. One beam passes through the reference and the other through the sample cell. Due to the different absorption of the radiation, the concentration of the analyt can be calculated by using the Beer-Lambert law. [124, 125]

Anna Dreyer performed the UV-Vis measurements with an UV-2401 PC spectrophotometer from the Shimadzu Corporation.

4.15. X-Ray Photoelectron Spectroscopy (XPS)

X-ray photoelectron spectroscopy is a powerful tool for identifying the chemical composition and the thickness of a thin film material on a surface. It provides information about the binding energy and the chemical environment of the involved atoms. This is why the technique has been also called electron spectroscopy for chemical analysis (ESCA). [126–129]

The basic working principle of a X-ray photoelectron spectrometer is the photoelectric effect [130, 131]. X-ray photons excite core electrons of an atom, which are subsequently ejected if the transferred energy is high enough to overcome its binding energy and the work function of the spectrometer. When the resulting hole is filled by an energetically higher electron, the excess energy can be emitted as a X-ray photon or transferred to a third electron (Auger electron), which will be extruded (figure 4.3). [126, 132]

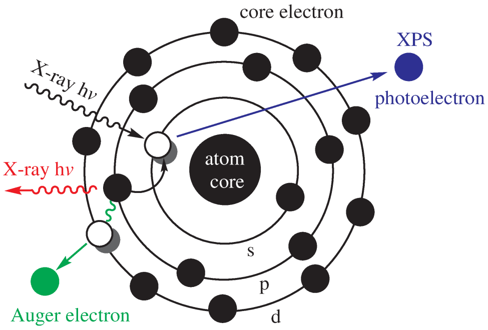

Figure 4.3.: Interaction of a X-ray photon with matter: A core electron is ejected (blue, XPS) after the absorption process and the resulting electron hole is filled by an energetically higher one. The excess energy can either be emitted (red) or radiation-free transmitted to a third electron, which leaves the system (green, Auger electron).

The kinetic energy of the released electron is measured and the counted electrons are displayed as a function of their corresponding binding energy. For a conductive sample, which is in electrical contact with the spectrometer, equation (4.4) [127] can be applied.

$$E_K = h\nu - E_B^F - \phi_{sp} \tag{4.4}$$

The kinetic energy of the electron is represented by E_K. The energy of the X-ray photon is $h\nu$. The electron's binding energy related to the Fermi level and the work function of the spectrometer are E_B^F and ϕ_{sp}, respectively. The latter parameter is device-dependent and needs to be determined for each spectrometer individually.

Due to spin-orbit (j-j) coupling core electrons with an orbital angular momentum quantum number greater than zero ($l > 0$) show doublets in the XP spectrum. According to $j = |l \pm s|$, the spin angular momentum with its corresponding quantum number s combines with l to the total angular momentum quantum number j. With known j the intensity ratios between the two doublet peaks can be calculated as $(2j + 1)$. The notation of the core level signals follows the general nomenclature nl_j with n representing the principle quantum number. [127]

From the characteristic binding energy of the detected electron the element as well as it's chemical state can be concluded. Different oxidation states are distinguishable and chemically non-equivalent positions of the same element in one molecule can lead to multiple peaks in the XP spectra. Consequently, an identification of functional groups is possible. [129, 133] Lindgren [134] historically reviews the chemical shifts in X-ray and photo-electron spectroscopy. Taucher *et al.* [135] point out that also electrostatic effects shift the core-level binding energy and must therefore be taken into account when interpreting those displacements.

The surface sensitivity of this method is based on the inelastic mean free path (IMFP, λ_{IMFP}) of the ejected core electrons. The IMFP describes the average distance between inelastic scattering events of an electron with a given kinetic energy inside a specific material. After a distance equal to the IMFP, the remaining number of non-scattered electrons is $1/e$ of the initial number of the ejected core electrons, which means that the longer the distance to the material-vacuum interface, the less is their probability to escape into the vacuum and to contribute to the detected signal. [128] The IMFP's electron energy dependence follows an universal curve and has values of $\lambda_{\mathrm{IMFP}} < 5$ nm in the typically used energy range for X-ray photoelectron spectroscopy. [136–140]

To determine the thickness d of a thin film material the attenuation of a reference signal can be used and compared to the corresponding signal of a known reference sample. Following equation (4.5) [43, 128] the intensities of the reference signal of the thin film sample, I_{film}, and the reference, I_0, the inelastic mean free path of the electrons through the thin film material and the tilt angle θ need to be known.

$$I_{\mathrm{film}} = I_0 \exp[-d/(\lambda_{\mathrm{IMFP}} \cos\theta)] \tag{4.5}$$

A multiprobe X-ray photoelectron spectrometer system from Omicron Nanotechnology equipped with a monochromatic aluminum K_α X-ray source (XM 100 MkII, 1486.7 eV, max. 255 W), a hemispherical electron analyzer (EAC 2000 Sphera) and an electron gun (SL 1000) has been used. The tilt angle of the analyzer was $\theta = 13°$. The $\mathrm{Au}4f_{7/2}$ peak at a binding energy of $E_B^F = 84$ eV was employed as a reference signal for the thickness determination. For oligophenylthiols the inelastic mean free path was estimated to be $\lambda_{\mathrm{IMFP}} = 32$ Å [43] and for alkanethiols to be $\lambda_{\mathrm{IMFP}} = 42$ Å [141]. The XP spectra were processed with the software CasaXPS 2.3.22PR1.0 [142]. The peak assignment based on the references [7, 34, 36, 48, 119, 143–153]

5. Functionalization of Carbon Nanomembranes

This tripartite chapter focuses on the functionalization of carbon nanomembranes with a special emphasis on protein immobilization and explores the applicability of the presented approaches. First, an introduction to the current state of the research and the motivation of the investigations performed in the present thesis are given. Subsequently, the achieved results are presented and discussed in the context of the preliminary works and the stated objectives. A summary with prospects for further work is given at the end of the chapter.

5.1. Current State of Research

Carbon nanomembranes serve as a template for further chemical reactions due to their available functional groups. Typically amino (-NH_2) or thiol groups (-SH) can be employed for the further processing. Amin *et al.* [154] produced patterned CNMs with two different precursor molecules among which only one exhibits an active amino group (cABT). The other molecule (cBT) only consists of carbon at the surface, which is not favored during the functionalization step. Vinyl monomers grow to polymer carpets on the complete nanomembrane by self-initiated surface photopolymerization and photografting (SIPGP) with a strong preference for the cABT areas. In figure 5.1a the fabrication and the 3D representations of the resulting polymer carpets are shown. The corresponding AFM scans and height profiles are displayed in figure 5.1b. The line profiles nicely reveal the altering sequence of the cBT and cABT areas indicating that the height of the polymer carpet is about 11 nm.

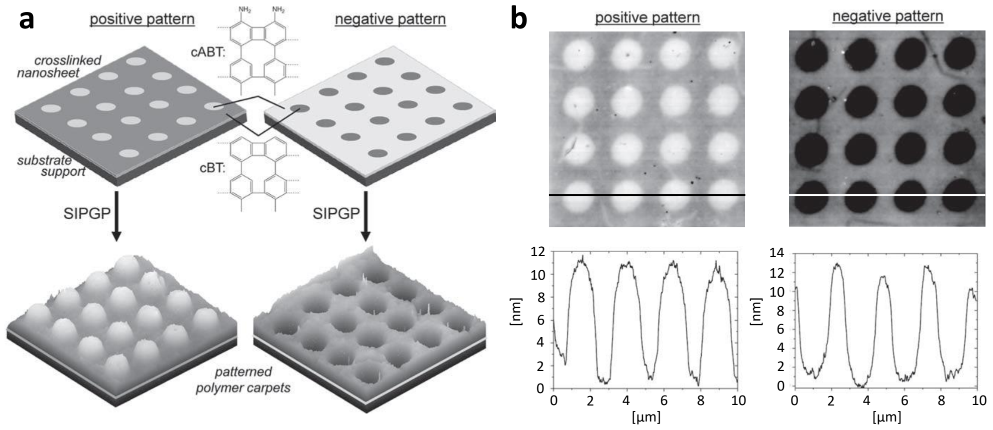

Figure 5.1.: (a) Polymer carpet fabrication on patterned CNMs by self-initiated surface photopolymerization and photografting (SIPGP). (b) Corresponding AFM scans and height profiles of the resulting polymer carpets. The strong preference for the reaction at the amino-terminated areas (cABT) is obvious. Reprinted and adapted with permission from Amin *et al.* [154]. Copyright 2011 Wiley-VCH Verlag GmbH & Co. KGaA, Weinheim.

The former example used a radical-driven process for the functionalization, which generally demonstrated the possibility for further selective chemical reactions. Depending on the application, the immobilization of proteins requires a certain functionalization strategy of the carbon nanomembrane. In a first attempt Rhinow *et al.* [22] immersed a CNM made of cBT into a buffer solution of purple membrane (PM) extracted from *Halobacterium salinarum*. PM contains the protein bacteriorhodopsin (bR), which acts as a proton pump. It was shown that the carbon nanomembrane could immobilize patches of PM through unspecific interactions. Structural analyses by cryo-TEM and AFM were successfully performed, demonstrating that CNMs preserve the structural integrity of the specimen. Thus, when using the aforementioned techniques, carbon nanomembranes are promising supports for comparing different biological samples without altering their respective appearance.

Biebricher *et al.* [155] explored the possibility of specific irreversible protein binding strategies and investigated the issue of quenching due to the metallic surface when doing fluorescence measurements. In this study 4'-nitro-1,1'-biphenyl-4-thiol (NBPT) was used for the SAM preparation. The exposed regions of a partially shielded SAM result after cross-linking in an amino-terminated CNM, which was used as a starting point for further functionalization. Unirradiated areas were exchanged by poly (ethylene glycol) to suppress unspecific protein attachment. Two different main approaches were tested. First, streptavidin was bonded to the -NH_2 moiety of the carbon nanomembrane by using glutaraldehyde. The examination of the fluorescent signal employing a fluorescently-labeled counterpart revealed that quenching from the metallic gold surface still occurred. The subsequent addition of more layers to the previous one by employing glutaraldehyde-mediated cross-linking of the lysine residues of streptavidin or antibody layers could only enhance the signal-to-background (S/B) ratio to ~ 4. This method was not satisfying due to the utilization of a large amount of proteins. The second strategy used tetraethylenepentamine (TEPA) as a molecular spacer unit after the activation of the amino groups through *p*-nitrophenylchloroformiate (NPCF). Because TEPA also exhibits a terminal amino group the increase of the distance to the metallic surface could be done by the same building block. In a final step the desired protein could be attached by the usage of glutaraldehyde. With this S/B-ratios of >20 could be achieved while simultaneously a comparable low amount of protein is needed.

An effective and reversible immobilization method for proteins was presented by Turchanin *et al.* [36]. Again, a partially shielded NBPT SAM was employed. The surface-active amino groups undergo a condensation reaction with *tert*-butyl protected tris-*N*-nitrilotriaceticacid (NTA). The deprotection of its acid moieties and the subsitution of unirradiated areas by (triethylene glycol) (EG_3) units were conducted. In figure 5.2a the spectroscopic evidence for the different molecules are provided. Particular scans of the sulfur, carbon, nitrogen and oxygen regions were performed. However, the XP spectra will not be discussed in detail at this point, although the significant carbon and nitrogen signals are briefly described. The C1s signals of the SAM and CNM stage do not significantly differ from each other with the exception of the broadening due to the irradiation. The signals of EG_3 and tris-NTA-EG_3 are dominated by the ones of alkyl groups, especially proving the presence of carboxyl groups at ~ 289.2 eV.

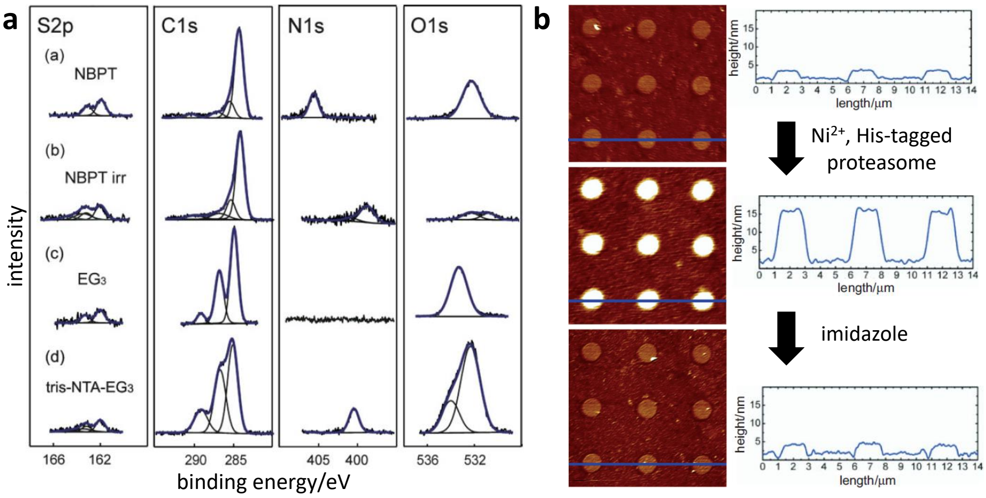

Figure 5.2.: (a) XP spectra of the different molecular structures involved in the functionalization procedure identifying their characteristic signals. (b) AFM scans and height profiles of a patterned NBPT CNM treated with EG_3 and functionalized with tris-NTA. The reversibility of the proteasome's binding can be clearly seen. Reprinted and adapted with permission from Turchanin *et al.* [36]. Copyright 2008 Wiley-VCH Verlag GmbH & Co. KGaA, Weinheim.

The N1s signal for the SAM is located at ~ 405 eV, indicating the nitro group. After irradiation the signal shifts to ~ 399 eV, which is characteristic for amino groups. The signal of tris-NTA-EG_3 exhibits a comparable higher intensity and has a binding energy of ~ 400.5 eV, showing the presence of nitrogen atoms in a different chemical environment, which is in agreement to its chemical structure. Additionally the deprotection of the NTA units was checked by the addition of nickel(II) ions. The reported XP spectra confirmed chelated nickel inside of the NTA moieties. In figure 5.2b AFM scans and the corresponding height profiles of a functionalized CNM are displayed. It can be clearly seen that the patterned areas are higher due to the surface functionalization. The addition of nickel(II) ions and the his-tagged proteasome leads to a sharp increase only where the chelating NTA groups are located. Thus, the octahedral complex between the NTA units and the protein's his-tag was formed. The reversibility was proven by the subsequent washing with imidazole, which competes with the his-tag of the proteasome for the binding site and replaces it with time. The line scans indicate that the height returned to a comparable level as before the protein binding.

Turchanin *et al.* [36] proved that the tris-NTA groups are an effective way to immobilize proteins reversibly on a carbon nanomembrane. Kankate *et al.* [38] adapted the general idea and developed a slightly different functionalization strategy. The utilized molecular structure is given in figure 5.3b. In this approach the tris-NTA molecule has a longer alkyl spacer ending in a terminal -SH group. This was probably done to increase the distance to the metallic support and thus to avoid quenching during fluorescence measurements according to the results of Biebricher *et al.* [155]. Employing 3-(maleimido)propionic acid *N*-hydroxysuccinimide ester as a mediator, the CNM firstly conducts an ammonolysis, whereas later a stable thioether bond between the NTA's thiol group and the mediator is formed. The specimen was loaded with $NiSO_4$ and subsequently exposed to a fluorescently-labeled and his-tagged protein. In this study a maltose binding protein with a decahistidine tag and Oregon Green 488 as a fluorescence marker (MBPH10-OG488) was utilized. The result of the conducted fluorescence analysis is shown in figure 5.3a. The patterned signal originates on a large scale only from the areas which were treated with the described procedure.

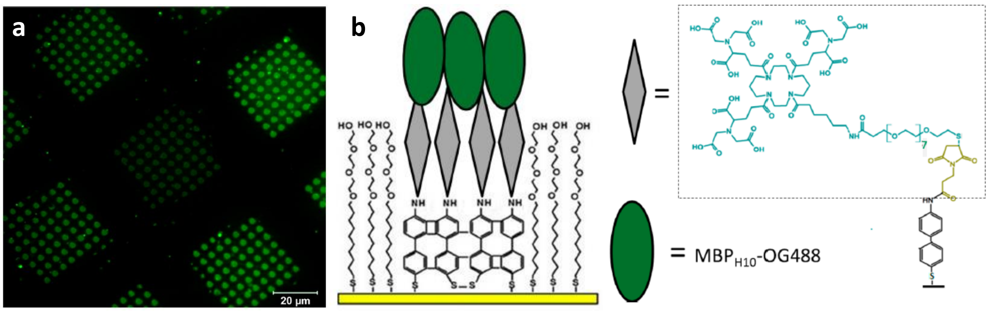

Figure 5.3.: (a) Large scale fluorescent image of a patterned and functionalized carbon nanomembrane showing the possibility to bind proteins specifically to the CNM. The schematic structure is given in (b). (b) Detailed scheme of the resulting molecular structure after the functionalization process. The maltose binding protein with a decahistidine tag and Oregon Green 488 as a fluorescence marker is labeled as MBPH10-OG488. Reprinted and adapted with permission from Kankate *et al.* [38]. Copyright 2017 American Chemical Society.

Recently a patent [119] which deals with the functionalization of surfaces and employs among other things the usage of the selective and fast copper-free click chemistry was registered by CNM Technologies GmbH and Aptarion Biotech.

The previous examples showed that in principle the functionalization of a supported carbon nanomembrane is possible. The immobilization of proteins can be done with irreversible or reversible methods and the variation of the distance to the support plays an important role when dealing with fluorescent agents. Zheng *et al.* [34] moved on to free-standing CNMs and demonstrated that the two sides of a NBPT carbon nanomembrane can be functionalized differently. After cross-linking, the transferred CNM exhibits on the upper side amino and on the lower side thiol groups. The amino groups were treated with tetramethylrhodamine (TMR) isothiocyanate, leading to a thiourea moiety. The thiol groups reacted with ATTO647N maleimide, resulting in a stable thioether bond of the ATTO unit. Both TMR and ATTO647N are commonly used fluorescent dyes and were utilized as a control agent. In figure 5.4a/b the respective fluorescence micrographs of the free-standing carbon nanomembrane are shown, proving the successful side-dependent funtionalization. Consequently, the subsequent treatment of both sides results in a free-standing Janus membrane, which was verified by Förster resonance energy transfer (FRET) displayed in figure 5.4c.

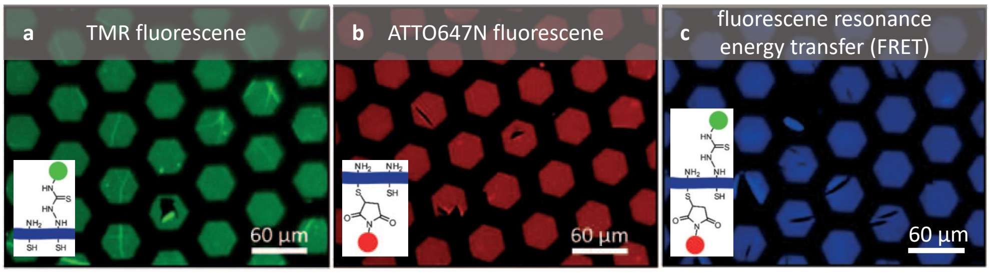

Figure 5.4.: (a)/(b) Fluorescence micrographs of free-standing, one-sidedly functionalized CNMs suspended over TEM grids. As dyes tetramethylrhodamine (TMR, green) isothiocyanate and ATTO647N (red) maleimide were used. (c) Förster resonance energy transfer (FRET) micrograph of the Janus system. Reprinted and adapted with permission from Zheng *et al.* [34]. Copyright 2010 Wiley-VCH Verlag GmbH & Co. KGaA, Weinheim.

The aim of the investigations presented in this chapter is to immobilize proteins on both sides of the free-standing carbon nanomembrane based on its Janus behavior. The type of immobilization can either be irreversible or reversible, whereas the latter one is more favorable. As a proof-of-concept transmembrane FRET measurements between the proteins should verify the successful coupling. Single-sided functionalization can be tested using fluorescent microscopy. For FRET measurements the distance should be as short as possible, whereas for the single-sided measurements a certain distance is needed due to quenching effects. Considering both the objectives and the previously mentioned investigations, a functionalization strategy which balances on the one hand the distance between the dye and the metallic support and on the other hand between the spatially divided fluorophores needs to be developed. The successful realization would make carbon nanomembranes an attractive model system for the investigation of biological membrane processes.

5.2. Protein Coupling to Carbon Nanomembranes

The following results were obtained in cooperation with Anna Dreyer from Plant Biochemistry and Physiology of the Faculty of Biology of Bielefeld University. The cloning, the heterologous expression and the application of the proteins were done by her.

5.2.1. Complex Formation with L-Lysine-NTA

In the course of obtaining a bilaterally functionalized carbon nanomembrane, the first step is the successful binding of a protein to one side. The strategy presented by Kankate *et al.* [38] was chosen for this purpose. Unfortunately, the tridentate tris-N-nitrilotriaceticacid ligand had to be replaced by N-[N_α,N_α-Bis(carboxymethyl)-L-lysine]-12-mercaptododecanamide (L-lysine-NTA) as the former one was not available anymore. The difference between these two molecules is simply the number of chelating agents, which is reduced to one instead of three. However, the linking to the CNM through 3-(maleimido)propionic acid N-hydroxysuccinimide ester (MI) and the ability to form a complex with his-tagged proteins remain unaffected.

A detailed description of the sample preparation is given in appendix B. The different steps are visualized in figure 5.5a. NBPT was used as a precursor molecule for the self-assembly process on a gold substrate. The resulting SAM exhibited a terminal nitro group (a). The SAM was converted into a carbon nanomembrane with amino groups located at the surface (b) through the irradiation with low-energy electrons. During the first functionalization step with MI the ester has been cleaved and a peptide bond between the CNM and MI was formed (c). The resulting maleimide moiety specifically reacted with the thiol group of the NTA molecule, leading to the final molecular structure (d).

RAIRS and XPS measurements have been conducted to verify each step of the functionalization. Taking a look at the infrared spectrum of the SAM (a) in figure 5.5b both stretching vibrations of the nitro group - the symmetric ($\tilde{\nu} \sim 1348\ \text{cm}^{-1}$) and asymmetric ($\tilde{\nu} \sim 1528\ \text{cm}^{-1}$) - can be cleary seen proving the presence of the self-assembled monolayer. After the irradiation these bands vanish, indicating the transformation of the groups into amino moieties.

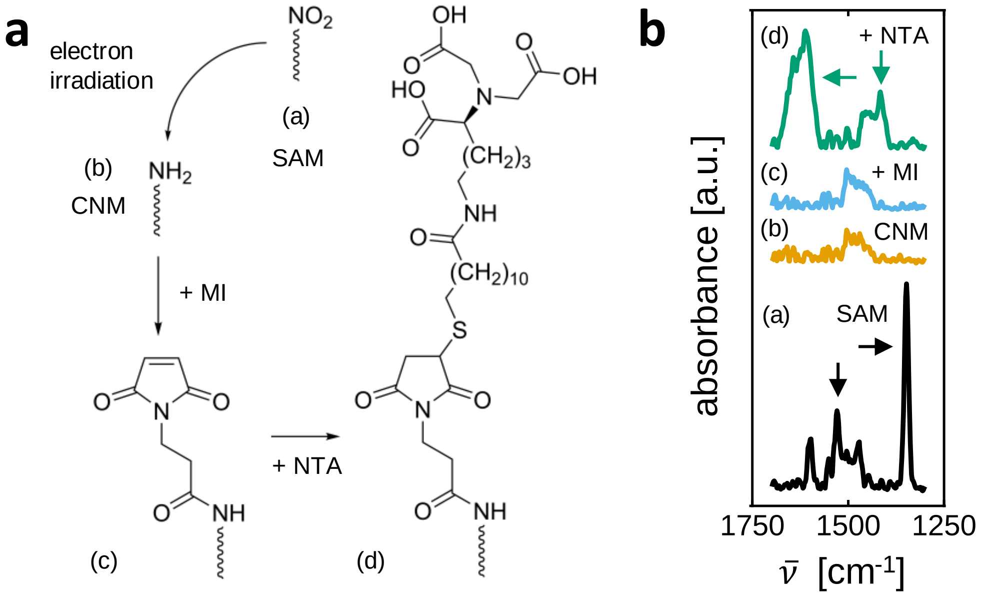

Figure 5.5.: (a) Schematic illustration of the functionalization route starting from an aromatic, nitro-terminated SAM and employing MI as well as L-lysine-NTA. (b) Corresponding RAIRS spectra of the different stages as shown in the reaction scheme. The arrows mark the positions of the characteristic vibrations, which are explained in the text.

The spectra of (b) and (c) exhibit no bands which are characteristic for the -NH_2, the peptide bond or the maleimide group. Nevertheless, their existence cannot be excluded because their dipole moment needs to be aligned with the electric field vector of the incoming polarized light to be detected by the RAIRS measurement. After the reaction step with NTA, the symmetric stretching vibration of the deprotonated carboxylic groups ($\tilde{\nu} \sim 1416$ cm^{-1}) is observed. A broad signal in the range of $\tilde{\nu} \sim 1580$ cm^{-1} to 1680 cm^{-1} is detected, which probably originates from an accumulation of the asymmetric stretching vibration of the carboxylates and the signals of the amide moieties. These vibrations indicate the successful functionalization and allow the conclusion to be drawn that the previous steps (b) and (c) have been present.

In figure 5.6 the XP spectra for the different stages of the functionalization are shown. Starting with the nitro-terminated SAM in (a), peaks for the -NO$_2$ functional group can be seen in the N1s and O1s spectra at binding energies of $\sim$ 406 eV and $\sim$ 532.5 eV respectively. The C1s signal is a superposition of two peaks, namely the one for the aromatic backbone at $\sim$ 284.4 eV and second one representing the -C-S and -C-N bonds at $\sim$ 285.7 eV. The latter one causes the signal to be slightly asymmetric towards higher binding energies. In the S2p scan the first peak of a doublet with an energy separation of $\Delta E = 1.2$ eV is located at $\sim$ 162.2 eV, indicating the presence of sulfur gold bonds. After the irradiation changes in the XP spectra can be seen. The resulting carbon nanomembrane (b) exhibits in the N1s scan a peak at $\sim$ 399.5 eV, which is characteristic for -NH$_2$ groups. The former signal for the nitro moieties is absent, proving the complete conversion of the functional groups. The sulfur peak broadens to higher binding energies due to the presence of a second doublet representing new sulfur species. As known from the literature, the species can either be unbonded thiols, sulfides or disulfides. The intensity of the oxygen signal decreases but does not disappear completely. In combination with the increase in intensity of the C1s peak it leads to the hypothesis that material was deposited onto the CNM during the irradiation process. The XP spectra after the functionalization step with MI are displayed in (c). The carbon and oxygen signal gain intensity, whereas the scans of N1s and S2p show no significant change to the prior step. Due to the structure of the maleimide group a second signal for the -C=O groups at higher binding energies in the C1s spectrum was expected.

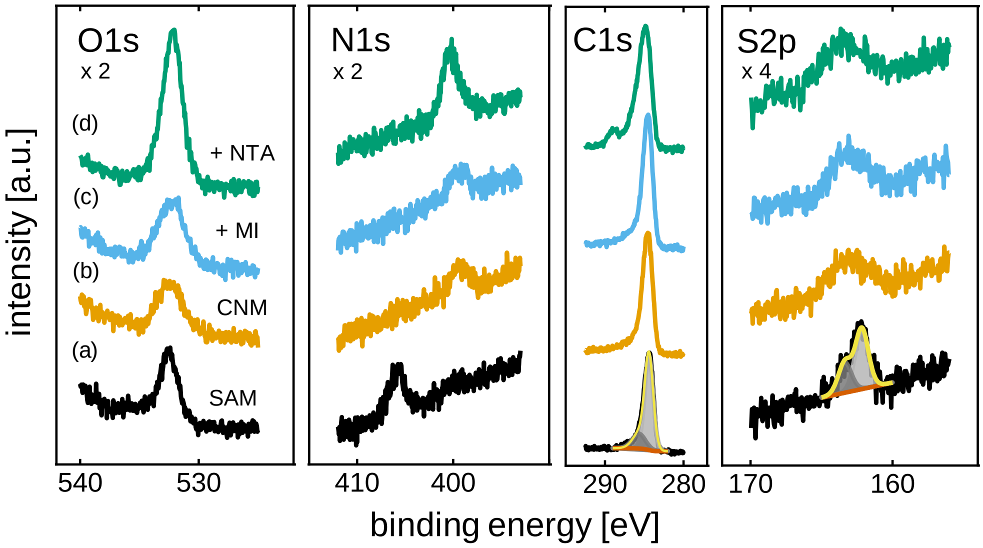

Figure 5.6.: XP spectra in the regions of oxygen, nitrogen, carbon and sulfur of each functionalization step starting from a NBPT SAM (a). After the exposure to electrons the resulting CNM (b) was further treated with MI (c) and NTA (d). Selected fits are shown for the SAM.

Nevertheless, the increase of intensity is at least a hint for the coupling of the MI to the carbon nanomembrane. The scans of the specimen after the second functionalization step with NTA are shown in (d). The C1s peak is shifted to higher binding energies and a second peak at ∼ 288.8 eV can be detected. The shift can be explained by the existence of aliphatic carbon and the second peak is characteristic for oxidized carbon in the chemical state -O-C=O. Both observations are in accordance with the chemical structure of the NTA moiety. Further evidence is given by the rise in the intensity of the O1s peak, which can be attributed to the incorporation of seven oxygen atoms per bonded NTA unit. The intensified nitrogen peak was shifted to a binding energy of ∼ 400.3 eV. This originates from the added nitrogen atoms in the different chemical environment of the NTA group. As expected, the S2p spectrum does not differ from the previous stage. Consequently, the realization of the different stages of the functionalization appears to be plausible. In combination with the conducted RAIRS measurements the successful bonding of the NTA moiety to the CNM according to figure 5.5a can be assumed.

To test the functionalization of the carbon nanomembrane, fluorescence measurements were performed. For this purpose the his-tagged cyan fluorescent protein mTurquoise2 was used. The incubation of the protein was done after loading the CNM with nickel(II) ions. The specimen was washed with buffer solution and subsequently imaged in the CLSM. To release the mTurquoise2 again from the octahedral complex, elution of the sample with imidazole was done. Rebinding of the protein following the same procedure should verify the reversibility of the coupling. In figure 5.7 the series of fluorescent images are displayed.

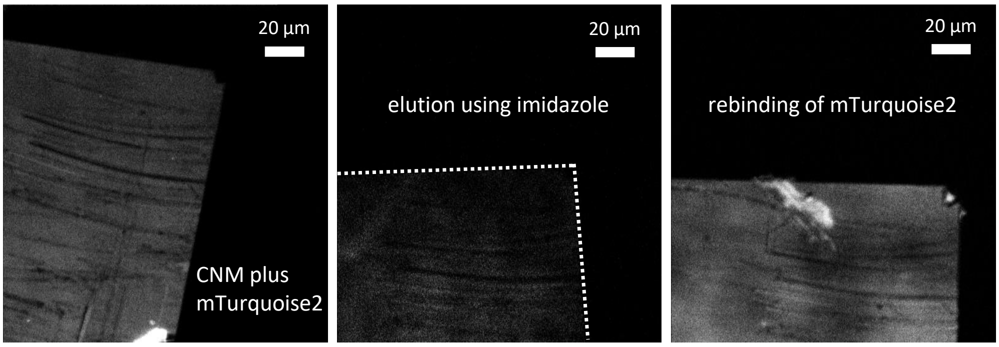

Figure 5.7.: Fluorescence images of a NTA-functionalized CNM. From left to right: Carbon nanomembrane loaded with mTurquoise2, the same sample after the elution of the protein trough imidazole and rebinding of the mTurquoise2.

It can be clearly seen that the binding of the protein was successful. In contrast to the black background the complete sample exhibits a fluorescent signal. It was expected that after the treatment with imidazole, which competes with the his-tagged protein for the binding site, no signal should be detectable anymore. The corresponding image reveals nevertheless some bright areas.

Consequently, the his-tagged mTurquoise2 was not removed completely, which could be improved by more extensive washing. The successful reattachment of the protein was demonstrated in the right panel of figure 5.7.

In principle the coupling of his-tagged proteins using the presented method could be achieved. Several attempts were made to reproduce these results or even to obtain comparable measurements. However, none of them succeeded and the reasons for this are still unknown. Under the aspect of developing a reliable functionalization strategy, experiments utilizing this approach were ceased and different ways were explored.

5.2.2. Reversible Protein Immobilization

To enable a faster screening for an appropriate functionalization route, self-assembled monolayers and carbon nanomembranes on an aluminized polyethylene terephthalate (PET) support were provided by CNM Technologies GmbH. The utilized precursor molecule also exhibits a terminal nitro group, which converts into an amino moiety after the cross-linking process. It was found that harsher reaction conditions are needed to successfully functionalize the CNM employing a reactive acyl chloride and a selective copper-free click chemistry [119]. The fabrication of the samples is described in detail in appendix B.

In figure 5.8a the subsequent stages of the reaction are displayed. The lone electron pair of the CNM's functional amino group (a) attacks the partially positively charged carbon atom of the linker molecule 2-azidoacetyl chloride (2-AAC) according to the mechanism of a nucleophilic acyl substitution. The elimination of the chloride anion follows and the removal of one proton bonded to the nitrogen leads to the formation of a stable peptide bond (b). The attached azide moiety easily reacts with the alkine of the sulfo-dibenzylcyclooctyne-biotin conjugate (SDBCOB) through a 1,3-dipolar cycloaddition forming a 1,2,3-triazole and coupling a biotin moiety to the carbon nanomembrane (c). It is known that biotin specifically interacts with certain proteins such as streptavidin due to its high affinity for them. The non-covalent interaction between the two components can be released by the intensive washing with *d*-desthiobiotin, which competes with biotin for the binding pocket of streptavidin. In this way a reversible immobilization of proteins exhibiting streptavidin should be achievable. Each step of the functionalization was checked by RAIRS and XPS measurements.

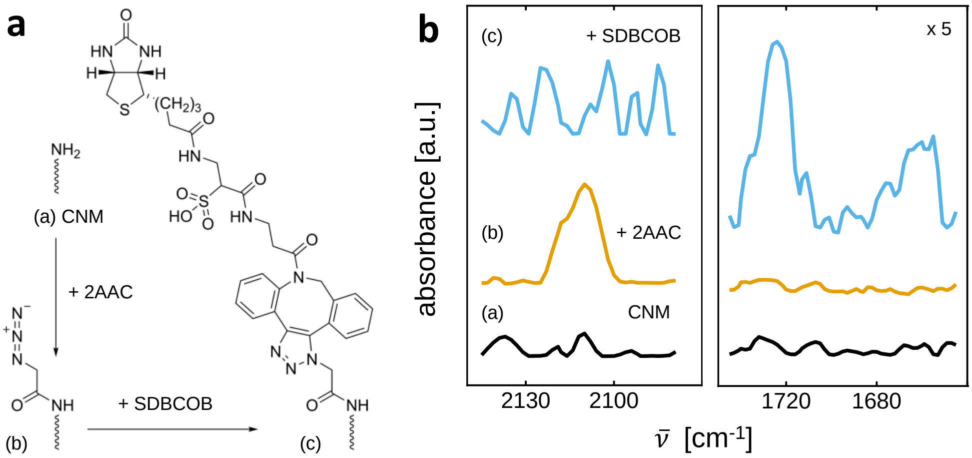

Figure 5.8.: (a) Schematic illustration of the attachment of a biotin moiety to CNMs using a copper-free click reaction employing 2-AAC and SDBCOB. (b) Corresponding RAIRS measurements of the different steps of the functionalization.

In figure 5.8b the relevant ranges of the infrared measurements are shown. The CNM (a) has no significant signals and displays only background noise within these limits. After the first reaction with 2-AAC the asymmetric stretching vibration of the azide moiety (b) is located at $\tilde{\nu} \sim 2110$ cm^{-1}. No signals for the secondary amide could be observed, which can be explained by the wrong alignment of its dipole with respect to the RAIRS measurement principle. The reaction with SDBCOB should cause the azide's asymmetric stretching vibration to disappear because it transforms into a 1,2,3-triazole. Consequently, the RAIRS spectrum (c) displays only background noise within this range. The five-membered cyclic ureide, -NH-C(O)-NH-, of the biotin moiety at $\tilde{\nu} \sim 1724\ \mathrm{cm}^{-1}$ is clearly distinguishable and the secondary amides give rise to "amide I band" vibrations around $\tilde{\nu} \sim 1665\ \mathrm{cm}^{-1}$.

Based on the previously presented RAIRS data a successful functionalization was very likely. The examination of the different steps using XPS measurements should furthermore verify this hypothesis. The XP spectra are displayed in figure 5.9 and explained in the following paragraph. Taking a look at the oxygen peak reveals no pronounced difference between the three reaction stages and it is noticeable that the O1s peak dominates all XP spectra. An explanation for this is the abundance of oxygen on the aluminized PET support in form of aluminum oxide. Hence, the contribution of the added oxygen atoms due to the functionalization is of no consequence.

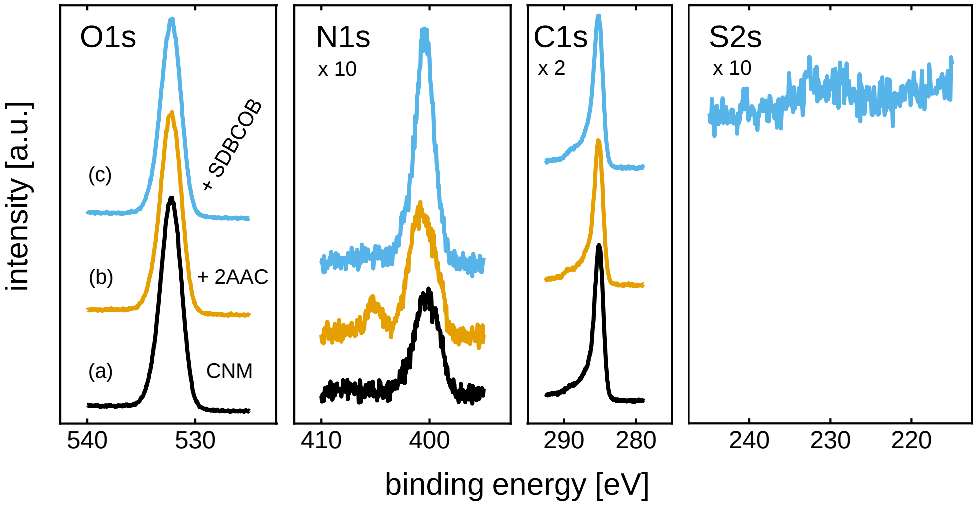

Figure 5.9.: XP spectra in the regions of oxygen, nitrogen, carbon and sulfur of each functionalization step starting from an amino-terminated CNM (a), which was further treated with 2-AAC (b) and SDBCOB (c).

The nitrogen peaks change from (a) to (c) and indicate the presence of different nitrogen species. The carbon nanomembrane (a) exhibits a N1s peak at

$\sim$ 400.1 eV, which is typical for functional amino groups. After the reaction with 2-AAC the main peak's intensity slightly increases and shifts to higher binding energies. The enhancement of the N1s peak originates from the addition of nitrogen atoms to the molecule. The shifting can be explained by the different chemical environment of the amide and the outer nitrogen atoms of the functional azide group. Additionally, a second peak at $\sim$ 405.2 eV appears, which can be attributed to the inner nitrogen atom of the azide moiety. The main signal rises further after the functionalization step with SDBCOB (c) and the energetically higher N1s peak of the functional azide group vanished. The observations are in accordance with the chemical structure, which further introduces five nitrogen atoms and binds the azide's nitrogen atoms in an 1,2,3-triazole moiety. The resulting nitrogen peak is a superposition of peaks arising from all the nitrogen atoms. The carbon peaks of the three reaction steps do not differ significantly from each other. They exhibit an asymmetric peak shape and are all broadened towards higher binding energies. Contrary to the expectations, the intensity does not increase from (a) to (c). Assuming a relatively low coupling yield and the effect of self-attenuation, the relative change in the carbon intensity would not be visible in contrast to the relative enhancement of the N1s peak. Nevertheless a slight shift of the C1s peak to higher binding energies and a more pronounced formation of a shoulder around 288.5 eV after the functionalization with SDBOCB could be posited, attributing the shift to the aliphatic hydrocarbons and the shoulder to the -C=O groups in the molecule. For the last step of the functionalization approach (c) a detailed scan of the sulfur S2s region was conducted because only the SDBCOB molecule contains a sulfonic acid and a thioether moiety. The respective XP spectrum reveals a weak peak at $\sim$ 231 eV supporting the presence of these functional groups. The presented XPS data, especially the N1s spectra, strengthened the assumption of a successful coupling to the carbon nanomembrane.

To verify the applicability of the functionalization strategy fluorescence measurements using streptavadin-Cy3 as a fluorophore were performed. The procedure is schematically shown in figure 5.10a. A SAM was patterned by using a brass mask during the electron irradiation, leading to a 3x3 array of circular areas, which were subsequently functionalized. Only these regions exhibit a CNM and should be capable of binding the streptavidin through the interaction with the biotin moiety. The rest of the sample remains a self-assembled monolayer and should not take part. The specimen was incubated with the streptavadin-Cy3 and an image was taken. The sample was imaged a second time after the extensive washing with *d*-desthiobiotin, which should replace the biotin moiety causing the elution of the fluorophore.

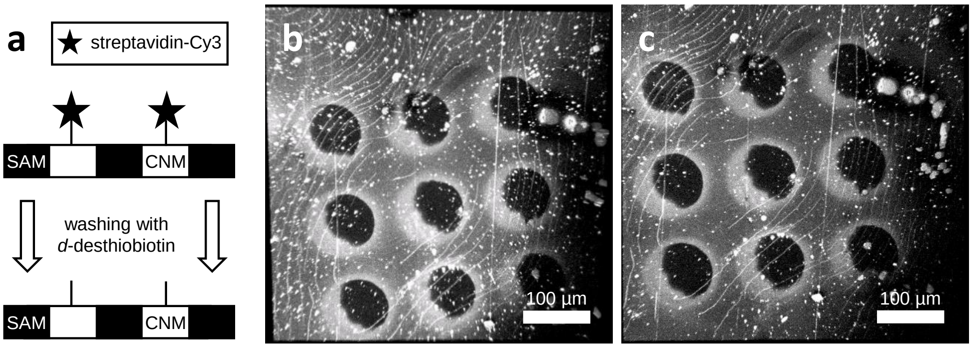

Figure 5.10.: (a)Schematic illustration of the patterned specimen and the experimental procedure. (b) Fluorescence image of the patterned CNM functionalized with biotin moieties and treated with streptavidin-Cy3. (c) The same sample after washing with *d*-desthiobiotin.

The results of the fluorescent measurements are presented in figure 5.10b/c. The image of the loaded specimen is displayed in (b). Although the unirradiated areas and the underlying lines of the supporting layer also exhibit a fluorescence signal, the pattern is still clearly visible. The functionalized regions show a brighter signal indicating a higher coupling density. The reason why all circles of the pattern have an area with a similar spatial orientation where no fluorescence signal is detectable is still unknown. Furthermore, it cannot be excluded that the mask contaminated the self-assembled monolayer, recognizable by the small particles on the specimen, which led to an unspecific binding of the streptavidin-Cy3. To avoid this, non-contact lithographic techniques could be used to generate a patterned CNM. After the treatment with *d*-desthiobiotin (figure 5.10c) the overall fluorescence signal lost intensity but did not disappear completely. Moreover, the unirradiated areas as well as the lines and particles still show a fluorescence signal. It can only be concluded that the conducted washing, and thus the replacement, was not effective enough to release the fluorophore. Streptavidin contains four binding sites for biotin. To detach the protein from the functionalized areas all of them need to be replaced by *d*-desthiobiotin at the same time. Otherwise, the functional biotin group competes with the eluant and will probably displace it again due to its high affinity so that the fluorophore remains on the surface. In order to obtain better results in future experiments the SAM should be replaced by a protein-repelling matrix of poly (ethylene glycol) leading to a darker background. Additionally, different washing strategies should be tested to achieve a better release of the streptavidin-Cy3.

The presented strategy of functionalizing a carbon nanomembrane with a functional biotin group in order to achieve a reversible protein immobilization through the interaction with streptavidin was verified by RAIRS and XPS measurements. The taken fluorescence images suggest that the method works in principle, but also revealed some points for improvement like, for instance, the reduction of the background signal or the coupling density of the linker molecules.

5.2.3. Irreversible Protein Immobilization

The superordinate aim is to develop a reliable immobilization strategy for proteins on both sides of the carbon nanomembrane. In principle, the employment of the copper-free click chemistry presented in the previous subsection seems to be an effective and reliable way to functionalize carbon nanomembranes.

It was shown that the immobilization through the interaction of biotin and streptavidin succeeded. However, strepatavidin is not universally applicable as a tag for the protein attachment due to its own complex molecular structure with respect to its linkage to the protein itself. Leaving the reversibility of the protein bonding aside, the key would be to simplify the protein's tag, which interacts with the CNM. The replacement of the relatively large and not universally attachable streptavidin tag by common cysteine moieties which interact with functional maleimide groups would lead to a simplified irreversible protein binding method. Hence, the CNM was functionalized according to figure 5.11a.

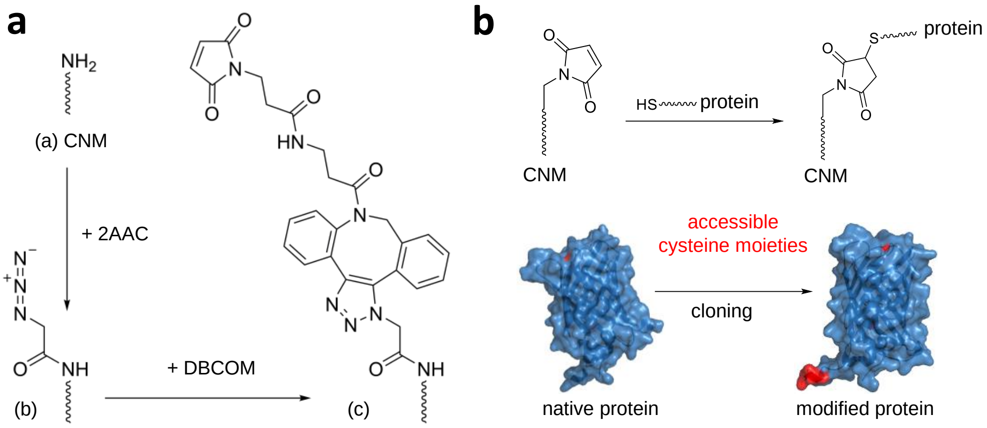

Figure 5.11.: (a) Schematic illustration of the attachment of a maleimide moiety to amino-terminated CNMs using a copper-free click reaction employing 2-AAC and DBCOM. (b) Reaction scheme between the maleimide-terminated CNM and the cysteine moieties of the GFP's derivatives (green fluorescent protein), as well as the representation of the accessible cysteine moieties (red shaded areas) of the utilizied proteins before and after cloning. The data of the protein's structures for generating the 3D models were taken from the protein data bank RCSB PDB [156].

In a first step the amino-terminated CNM (a) provided by CNM Technologies was treated with 2-azidoacetyl chloride (2-AAC) to obtain an azide moiety (b). The copper-free click chemistry was conducted with dibenzocyclooctyne-maleimide (DBCOM), introducing the desired functional maleimide group (c).

The fabrication of the specimen is described in detail in appendix B. The protein's accessible cysteine moieties exhibit -SH groups, which undergo a specific binding to the CNM's maleimide groups, resulting in stable, irreversible and covalent thioether bonds as displayed in figure 5.11b. Due to the bonding to the surface the maleimide moiety loses some degrees of freedom, which results in a diminished agility and a weaker reactivity. The utilized native proteins have some cysteine residues, which are marked red in the 3D model figure 5.11b. It is obvious that these are well embedded by other residues and therefore it could be difficult for the functional maleimide groups to reach an appropriate position to undergo a chemical reaction with those. As a consequence additional and easily accessible cysteine moieties were cloned to the native proteins in order to enhance the probability of the reaction.

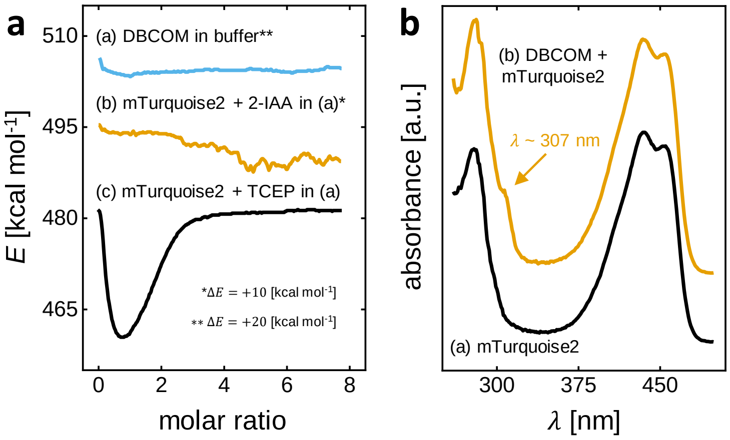

Figure 5.12.: (a) ITC measurements for the buffered DBCOM and DBCOM injected into mTurquoise2 in buffer solution containing 2-IAA or TCEP. (b) UV-VIS spectra of the pure mTurquoise2 and the adduct between the protein and DBCOM.

The reaction between the functional maleimide group and the native protein mTurquoise2 in the bulk phase was tested and monitored by ITC (figure 5.12a) and UV-VIS (figure 5.12b) measurements in advance to ensure that the formation of a stable thioether bond in principle occurs. For the ITC examinations the buffered DBCOM was injected into the buffer solution (a), as well as into buffered mTurquoise2 under reducing (b) and oxidizing conditions (c). 2-Iodoacetamide (2-IAA) and tris(2-carboxyethyl)phosphine (TCEP) were used as an oxidizing agent and reducing agent, respectively. The addition of DBCOM to the buffer solution causes no change in the ITC graph, proving no interaction of the DBCOM with the surrounding solution. 2-IAA forms a irreversible thioether bond with the protein and consequently inhibits a reaction with DBCOM. The corresponding data show almost no energy release indicating no reaction as expected. TCEP retains the original cystein residues avoiding the inactivation of the mTurquoise2 by the formation of disulfide bonds. The respective curve exhibits a significant decrease in the energy needed to keep the reaction compartment at the same temperature like the reference compartment, revealing a exothermic reaction between the maleimide moiety and the -SH groups.

The UV-VIS spectrum of mTurquoise2 was measured after the incubation with DBCOM and compared to the spectrum obtained for the pure protein. The corresponding UV-VIS spectrum in (b) exhibits an additional absorption band at ~ 307 nm, which is characteristic for the DBCO unit. [157, 158] Both methods independently verified the formation of an protein-DBCOM adduct through a thioether bond in the bulk phase. It was assumed that the modified protein should therefore show the same behavior with the surface-bonded functional maleimide groups.

The functionalization of the carbon nanomembrane was examined by RAIRS and XPS measurements as displayed in figure 5.13a and b, respectively. The RAIRS spectrum shows a peak at $\tilde{\nu} \sim 2114$ cm^{-1}, clearly indicating the presence of the azide moiety after the addition of 2-AAC (b), which was neither detectable on the amino-terminated CNM (a) nor on the with DBCOM further functionalized carbon nanomembrane (c). These observations allow the conclusion that the CNM exhibited an -N_3 group after the first functionalization step, which subsequently reacted with the DBCOM in a 1,3-dipolar cycloaddition, forming a 1,2,3-triazole causing the peak to disappear. The formed peptide bond between the amino moiety of the CNM and the acyl chloride give rise to the vibrations in (b) in the range of $\tilde{\nu} \sim 1610\ \mathrm{cm}^{-1}$ to $\sim 1675\ \mathrm{cm}^{-1}$. It is noticeable that the spectrum of the pure amino-terminated CNM showed some contaminations, which later on vanished or were overlaid by the vibrations of the secondary amide. After the copper-free click reaction the introduced amide moieties lead to an enhancement of the peaks in the respective region (c). However, the new peak at $\tilde{\nu} \sim 1713\ \mathrm{cm}^{-1}$ corresponds to the five-membered, cyclic imide moiety, proving the existence of the functional maleimide group in the final molecular structure.

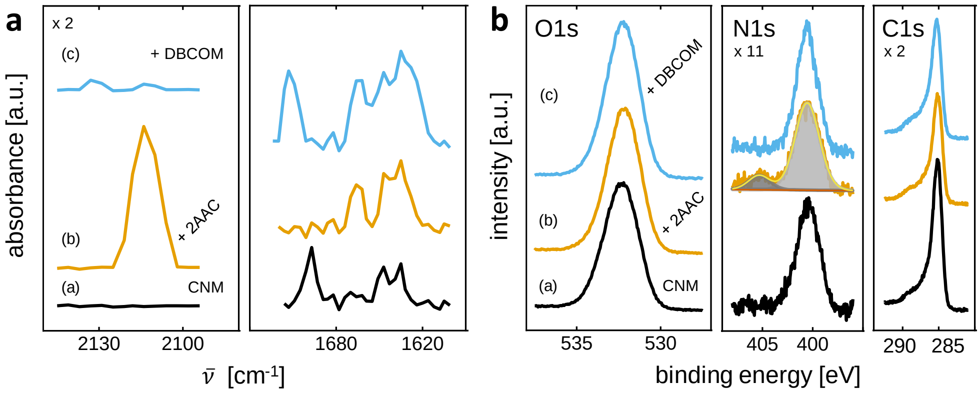

Figure 5.13.: (a) RAIRS measurement of the amino-terminated CNM (a) and the subsequent functionalization stages after the treatment with 2-AAC (b) and DBCOM (c). (b) Corresponding XP spectra in the regions of oxygen, nitrogen and carbon. The fits for estimating the coupling density of 2-AAC are shown.

The XP spectra given in figure 5.13b are dominated by the oxygen peak, which originates from the aluminum oxide of the underlying aluminized PET support, causing the functionalization to have no effect on the signal. The overall asymmetric shapes of the C1s peak of the different reaction stages (a) to (c) do not differ much from each other. The broadening to higher binding energies originates from oxidized carbon species and the main peak shows the presence of the carbon backbone. The reduced intensity after the treatment with 2-AAC can be explained by the release of attached contaminations, which were already visible in the RAIRS measurements. The constancy of the C1s spectra of (b) and (c) can be clarified as follows. Having a relatively low coupling yield, as known from subsection 5.2.2, and considering the self-attenuation of the carbon signal, the relative change in the carbon intensity traced back to the addition of carbon atoms would not be visible in contrast to the relative enhancement of the N1s peak. The nitrogen spectrum of the CNM (a) shows the typical peak of the functional amino groups at $\sim$ 400.5 eV. In (b) the peak for the azide's outer nitrogen atoms overlaps with the peak of the functional amide group located at the former position of the -NH_2 groups. The reduced intensity of the main peak compared to (a) can be attributed to detached contaminations containing both carbon and nitrogen atoms or to self-attenuation. The existence of the azide moiety is proven by the second peak at $\sim$ 405.2 eV, corresponding to the centered nitrogen atom of the functional group. By comparing the areas A of these two nitrogen peaks, one can estimate the coupling yield γ of the reaction according to equation (5.1). Under the assumption that self-attenuation can be neglected, a coupling yield of $\gamma \sim 21\,\%$ was found, which supports the aforementioned hypothesis.

$$\gamma = \frac{A_{405.2\,\mathrm{eV}}}{A_{400.5\,\mathrm{eV}} - 2A_{405.2\,\mathrm{eV}}} \tag{5.1}$$

After the coupling of the DBCOM to the CNM the energetically higher azide peak in the N1s spectrum is not observable anymore and the introduced nitrogen functionalities enhance the energetically lower peak. As with the RAIRS measurements, especially the nitrogen spectra support the assumption of the successful coupling of the functional maleimide group to the carbon nanomembrane.

Due to the progress in cloning, the immobilization of proteins on the functionalized CNM was first tested with the yellow fluorescent protein mVenus, which is structurally very similar to the previous investigated mTurquoise2. Additional cysteine moieties were added to the protein by cloning to increase the probability of the attachment. Drops containing a mixture of the modified mVenus with either TCEP (green circles in figure 5.14) or 2-IAA (red circles) have been placed on the specimen and after a latency time the sample was washed. Based on the results of the ITC and UV-VIS measurements it was expected that only fluorescent signals from the spots which were treated with the mixture of the modified mVenus and TCEP would be detectable. The areas on which drops containing the fluorescent protein and 2-IAA were placed, should not generate a signal. The cysteine residues should be inactivated and thus could not react with the functional maleimide groups.

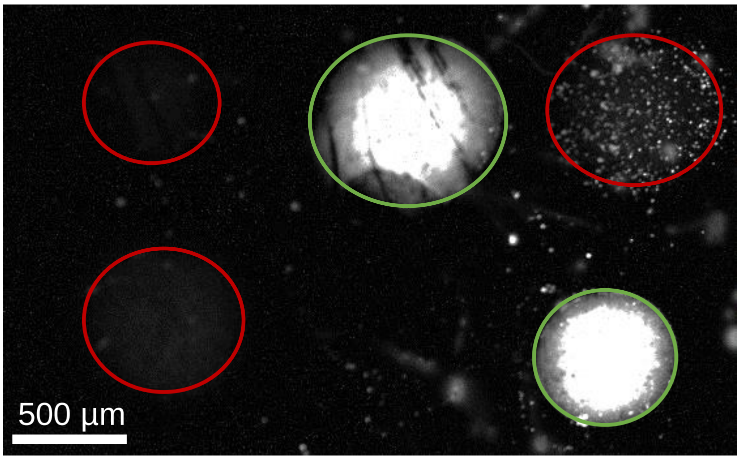

Figure 5.14.: Fluorescence image of a CNM functionalized with maeimide moieties and locally treated with drops of modified yellow fluorescent mVenus proteins. The green and red circles correspond to an added mixture of modified mVenus with TCEP and with 2-IAA, respectively.

In figure 5.14 the resulting fluorescent image is shown. As expected strong fluorescent signals are observable from the green-circled areas whereas in principle no signal originates from the red-circled regions. Isolated signals can be obtained from a red-circled area in the upper right corner of the fluorescent image. It is most likely that the signals originate from some defects in the PET support or from unspecific absorption as these features can also sporadically be seen in the background. The intensity of the respective fluorescent signals is significantly weaker compared to the bright intensity of the green-circled areas, where the modified mVenus is bonded through a thioether moiety. However, the fluorescent image clearly proves the successful irreversible coupling of the modified fluorescent protein and verifies the developed functionalization strategy. To achieve an even better distinction, the utilization of patterned CNMs in combination with a protein-repellant matrix should be considered. Furthermore, the experiment was so far only conducted with the modified mVenus and should be repeated with other proteins like the cyan fluorescent mTurquoise2.

5.2.4. Enhanced Coupling Density through Amino-Terminated Self-Assembled-Monolayers

In order to target the enhancement of the coupling density, the idea of using an amino-terminated self-assembled monolayer was developed. It was assumed that compared with the NBPT, more reactive functional amino groups would be available for the subsequent functionalization. The corresponding aromatic precursor molecule needed to be synthesized as it is not commercially available. To keep the synthesis effort as low as possible, it was decided to use the purchasable 4'-mercapto-[1,1'-biphenyl]-4-carbonitril as an educt for the reduction. The resulting precursor molecule 4'-(aminomethyl)-[1,1'-biphenyl]-4-thiol (AMBPT) and its oxidation-resistant derivate (4'-((methoxymethyl)thio)-[1,1'-biphenyl]-4-yl)methanamine (MOM-AMBPT) were synthesized by Nicole Wutke at the Max Planck Institute for Polymer Research in Mainz. NMR analyses which were conducted in Mainz confirmed the successful syntheses of the molecules. The chemical structures of the educt (a), the AMBPT (b) and the MOM-AMBPT (c) are shown in figure 5.15a.

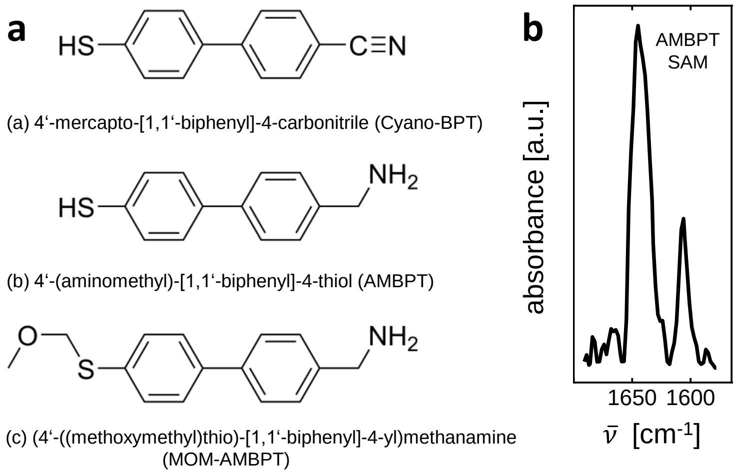

(a) 4'-mercapto-[1,1'-biphenyl]-4-carbonitrile (Cyano-BPT)

(b) 4'-(aminomethyl)-[1,1'-biphenyl]-4-thiol (AMBPT)

(c) (4'-((methoxymethyl)thio)-[1,1'-biphenyl]-4-yl)methanamine (MOM-AMBPT)

Figure 5.15.: (a) Chemical structures of the at the Max Planck Institute for Polymer Research in Mainz synthesized amino-terminated, aromatic precursor molecules AMBPT and MOM-AMBPT using Cyano-BPT as an educt. (b) RAIRS measurement of an AMBPT SAM.

The presented results were all obtained by utilizing the non-protected AMBPT as the precursor molecule because of the time course of the experiments. A detailed description of the specimen's preparation is given in appendix B.

Due to the first-time usage of the synthesized precursor molecule, it was necessary to examine whether (i) it is possible to form a SAM and (ii) the SAM results in a stable and transferable CNM after the electron irradiation. Spectroscopic evidence were obtained by RAIRS and XPS measurements. To check the transferability and the stability of the carbon nanomembrane, irradiated samples were transferred onto a silicon oxide wafer and onto quantifoil holey carbon foils on TEM grids, which exhibit free-standing areas, respectively. In figure 5.15b a RAIRS measurement of an AMBPT SAM is shown. The peak at $\tilde{\nu} \sim 1645$ cm^{-1} corresponds to the -N-H bending vibration and the one at $\tilde{\nu} \sim 1606$ cm^{-1} can probably be attributed to protonated functional amino groups. The protonation could be caused by coordinated water molecules. Thus, both peaks reveal the presence of functional amino moieties in the SAM and suggest a successful self-assembly.

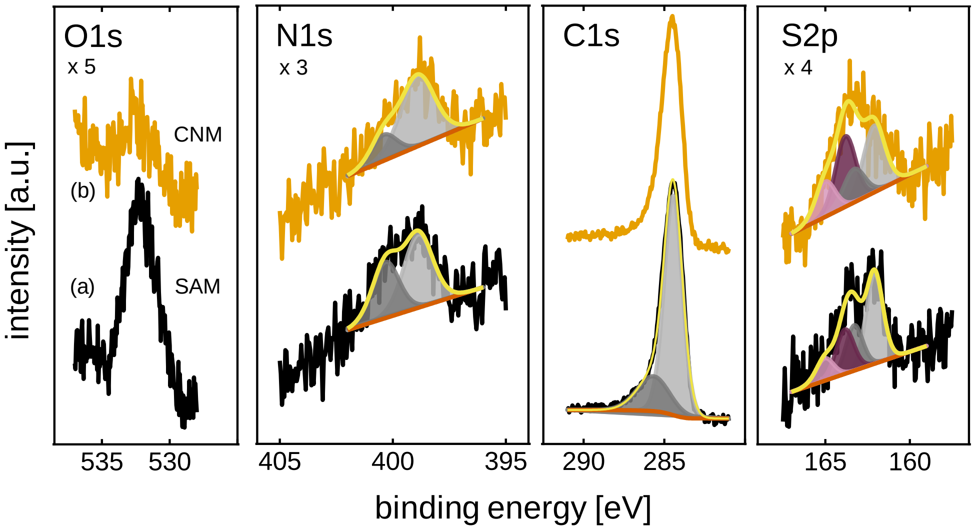

Figure 5.16.: XP spectra in the regions of oxygen, nitrogen, carbon and sulfur of the amino-terminated AMBPT SAM (a) and the corresponding CNM (b). Selected fits are displayed.

In figure 5.16 the XP spectra of an AMBPT SAM (a) and - after cross-linking in the ultrahigh vacuum - of the respective carbon nanomembrane (b) are given. The C1s spectrum of the SAM shows a peak, which can be described by the sum of two species. One originates at ∼ 284.5 eV and the other one at ∼ 285.7 eV corresponding to the aromatic carbon backbone and the carbon atoms bonded to sulfur and nitrogen, respectively. The sulfur spectrum clearly exhibits two doublets each with an energy separation of $\Delta E = 1.2$ eV with the S2p$_{3/2}$ peak located at ∼ 162.1 eV and at ∼ 163.8 eV. Besides the expected peaks of the bonds between the gold surface and the functional thiol groups, the latter doublet indicates the presence of unbonded thiols in the SAM. The N1s spectrum contains the characteristic peak of the functional amino groups at $\sim$ 398.9 eV and a second peak at $\sim$ 400.3 eV. Graf *et al.* [145] reviewed different bonding situations of amine precursor molecules on a gold surface including the protonation of the amino group of an Au-bonded compound and the hydrogen bonding between the amino moieties of the surface-bonded and unbonded precursor molecules. Additionally, oxidized nitrogen species (e.g. NHC=O) were considered in their study. The latter possibility was excluded as the reason for the second nitrogen peak due to the lack of the corresponding signal in the C1s spectrum around $\sim 287 - 288$ eV. Thus, it was attributed to protonated/coordinated amino moieties. The oxygen spectrum shows a peak caused by oxygen-containing adsorbates due to the exposure to ambient air.

After the irradiation of the SAM in the XPS system the carbon peak loses intensity because of a material loss. The evaluation of the attenuation of the gold signal reveals a decrease of the thickness by $\sim$ 3 Å from $\sim$ 12 Å for the AMBPT SAM to $\sim$ 9 Å for the CNM. It is known that this decrease is due to the irradiation damage of the self-assembled monolayer. On the other hand, the for the calculation utilized inelastic mean free path of the CNM was estimated to be the same as the one of the SAM. This assumption introduces some inaccuracies, which also affects the obtained value of the thickness, but it cannot be avoided due to the unknown λ_{IMFP}. However, the determined value of the AMBPT SAM is in a good agreement to the estimated thickness of $\sim$ 11 Å using Chem3D Professional 16.0.1.4 [159]. The overall intensity of the N1s peak slightly decreased, but it is noticeable that the peak for the protonated/coordinated amino moieties was reduced more strongly. Furthermore, the O1s peak was also degraded. Both observations can be explained by the irradiation-induced detachment of the coordinated precursor molecules and adsorbates, respectively. From the S2p spectrum it is obvious that the energetically higher doublet got more dominant after the cross-linking. This is known from previous investigations of CNMs, indicating the presence of sulfur species such as unbonded thiols, sulfide or disulfides due to the radiation. In summary, the XP spectra suggest the formation of a SAM by the usage of AMBPT as a precursor molecule. After the electron irradiation, the typical changes in the spectra could be observed indicating the cross-linking into a CNM.

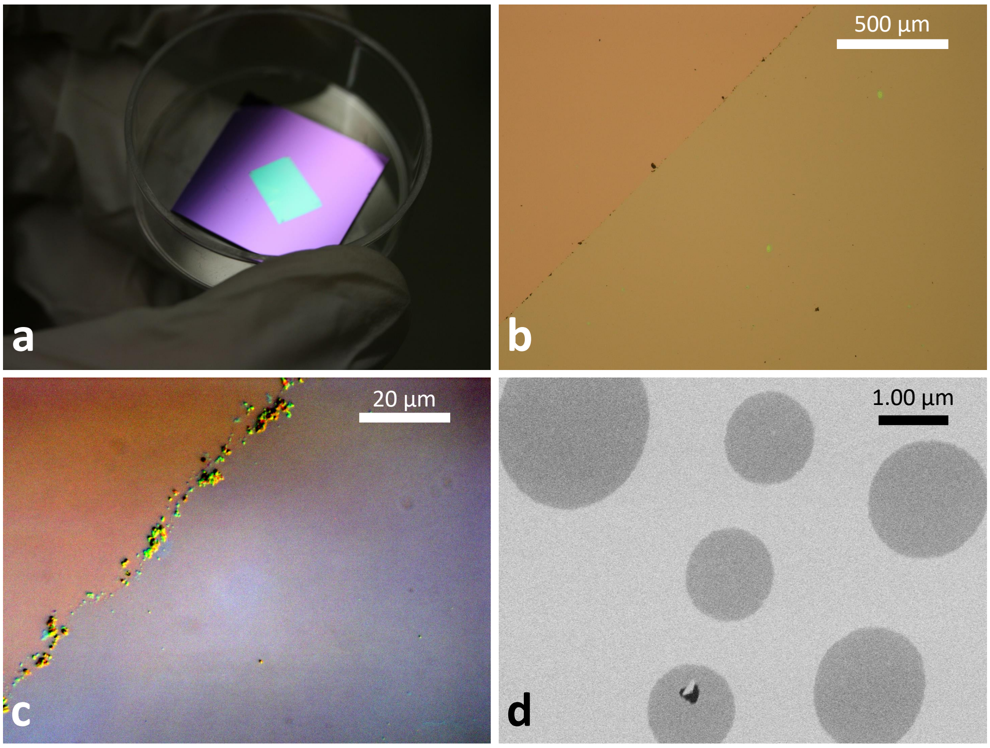

Figure 5.17.: Images of AMBPT CNMs on different supports. (a) to (c) on top of an silicon oxide wafer and (d) on a quantifoil holey carbon foil on a TEM grid. (a) Photography of the PMMA-coated AMBPT CNM. (b)/(c) Bright field microscopy images of the pure AMBPT CNM at magnification factors of 5x and 100x. The latter image was taken utilizing the DIC technique. (d) HIM image of a free-standing specimen measured in transmission mode.

The transferability of the CNM was checked in a next step, employing different supports. The PMMA-stabilized carbon nanomembrane was transferred onto a silicon oxide wafer as displayed in figure 5.17a. After dissolving the resist by acetone, the pure AMBPT CNM could be observed by bright field microscopy in (b) and (c). Additionally, some greenish dots, which might be residues of the PMMA, and some dark particles, mainly located at the border of the CNM, can be seen. At higher magnifications and by using the DIC technique the carbon nanomembrane is undoubtedly distinguishable. It exhibits a more bluish color in contrast to the surrounding silicon oxide wafer, which has a more reddish shade. At this scale no macroscopic defects could be seen. To verify the self-supporting character of the CNM a free-standing sample on a quantifoil holey carbon foil on a TEM grid was prepared and examined in the HIM using the transmission mode. In figure 5.17d the corresponding image, which proves the stability of the AMBPT CNM over different open areas, is given, nicely showing a defect in the lower part.

The successful preparation of a carbon nanomembrane from the amine precursor molecules was confirmed, enabling the study of the AMBPT's potential for further functionalizations. Having more reactive functional amino groups, which can undergo further chemical reactions, should result in a higher coupling density. This was subsequently investigated in cooperation with Nikolaus Meyerbröker (CNM Technologies) using both *N*-succinimidyl trifluoroacetate (TFA-NHS) and trifluoroacetic anhydride (TFAA). These molecules exhibit electron-poor carbon atoms due to the bonded electron-withdrawing groups and should be easily coupled to the AMBPT. The fluorine atoms facilitate the detection by XPS and in this way allow to monitor the coupling density.

In figure 5.18 typical XP spectra of a successful coupling are displayed. The bonded fluorine-containing group -CF_3 gives rise to peaks at $\sim$ 688.5 eV in the F1s spectrum and at $\sim$ 292.6 eV in the corresponding carbon spectrum. To determine the coupling density, the ratio of the areas of the fluorine and the nitrogen peak was calculated. The F1s area was divided by three in advance, considering that three fluorine atoms contribute to the respective XPS peak.

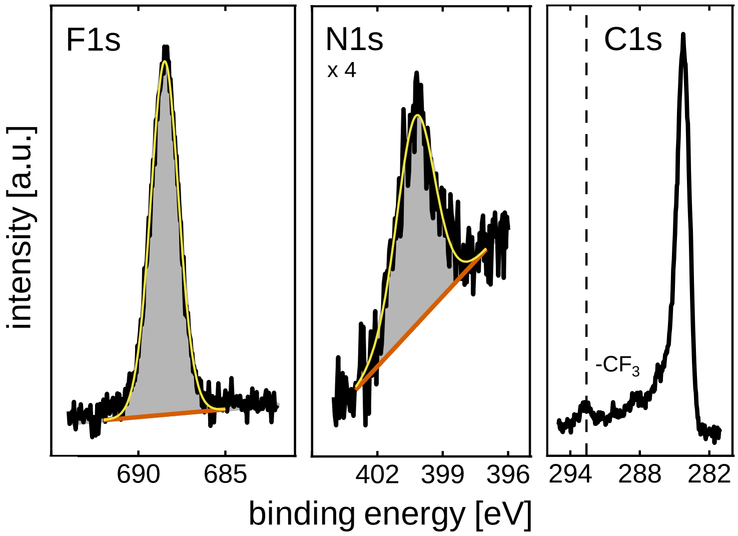

Figure 5.18.: XP spectra in the regions of fluorine, nitrogen and carbon of an amino-terminated AMBPT SAM after the treatment with TFAA. Fits which are relevant for the calculation of the coupling density are displayed.

Using the AMBPT SAM, coupling densities in the range of $\sim 0 - 12\,\%$ (TFA-NHS) and $\sim 55 - 73\,\%$ (TFAA) could be achieved, showing that the amino moieties were not able to substitute the NHS. Nevertheless, when employing TFAA, higher coupling densities could be realized. For comparison, the functional nitro groups of a standard SAM were converted into amino moieties by a chemical reduction. The subsequent reaction with TFAA results in coupling densities in the range of $\sim 69 - 75\,\%$, which are similar to the one of the AMBPT SAM. As a next step, the effect of the electron irradiation was studied. The SAMs were exposed to electrons and subsequently reacted with TFAA. The chemically reduced SAM had coupling densities around $29\,\%$ and thus showed a lower value compared to an irradiated standard nitro-terminated SAM ($\sim$ 39%). The same behavior is expected for the AMBPT, not resulting into a significant advantage for the chemical functionalization due to the SAM's similar coupling densities. The most likely explanation for the lower coupling densities of the amine SAMs is that during the established cross-linking procedure most of the -NH_2 moieties suffer from radiation damage, which leads to a fragmentation of the functional groups and to a desorption from the SAM. One way of tackling this issue in the future would be to find a milder (e.g. lower energies, doses) or more specific cross-linking method (e.g. utilization of photons) in order to conserve the functional amino groups without endangering the stability of the CNM.

However, the presented amino-terminated SAMs could for instance still serve as a pure reference specimen for the studies of Zhang *et al.* [27] who characterized the electronic transport behavior through NBPT SAMs and CNMs. Considering the possibility of the oxidation of the AMBPT's sulfur, the protected MOM-AMBPT, which was synthesized close to the end of the investigations, should be used for this purpose. Adding a small amount of trifluoroacetic acid to the solution of the MOM-protected AMBPT should lead to the cleavage of the protecting group and the following self-assembly process could be performed with nascent AMBPT molecules.

5.3. Summary of the Chapter

In this chapter different functionalization stratgies were explored to immobilize proteins on a carbon nanomembrane using either reversible or irreversible binding approaches.

In the first subsection the complex formation using l-lysine-NTA was investigated. It turned out that in principle the strategy worked but suffered greatly from the reproducibility of the onetime results. Because the reasons for this could not be clarified, other strategies were developed.

The copper-free click chemistry using 2-azidoacetyl chloride as the mediator molecule and dibenzocyclooctyne derivatives responsible for the interaction with the protein proved to be an efficient way. Two different approaches were examined.

The first one used the reversible binding of a streptavidin-tagged protein to a functional biotin moiety connected to the CNM. The taken fluorescent images revealed the coupling to the carbon nanomembrane but also showed some challenges related to the background signal and the coupling density. Consequently, attempts were made to enhance the coupling density of the proteins by the usage of amino-terminated self-assembled monolayers as a starting point, which is the topic of the chapter's last subsection. It was assumed that more reactive functional amino groups, which could be used for the further functionalization, would survive the irradiation with low energy electrons compared to the conventionally used nitro-terminated SAMs. After the verification of the carbon nanomembrane fabricated from the synthesized precursor molecule 4'-(aminomethyl)-[1,1'-biphenyl]-4-thiol (AMBPT) the coupling efficiency was evaluated. Unfortunately, the results showed no significant advantage compared to the standard CNMs. Nevertheless, the utilization of an aromatic, amino-terminated molecule extends the set of molecular building blocks which can be used for the successful fabrication of carbon nanomembranes.

The irreversible immobilization approach is based on the specific reaction between functional maleimide groups and thiol moities forming stable and covalent thioether bonds. In this case simple cysteine residues would act as the protein's tag. To compensate the diminished agility of the surface-bonded maleimide groups, the proteins were modified in the way that they exhibit easily accessible cysteine moieties. The evaluation of the patterned fluorescent image revealed an intense signal and thus a successful coupling in the expected areas.

In summary it can be stated that the irreversible protein binding strategy, which is described in the third subsection of this chapter, is the most promising way to achieve the designated objectives. It was shown that an attachment in the desired areas is possible.

Due to the intensive search of a reliable method for the protein immobilization using the CNM's functional amino groups, the exploration of an appropriate binding strategy for the thiol-terminated site of the carbon nanomembrane could not be performed. Considering the facts gained during this investigation, the usage of modified proteins containing a readily clonable cysteine-tag is assumed to be an effective way. The coupling to the functional thiol groups of the carbon nanomembrane might be achievable by utilizing either directly the -SH groups of the CNM and the protein's tag under oxidizing conditions or comparabily short, (asymmetric) maleimides as cross-linking agents. In the first case a direct disulfide bond (-S-S-) would be generated between the cysteine-tag and the carbon nanomembrane, whereas in the latter case the maleimides would form thioether bonds. For the verification of the coupling strategy transferred thiol-terminated CNMs should be used.

To achieve a Janus membrane, the following concept could be utilized: In a first step the amino-terminated side is functionalized using the presented copper-free click chemistry. Afterwards the CNM is transferred onto a silicon nitride membrane, which is embedded by a solid silicon substrate. For this purpose a silicon nitride membrane should be used in which a single orifice has been artificially generated, leading to a free-standing membrane area. This chip can be placed between two compartments as shown by Yang *et al.* [10]. Both compartments can be simultaneously filled with the respective protein and cross-linking agents under the right conditions. Afterwards the solutions can be exchanged by an appropriate buffer solution and the sample could be used for measurements. The adjustment of the compartments needs to be evaluated with respect to the specific investigation, but in this way a fabrication of a carbon nanomembrane with different functionalities on either sides would be imaginable.

6. Transport Processes through Carbon Nanomembranes

This three-part chapter outlines the investigations regarding the transport processes through carbon nanomembranes by now and demonstrates the applicability of radioactive tracers for determining the apparent diffusion coefficients through carbon nanomembranes in aqueous solution. First, the current state of the research is shortly presented and the motivation of the conducted experiments of the present thesis is given. Subsequently, the obtained findings are shown and evaluated with respect to the previous publications and the targeted aims. At the end of the chapter the results were summarized and suggestions for further investigations are given.

6.1. Current State of Research

The discovery of carbon nanomembranes as a novel molecularly-thin material gave rise to the question of its properties. Thinking of separation processes, the transport through carbon nanomembranes needed to be investigated to clarify its potential for applications in this field. In 2014, Ai *et al.* [39] started to examine the gas separating behavior of supported CNM composite membranes. As an underlying and stabilizing support polydimethylsiloxane (PDMS) thin film composite (TFC) membranes, which are known as highly gas permeable materials, were used. A HIM image of a such a composite is shown in figure 6.1a, where the two different materials are nicely distinguishable. A mathematical model which treats the contribution of the CNM and the PDMS layer to the overall permeance like the parallel circuit of resistors, facilitating the derivation of the pure permeance of the CNM P_{CNM} was proposed.

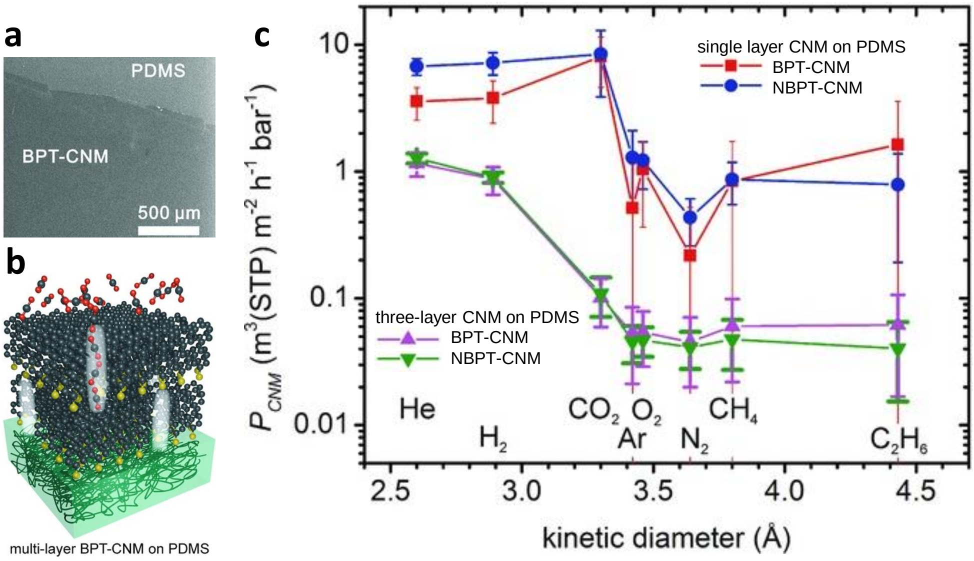

Figure 6.1.: (a) HIM image of a single layer BPT-CNM on PDMS support. (b) Schematic illustration of the gas transport mechanism in multi-layer CNMs. (c) Derived permeance of the pure carbon nanomembrane P_{CNM} from the data of the composite CNM-PDMS membrane. Reprinted and adapted with permission from Ai *et al.* [39]. Copyright 2014 Wiley-VCH Verlag GmbH & Co. KGaA, Weinheim.

Selected findings for single or multilayers of different carbon nanomembranes on PDMS are shown in figure 6.1c. Whereas larger gases with respect to their kinetic diameter e.g. Argon were blocked by the single layer, multilayers seem to shift this cut-off towards smaller values already hindering the passage of CO_2 besides the drop in the overall permeance. Based on these results a small lateral diffusion between the different layers of the CNM and the existence of molecular-sized channels (b) allowing the transport of small species were assumed.

The effect of different precursor molecules and the partial exchange of self-assembled monolayers which consist of oligophenylthiols by alkanethiols (mixed SAMs) on the composite was studied by Chinaryan [160]. It was found that the permeance is related to the molecular structure of the precursor molecule. Introduced nano-sized defects, which cause a decline of its separation ability, were proposed for the resulting composite of the mixed SAMs.

In 2018, Yang *et al.* [8] reported the investigation of free-standing carbon nanomembranes which were fabricated by the transfer onto a silicon nitride window with a single, well-defined orifice. As a mechanical support the Si_3N_4 window is embedded into a solid silicon chip. The permeation of a vapor originating from a liquid was studied by gravimetric analysis and the gas permeation was determined using the detection by a quadrupole mass spectrometer. Photographs of the respective experimental setups are shown in figure 6.2a/b.

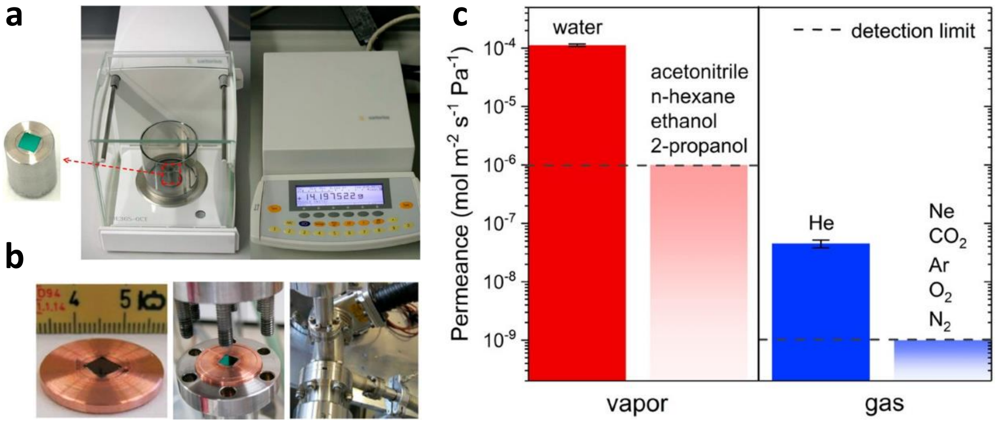

Figure 6.2.: (a)/(b) Photographs of the experimental setups of the gravimetric analysis and the gas permeation, respectively. (c) Permeances of different vapors and gases through TPT CNMs. Reprinted and adapted with permission from Yang *et al.* [8]. Copyright 2018 American Chemical Society.

It was found that for TPT CNMs only helium and water were able to permeate through the carbon nanomembrane (figure 6.2c), whereas the latter one remarkably displays a ~ 2500 times higher flux. Structural investigations suggested a carbon network with sub-nanometer channels. The upper limit of the pore diameter was determined to be (0.7 ± 0.1) nm allowing a cooperative rapid water permeation similar to the one one in carbon nanotubes or membrane proteins like aquaporins. Dementyev *et al.* [41] pushed the development of the experimental setup for the vapor permeation measurements, which enabled sophisticated investigations of mixtures. It was found that water assists the permeation of other gases [9] causing the suggestion of a phenomenological model for the permeation of gases and vapors through carbon nanomembranes. A following study on the permeation behavior through single and double layers of free-standing TPT CNMs using small, aliphatic alcohols' vapors led to the idea of the molecular jamming mechanism [42] refining the proposed model. However, the mentioned investigations in the gas phase indicated that CNMs could be a promising material for efficient separation processes.

In 2020, Yang *et al.* [10] recently demonstrated the separation ability of TPT CNMs in the liquid phase. Current-voltage characteristics and electrochemical impedance measurements were employed to investigate the rejection of ions and the corresponding resistances, respectively. In figure 6.3 the schematic depictions and results are displayed. The current-voltage characteristic for a 1 M potassium chloride solution was compared to a sealed silicon chip and to apertures of different sizes for which HIM images were additionally provided. It was found that the result obtained for a CNM-covered aperture is indistinguishable from the one of a sealed silicon chip, whereas the references show a linear characteristic depending on the aperture's size. The associated calculated resistance for the TPT specimen is in the range of GΩ. Furthermore, different ionic species were measured by the electrochemical impedance method and the resistances were derived by the equivalent circuit model displayed in figure 6.3b. Interestingly, the obtained GΩ resistances for the samples covered by carbon nanomembranes revealed a correlation between the hydration radii of the utilized cations and the determined resistances. A bigger hydration radius corresponds to a higher resistance and thus to a reduced probability of passing through the carbon nanomembrane.

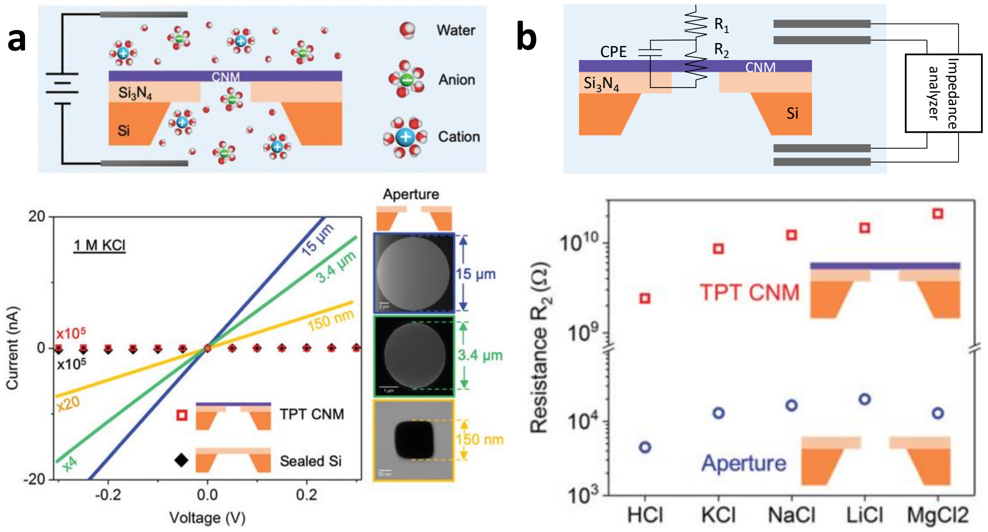

Figure 6.3.: (a) Upper panel: Schematic illustration of the experimental setup for determining the current-voltage characteristic of free-standing CNMs. Bottom panel: Selected results for a 1 M potassium chloride solution. (b) Upper panel: Schematic depiction of the electrochemical impedance measurements of free-standing CNMs with the applied equivalent circuit model. Bottom panel: Resulting resistances of different ions. Reprinted and adapted from Yang *et al.* [10]. Copyright 2020. Published by Wiley-VCH Verlag GmbH & Co. KGaA, Weinheim.

The ionic exclusion of carbon nanomembranes consequently led to experiments concerned with the application in forward osmosis (FO). Supported double-layer TPT CNMs were used for reasons of stability, not affecting the general permeation behavior. The experimental setup is schematically shown in figure 6.4a, which also displays the hypothesis that water permeates through the CNM in a single-file motion. Yang *et al.* nicely demonstrated that by time a draw solution of sodium chloride became diluted and the corresponding feed solution concentrated. The directed water transport to the draw side caused changes in the fluid levels - meaning a rise on the draw side and a decline on the feed side. Video evidence was attached to their publication and the respective time-depended concentrations are provided in figure 6.4b.

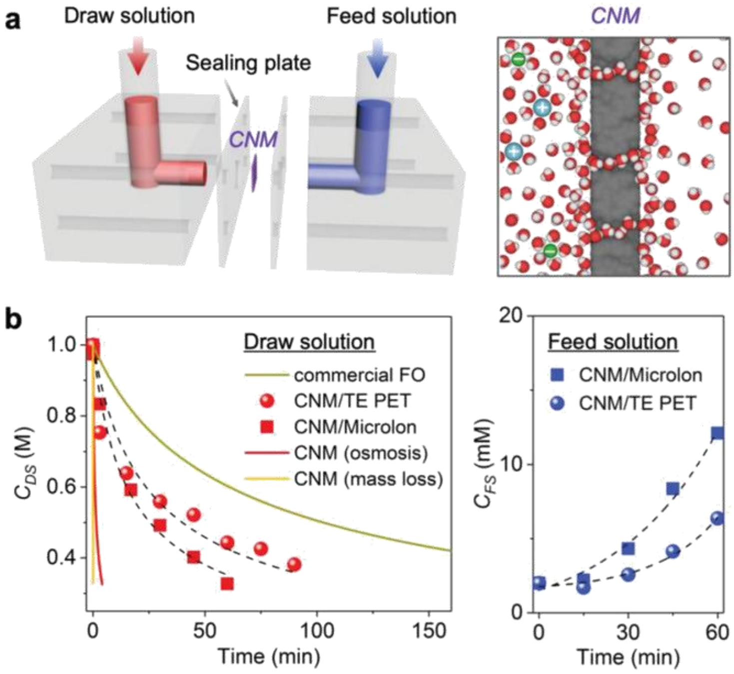

Figure 6.4.: (a) Schematic illustrations of the forward osmosis experiment with supported double-layer CNMs and the assumed osmotic process. (b) Time-depended sodium chloride concentrations of the draw ($c_{t=0} = 1\,\mathrm{M}$) and the feed solution ($c_{t=0} = 2\,\mathrm{mM}$). Reprinted and adapted from Yang *et al.* [10]. Copyright 2020. Published by Wiley-VCH Verlag GmbH & Co. KGaA, Weinheim.

For a CNM-Microlon composite the salt concentration of the 1 M NaCl draw solution dropped to 0.3 M within sixty minutes with a simultaneous increase of the feed solution's salt concentration from 2 mM to ∼ 12 mM. Similar results were obtained for the "track etched" polyethylene terephthalate (TE PET) supported specimen. The comparison with commercial FO membranes clearly demonstrates the superiority of the carbon nanomembranes and draws now the attention to the challenge of fabricating large-scale composites which can be used on an industrial level.

The presented investigations outline the development from the quantitative determination of permeating gaseous and ionic species associated with the establishment of a phenomenological model to the fabrication of a proof-of-concept prototype for forward osmosis applications. However, permeation can only be investigated so far in the gas phase or for charged molecules in the liquid phase. Consequently, the quantification through derived diffusion coefficients can exclusively be done for these cases. The aim of the investigations presented in this chapter is to explore the usage of radioisotopes in aqueous solution in order to find a more universally applicable method to determine the apparent diffusion coefficients through carbon nanomembranes. Advantages of this method would be a high sensitivity and the ability of tagging almost every molecule of interest as well as the simultaneous measurement of multiple differently marked components. The successful implementation would extend the available analytical methods for characterizing the carbon nanomembranes' material properties and facilitate a comparable easy way of screening for permeating species. Free-standing TPT CNMs were used to ensure the comparability to the previous examinations. The design of the measurement cell and the general experimental conditions were adapted from Yang *et al.* [10]. Hydrogen-3 (^{3}H, tritiated water), carbon-14 (^{14}C, sodium bicarbonate) and phosphorus-32 (^{32}P, phosphoric acid) served as a test system and the radioactive tracers were monitored by liquid scintillation counting.

6.2. Aqueous Apparent Diffusion Coefficients Determined by Radioactive Tracers

The following results were obtained in cooperation with Anna Dreyer from Plant Biochemistry and Physiology of the Faculty of Biology of Bielefeld University. The handling of the radioisotopes and the acquisition of the time-dependent tracer counts were done by her.

Based on the results of the following subsections, a publication was submitted to the peer-reviewed scientific journal *The Journal of Physical Chemistry Letters.* The subsequent contents associated with this topic are reprinted and partly adapted with permission from Dalpke, R., Dreyer, A., Korzetz, R., Dietz, K.-J. & Beyer, A. Selective Diffusion of CO_2 and H_2O through Carbon Nanomembranes in Aqueous Solution as Studied with Radioactive Tracers. *The Journal of Physical Chemistry Letters*, Manuscript ID: jz-2020-018217. Submitted and under review (2020). Copyright 2020 American Chemical Society. Repeated citations after each individual content are omitted.

6.2.1. Experimental Setup

As stated above, the design of the utilized permeation container was adapted from Yang *et al.* [10]. In figure 6.5 a schematic illustration (a) and a photograph (b) of the experimental setup are shown. The employed permeation cell exhibits an acceptor and a donor compartment, each having a capacity of $V \sim 88$ µl. The compartments were filled with a mineral oil-covered buffer solution (pH $=$ 7) and separated by a free-standing carbon nanomembrane with a diameter of $d \sim 7$ µm on a silicon nitride window, which was embedded into a solid silicon chip. Hydrogen-3 (^{3}H, tritiated water), carbon-14 (^{14}C, sodium bicarbonate) and phosphorus-32 (^{32}P, phosphoric acid) were purchased as radioactive components. The reason for this was the known good discriminability in energy of the radioisotopes during the liquid scintillation counting.

After the addition of the radioactive tracers to the donor compartment of the permeation cell, diffusion to the acceptor side occurs. The general procedure was to determine the concentration of the respective radioisotopes in both compartments after specific time intervals. The detailed description of the specimen's fabrication and the precise measurement procedure are provided in appendix B.

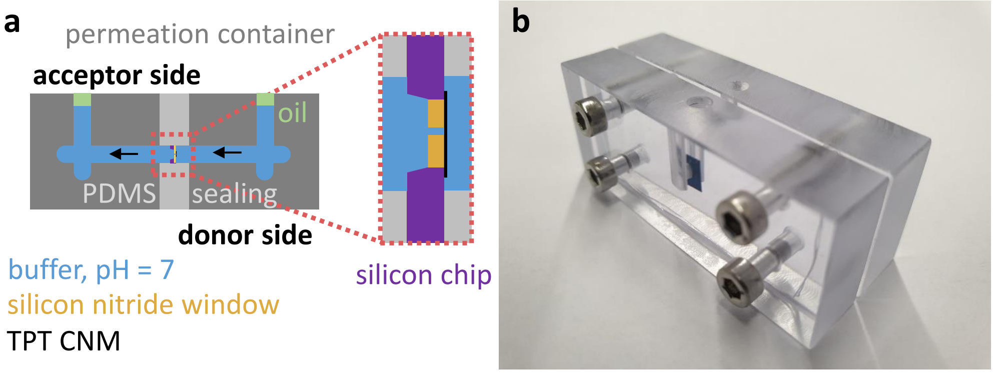

Figure 6.5.: (a) Schematic depiction of the radioisotope diffusion experiment. The tracer molecules were added to the donor compartment. Diffusion occurs through the TPT CNM to the acceptor compartment. (b) Photograph of a typical permeation container based on the design of Yang *et al.* [10] including a mounted specimen.

The initial activities of the radioisotopes were set to be $A(^{3}\text{H}) = 2$ µCi, $A(^{14}\text{C}) = 6$ µCi and $A(^{32}\text{P}) = 1$ µCi. In the course of some preliminary investigations an interference between the ^{3}H and ^{14}C has been found during the evaluation of the acquired scintillation data. As a consequence the obtained carbon-14 data were overcorrected and not usable in a sensible way. To tackle this issue the ^{3}H and ^{14}C radioisotopes were investigated separately with ^{32}P as an internal control agent. Reference measurements were conducted by using an open orifice to separate the two compartments from each other. In order to be able to take the outgassing of the radioactive tracers into account, preliminary investigations were conducted. These experiments exhibited starting activities of $A(^{14}\text{C}) = (2 \text{ to } 10)$ µCi and were performed in a permeation cells with sealed silicon chips.

6.2.2. Mathematical Model

A mathematical model to describe the radioisotope's time-dependent concentration, which incorporates the tracer loss, was developed and its complete derivation is given in appendix C. In equation (6.1) the differential equation for the time-dependent concentration, which is composed of two distinct terms, is shown. The left hand side considers the outgassing behavior and the right hand side represents the occurring diffusion, which has in this case a positive algebraic sign when describing the acceptor compartment. The conversion of the detected activities to concentrations was done by the division with the specific activity of the respective radioisotope and the volume of the specimen.

$$\frac{\mathrm{d}C_{\mathrm{A/D}}}{\mathrm{d}t} = -kC_{\mathrm{A/D}} \pm D'\frac{\partial C}{\partial x} \cdot \frac{A}{V} \tag{6.1}$$

$C_{\mathrm{A/D}}$ is the bulk concentration in the acceptor or donor compartment, t the time, k the outgassing constant, D' the apparent diffusion coefficient, $\partial C/\partial x$ the concentration gradient across the orifice, A the effective diffusion membrane area and V the compartment volume. The utilization of suitably selected boundary conditions results in the solution displayed in equation (6.2).

$$C_{\mathrm{A/D}} = \frac{C_0}{2}\exp(-kt)\left[1 \mp \exp\left(-\frac{2D'A}{Vd}t\right)\right] \tag{6.2}$$

The parameters C_0, d and a are the initial concentration in the donor compartment, the thickness of the membrane and the radius of the effective diffusion membrane area, respectively. The introduction of a correction factor f as shown in equation (6.3) takes the effect of concentration polarization into account where the concentrations at the membrane's surface and bulk differ from each other. It was found that f can be calculated from the geometrical factors d and a (radius of the orifice) and the ratio of the fluxes F/F_{Ref} through a membrane and an open orifice. This ratio is derivable from the respective ratio of the radioisotopes' activities in the acceptor compartment. In this investigation the ratio was calculated for the last taken data point.

$$f = 1 - \left(1 - \frac{2d}{\pi a}\right) \frac{F}{F_{\mathrm{Ref}}} \tag{6.3}$$

The combination of the correction factor f with equation (6.2) slightly modifies the expression and yields the final equation (6.4) for the description of the radioisotopes' concentrations.

$$C_{\mathrm{A/D}} = \frac{C_0}{2} \exp(-kt) \left[1 \mp \exp\left(-2f\frac{D'A}{Vd}t\right)\right] \tag{6.4}$$

Rearrangement of the former equation leads to a linearization of the expression with respect to time as displayed in equation (6.5), facilitating the direct calculation of the apparent diffusion coefficient D' from the slope as all other parameters are known.

$$\ln\left[-\frac{2C_{\mathrm{A}}}{C_0 \exp(-kt)} + 1\right] = -\frac{2fD'A}{Vd}t \tag{6.5}$$

6.2.3. Preliminary Investigation of Outgassing Effects

Sodium bicarbonate contains the carbon-14 radioisotope and is predominantly present as the ionic bicarbonate ($\sim 86\,\%$) under the experimental conditions according to the Henderson-Hasselbalch equation. In the buffered aqueous solution this HCO_3^- ion is in equilibrium with neutral, gaseous carbon dioxide (CO_2), which is able to leave the system through outgassing, leading to a loss of tracer material. The permeation cell was not sealed due to reasons of the carbon nanomembrane's stability. Therefore, a layer of mineral oil at the air-liquid interface was used to reduce the outgassing of the radioisotopes. Closed silicon chips - meaning without an orifice - were used to separate the compartments of the permeation cell during the preliminary investigation of the outgassing effect.

The obtained results for the different starting activities of the sodium bicarbonate are shown in figure 6.6a. Despite the overlay with mineral oil, the concentrations decrease with time, which means that the covering cannot prevent the outgassing effect. The exponential curve shapes of the time-dependent tracer concentrations are obvious. Therefore, a first order exponential decay was fitted to the data to obtain the respective outgassing constants k, which are displayed in figure 6.6b. The rate constants for the three lower activities show the same constant value, whereas the k for the higher initial activities decrease with increasing amount of the radioisotope. The reason for this could be a nonlinear dependence of the thermodynamic activities on the concentrations, which would affect the respective rate constants. The averaging of the similar outgassing constants (gray-shaded) result in a mean rate constant of $\bar{k} = (2.76 \pm 0.17) \cdot 10^{-2}\ \mathrm{h}^{-1}$.

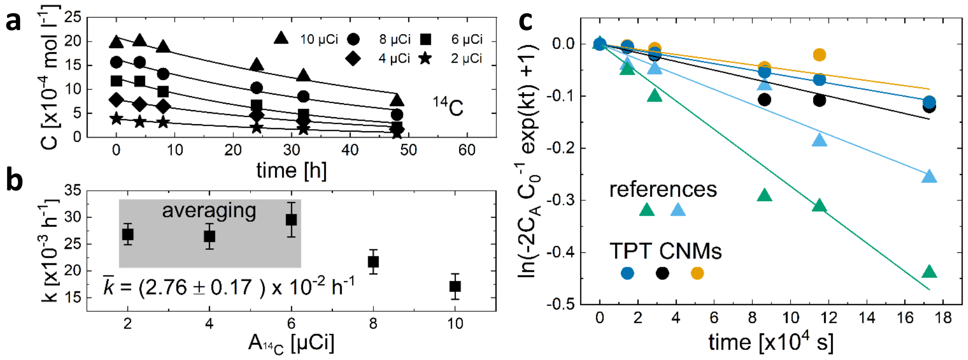

Figure 6.6.: (a) Time-dependent concentrations of the carbon-14 radioisotope for different initial activities. Two data sets were averaged for each activity. (b) Derived outgassing constants from (a) displayed with their respective fitting errors. The gray-shaded constants were averaged to determine the mean outgassing constant. (c) Experimental data of the acceptor compartment of the carbon-14 radioisotope plotted and fitted according to equation (6.5).

To test the applicability of the presented model the results of the carbon-14 diffusion and reference measurements were plotted in figure 6.6c according to equation (6.5) for which now every parameter except the apparent diffusion coefficient D' is known. In these cases the measurements were conducted with a CNM-covered silicon chip (diffusion experiment) and with an open orifice (reference experiment). Only the values of the acceptor compartment were considered due to the better distinguishability of the change in concentration. As it was expected, the model describes the linear dependence of the radioisotopes' data very well and validates the derived mathematical description. The acquired data for the hydrogen-3 and phosphorus-32 were processed in the same way to extract the respective apparent diffusion coefficients. It is important to note that for the cases of the ^{3}H and ^{32}P no outgassing occurs. Thus, the rate constant has been set to be zero, leading to the exponential function having a value of one.

6.2.4. Diffusion of Radioisotopes through CNMs in Aqueous Solution

As aforementioned, two sets of experiments for hydrogen-3 and carbon-14 have been performed independently from each other. The radioisotope ^{32}P was present in both cases. For the diffusion experiment a CNM-covered silicon chip and for the reference measurements an open orifice was used. After the derivation of each apparent diffusion coefficient using the linearized equation (6.5) the data have been plotted and the calculated curves of the time-dependent tracer concentrations of the acceptor compartments according to equation (6.4) were displayed. The obtained graphs are given in figure 6.7. It is noticeable that the error in the concentration is only visible for the ^{32}P data of the TPT CNMs. For each of the radioisotopes hydrogen-3 and carbon-14 three TPT CNMs and two references have been measured. Consequently, six samples and four references were investigated in total for the phosphorus-32.

In figure 6.7a/b the profiles of ^{3}H and ^{14}C are shown. It is clear to see that the model describes the measured data very well. The reference concentrations are in both cases higher compared to the ones of the CNM-covered samples, indicating that the diffusion of the radioisotopes is hindered by the carbon nanomembrane.

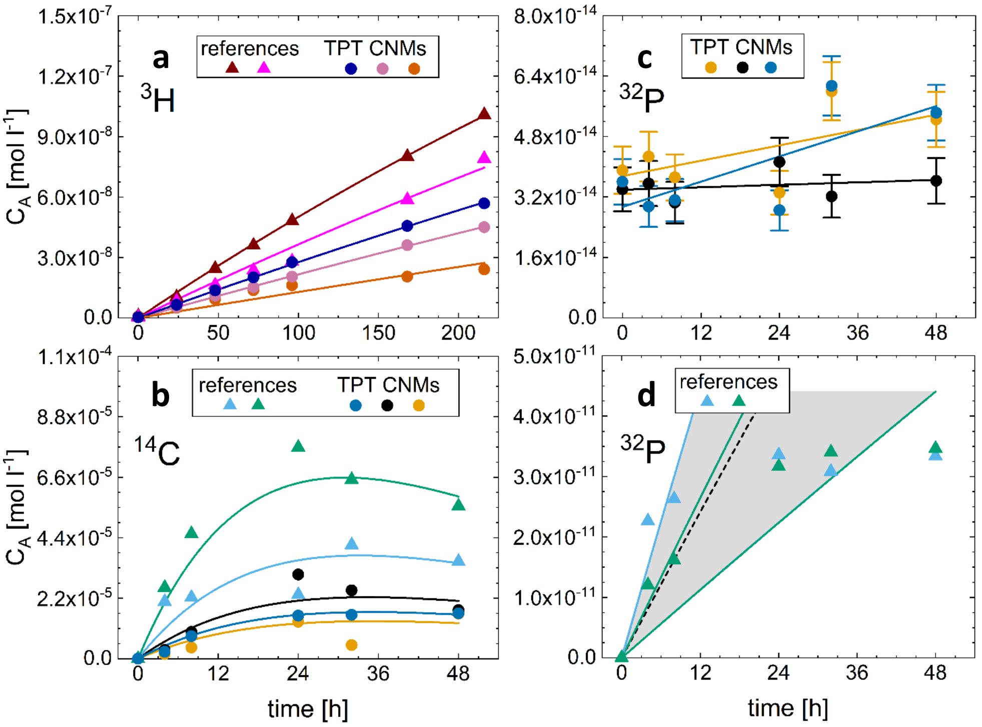

Figure 6.7.: Time-dependent acceptor compartment concentration of the radioisotope (a) hydrogen-3 (b) carbon-14, and (c)/(d) phosphorus-32. The measurements for the ^{32}P of typical references and TPT CNMs were displayed separately for a better visualization. The data in (c) are shown with their calculated error in the concentration. Fits according to equation (6.4) of the mathematical model were utilized to generate the time-dependent curves. In (d) each reference data set was modeled by two curves. The left ones only considered the first three data points for the extraction of the apparent diffusion coefficient according to equation (6.5), whereas the right ones used all available values. The gray-shaded area consequently displays the range of all possible curves. The dashed line represents the curve of the assumed mean apparent diffusion coefficient of the two references.

In the data of the carbon-14 tracer molecule two regions can be nicely identified. At early time stages the concentration increases due to diffusive transport of the radioisotope through the TPT CNM, whereas later on the outgassing dominates the ^{14}C causing the concentration's saturation. As expected from previous studies the tritiated water diffuses from the donor compartment through the TPT CNM to the acceptor compartment. Interestingly, the carbon-14 radioisotope is also able to pass the carbon nanomembrane.

Typical results of the conducted investigations of the ^{32}P tracer are given in panels c and d of figure 6.7. The obtained concentrations for the CNM-covered specimens are considered to be constant within the displayed errors and over the observed time period. It can be concluded that the phosphorus-32 is not able to pass through the TPT carbon nanomembrane or in other words that the ^{32}P radioisotope is blocked by the CNM. Thus, concentrations in the range of $C_{^{32}\mathrm{P}} \sim 80\,\mathrm{fmol\,l^{-1}}$ for phosphorus-32 are estimated as its specific detection limit of the method. To derive an upper boundary of the corresponding ^{32}P apparent diffusion coefficients, equation (6.4) has been extended with an offset in the same range as the limit of detection and was used for the determination of D'.

The aforementioned detection limit was specified as the seeming radioisotope's concentration of a blank measurement. Assuming the same activity, the detection limit is inversely proportional to the respective tracer's specific activity. For comparison, this results in specific detection limits for hydrogen-3 and carbon-14, which are three and six orders of magnitude higher compared to one of ^{32}P.

The reference measurements of the phosphorus-32 are given in figure 6.7d. The time-dependent concentrations show a similar trend as the carbon-14 data in panel b. It was expected that the concentration increases linearly with time as the one of the hydrogen-3 tracer. The apparent saturation of the values cannot be explained by outgassing effects compared to the ^{14}C. The half life of the phosphorous-32 radioisotope is $t_{1/2} \sim 14.3$ d and through a beta decay the ^{32}P results in the stable sulfur-32 isotope (^{32}S). [161] Using the first-order differential equation for a radioactive decay $\sim 10\,\%$ of the initial tracer molecules transmuted during the course of the experiments. The decay product sulfur-32 is not radioactive and thus cannot be monitored by liquid scintillation counting. The presented mathematical approach does not consider the tracer loss due to the nuclear transmutation. However, because of its comparably small amount, this effect cannot be the only reason why the plotted curves do not reproduce the obtained phosphorus-32 concentrations, but the actual cause could not be determined. In order to give a reasonable order of magnitude for the ^{32}P apparent diffusion coefficient through the carbon nanomembrane, two different cases were examined. The model was applied on the one hand to the few early data points which are assumed to follow a linear behavior and on the other hand to all available time-dependent concentrations, facilitating the determination of an upper and lower limit of the apparent diffusion coefficient. The range in between those is marked by the gray-shaded area in figure 6.7d. The black dashed line represents the resulting curve of the mean apparent diffusion coefficient. The determined apparent diffusion coefficients differ by a factor of three and for the comparison in figure 6.9, it was chosen to show D' which used all data points.

The applicability of the ^{32}P tracer as an internal control agent for the intactness of the carbon nanomembrane is shown in figure 6.8. The time-dependent concentrations of the acceptor compartment of a reference measurement through an open orifice, and of intact and defective CNM-covered openings are displayed in comparison. The data of the intact TPT CNM and the reference show a similar trend as already explained for the panels c and d of figure 6.7, respectively. Intuitively more tracer molecules should pass through the defective specimen compared to an intact sample. The time-dependent concentrations should converge to the values of the reference, depending on the total broken area of the sample. Accordingly, the corresponding values for the acceptor concentration of the defective specimen lies in between the open and covered orifice.

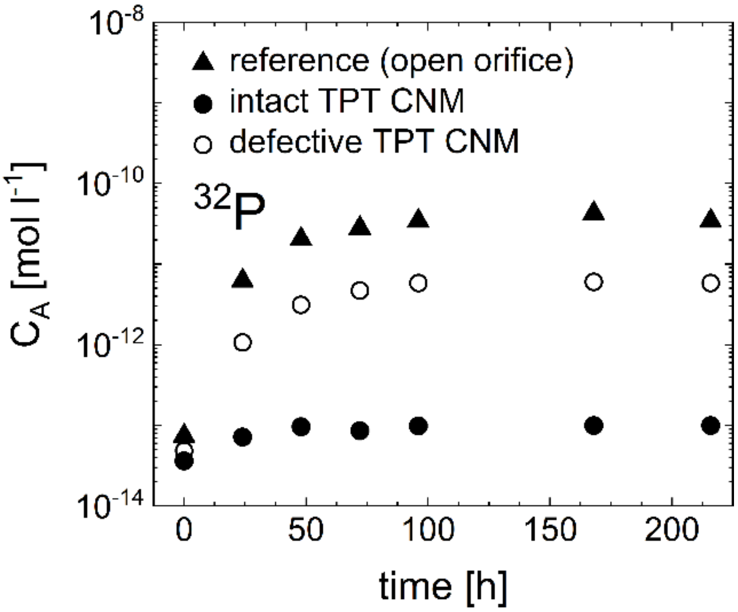

Figure 6.8.: Time-dependent acceptor compartment concentrations of the radioisotope phosphorus-32 for an reference measurement using an open orifice (black-filled triangles), as well as for an intact (black-filled circles) and defective TPT CNM (open circles).

To estimate the defective area A_{Def} of a partially defective specimen, equation (6.7), which has been fully derived in appendix C, was applied. The approach bases on Fick's law of diffusion which states that the flow rate Q through the specimen is proportional to its area A and concentration gradient $\partial C/\partial x$ as shown for both cases in equation (6.6). The first expression theoretically attributes the overall flow rate to two separate transport processes. Two cases can be distinguished: the flow rate through intact areas A_{Int} of the CNM and the one through defective, or in other words open areas. Assuming each term has an own, independent concentration gradient and apparent diffusion coefficient, the intact regions would behave like a totally intact CNM specimen with $D'_{\mathrm{CNM}}\,(\partial C_{\mathrm{CNM}}/\partial x)$ and the defective areas like an open orifice of a reference measurement with $D'_{\mathrm{Ref}}\,(\partial C_{\mathrm{Ref}}/\partial x)$. On the other hand the flow rate during a real measurement considers the complete area of the specimen A_{Tot} and cannot differentiate between open and CNM-covered regions. The overall observable apparent diffusion coefficient D'_{Obs} contains contributions from both cases. The resulting expression is shown in the second equation. The defective area is furthermore defined as the difference of the total and intact area.

$$\begin{aligned} Q &= -\left(A_{\mathrm{Int}} D'_{\mathrm{CNM}} \frac{\partial C_{\mathrm{CNM}}}{\partial x} + A_{\mathrm{Def}} D'_{\mathrm{Ref}} \frac{\partial C_{\mathrm{Ref}}}{\partial x}\right) \\ Q &= -\left(A_{\mathrm{Tot}} D'_{\mathrm{Obs}}\right) \frac{\partial C}{\partial x} \end{aligned} \tag{6.6}$$

Because both descriptions of the flow rate are valid these can be equated. The different concentration gradients can be unified by utilizing the already introduced correction factor f, simplifying the expression for the ratio of the intact and total area to the following equation (6.7), which is directly related to the defective area of the specimen.

$$\begin{aligned} \frac{A_{\mathrm{Int}}}{A_{\mathrm{Tot}}} &= \frac{f_{\mathrm{Ref}} D'_{\mathrm{Ref}} - f_{\mathrm{Obs}} D'_{\mathrm{Obs}}}{f_{\mathrm{Ref}} D'_{\mathrm{Ref}} - f_{\mathrm{Int}} D'_{\mathrm{CNM}}} \\ \frac{A_{\mathrm{Def}}}{A_{\mathrm{Tot}}} &= 1 - \frac{A_{\mathrm{Int}}}{A_{\mathrm{Tot}}} \end{aligned} \tag{6.7}$$

By knowing the appropriate values for $f_{\mathrm{Ref}} D'_{\mathrm{Ref}}$ and $f_{\mathrm{Int}} D'_{\mathrm{CNM}}$ from measurements of reference and intact specimens of the same batch, the defective area is easily obtainable from the observed parameters $f_{\mathrm{Obs}} D'_{\mathrm{Obs}}$ of the partially defective sample under investigation.

The defective area's fraction of the partially broken, free-standing TPT specimen in figure 6.8 was determined to be $A_{\mathrm{Def}}/A_{\mathrm{Tot}} \sim 12\,\%$. This value seems to be in a reasonable range. For comparison, Ai *et al.* [39] calculated values between 11 % and 25 % for the non-covered area of the used polymer-supported single-layer CNMs.

The apparent diffusion coefficients of the radioisotopes hydrogen-3, carbon-

14 and phosphorus-32 through an open orifice and a carbon nanomembrane which were obtained in the present thesis are shown in figure 6.9 and discussed in detail in the following paragraph. The values of at least three TPT CNM samples and not less than two open orifices have been averaged for each determination. Yang *et al.* [10] recently performed ion conductance measurements for different cations through TPT CNMs. From the conductivity the respective apparent diffusion coefficients were calculated by employing the Nernst-Einstein equation. The data are also shown for comparison and are most-likely the only available literature values for apparent diffusion coefficients through CNMs in aqueous solutions up to now.

The gray-shaded box represents the range of the apparent diffusion coefficients of the following listed ionic and neutral species in aqueous solution taken from the literature, assuming $K_\mathrm{L} = 1$: $\mathrm{H^+}$, $\mathrm{OH^-}$, $\mathrm{H_2PO_4^-}$, $\mathrm{HPO_4^{2-}}$, $\mathrm{PO_4^{3-}}$, $\mathrm{HCO_3^-}$, $\mathrm{NaCO_3^-}$, and $\mathrm{CO_3^{2-}}$ [162], $\mathrm{CO_2}$ [163], $\mathrm{H_2O}$ (self-diffusion) [164], THO [165], and $\mathrm{T_2O}$ (self-diffusion) [166].

The apparent diffusion coefficients of the reference measurements range all from $D'_\mathrm{Ref} \sim \left(10^{-9}\,\mathrm{to}\,10^{-8}\right)\mathrm{m^2\,s^{-1}}$, which agrees well with the displayed literature range and furthermore validates the reasonable design of the experiment with its evaluation procedure. It also strengthens the confidence in the reliability of the apparent diffusion coefficients determined for the intact CNM samples. It is obvious to see that the diffusive transport is hindered by the carbon nanomembrane. The apparent diffusion coefficients of the tracer molecules hydrogen-3 and carbon-14 deviate by four orders of magnitude compared to the measurements of the uncovered orifice, having values of $D'_{^3\mathrm{H}}(\mathrm{CNM}) \sim 10^{-13}\,\mathrm{m^2\,s^{-1}}$ and $D'_{^{14}\mathrm{C}}(\mathrm{CNM}) \sim 10^{-12}\,\mathrm{m^2\,s^{-1}}$, respectively. The radioisotope phosphorus-32 cannot diffuse through the TPT carbon nanomembrane, which acts in this case as an impermeable barrier. The estimated apparent diffusion coefficient $D'_{^{32}\mathrm{P}}(\mathrm{CNM}) \sim 10^{-16}\,\mathrm{m^2\,s^{-1}}$ is seven orders of magnitude lower compared to the reference measurements, which underlines the applicability of the ^{32}P as an internal control agent for the CNM's intactness and quality.

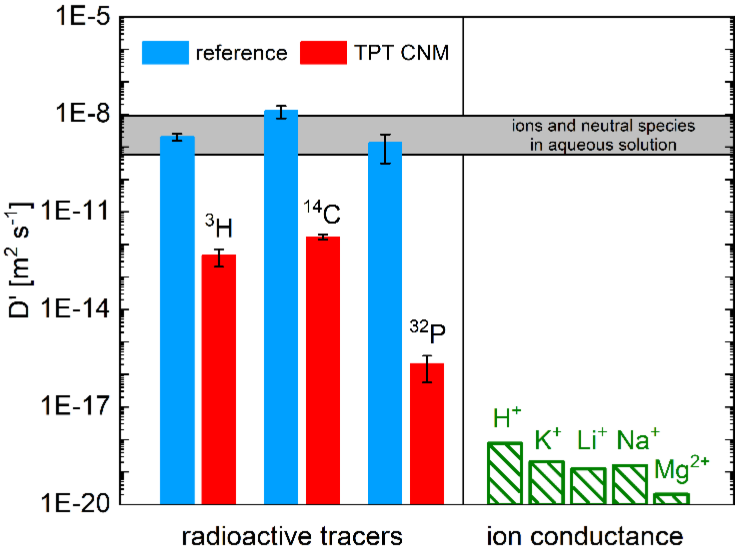

Figure 6.9.: Apparent diffusion coefficients of the three radioisotopes hydrogen-3, carbon-14 and phosphorus-32 through an open orifice (reference, blue) and through free-standing TPT CNMs (red) in aqueous solution obtained in the present thesis. Three TPT samples have been averaged for both ^{3}H and ^{14}C, and six samples for ^{32}P. Two references for the hydrogen-3 and carbon-14, and four open orifices for phosphorous-32 were measured. The errors represent the corresponding standard deviation. The apparent diffusion coefficients of the ionic species (green) were derived from Yang *et al.* [10]. The gray-shaded area represents the typical range of apparent diffusion coefficients in aqueous solutions taken from the literature [162–166], assuming $K_L = 1$.

The tracer molecules hydrogen-3 and carbon-14 are both able to pass the carbon nanomembrane, revealing its property as a semipermeable membrane. The selective transport behavior was shown in the literature before. It was reported that water and helium permeate through TPT CNMs while other gases, organic vapors and most ions are rejected by the carbon nanomembrane. [8, 10] The hindered permeation of ions through the CNM compared to neutral species gave rise to the idea that an electrostatic barrier, which opposes the passage of charged species, exists across the CNM. A carbon nanomembrane is basically an inhomogeneous carbon network. Computer simulations for the proton transport across carbon nanotubes were conducted by Dellago and Hummer [167]. It was found that a large electrostatic penalty arises due to the loss of the preferred eigenlike configuration $H_9O_4^+$. Studies about the proton transport utilizing the water channel protein aquaporin conclude similar outcomes. [168, 169] Thus, it can be assumed that such electrostatic effects also play a role for the transport of ions through CNMs, which would explain the comparatively low values of their apparent diffusion coefficients in figure 6.9. The determined apparent diffusion coefficient for ^3H is roughly six orders of magnitude higher than the one for H^+ which was extracted from the experiments of Yang *et al.* [10]. In combination with the previous stated observations this leads to the suggestion that the radioactive tracer hydrogen-3 diffuses as neutral water, most likely as THO, through the carbon nanomembrane. Due to its similar apparent diffusion coefficient in relation to the tritiated species it is most likely that the ^{14}C tracer permeates the TPT CNM as neutral CO_2 although the radioisotope carbon-14 has been introduced as sodium bicarbonate, which is mainly present as the bicarbonate ion. In fact, this hypothesis is supported by experiments of Gutknecht *et al.* [170] who investigated lipid bilayer membranes with carbon-14 tracers and whose results also indicated that the isotope crosses the membrane as neutral CO_2. In this case the lowered driving force due to the small amount of carbon dioxide ($\sim 14\,\%$) under the experimental conditions needs to be considered. The observed apparent diffusion coefficient was divided by the fraction of CO_2 in order to extract the apparent diffusion coefficient $D'_{^{14}CO_2}(\mathrm{CNM}) \sim 10^{-11}\,\mathrm{m^2\,s^{-1}}$. In the gas phase, the water-assisted permeation of carbon dioxide through TPT CNMs was further shown by Naberezhnyi *et al.* [9]. The derived apparent diffusion coefficient from their experiments is in the same order or magnitude. These findings substantiate the idea of neutral molecules to be the preferred carrier species through CNMs.

6.3. Summary of the Chapter

This chapter explored the possibility of using radioisotopes to determine the respective apparent diffusion coefficients through carbon nanomembranes in aqueous solution in order to find a more universal method for the investigation of permeating species compared to the ion conductance measurements. Free-standing TPT CNMs were utilized as a model system, facilitating the comparison to previous permeation studies in the gas and liquid phase. Tritiated water (hydrogen-3), sodium bicarbonate (carbon-14) and phosphoric acid (phosphorus-32) were used as tagged molecules. A mathematical model which considers the effects of concentration polarization and the carbon-14 tracer loss due to outgassing was developed. To the best of my knowledge this is the first time that the diffusion through a carbon nanomembrane in aqueous solution was studied with such a method.

It was found that the detection through liquid scintillation counting is a promising technique to investigate the semipermeable behavior of carbon nanomembranes. The derived apparent diffusion coefficients for open orifices in the range of $D'_{\mathrm{Ref}} \sim \left(10^{-9}\,\mathrm{to}\,10^{-8}\right)\mathrm{m^2\,s^{-1}}$ are in good agreement with the corresponding literature legitimating the experimental approach and the evaluation procedure.

As expected, the hydrogen-3 radioisotope diffuses through the TPT CNM. Intriguingly, the carbon-14 tracer was also detectable, having an apparent diffusion coefficient in the similar range like the ^{3}H containing component. The apparent diffusion coefficients are $D'_{^3\mathrm{H}}(\mathrm{CNM}) \sim 10^{-13}\,\mathrm{m^2\,s^{-1}}$ and $D'_{^{14}\mathrm{C}}(\mathrm{CNM}) \sim 10^{-12}\,\mathrm{m^2\,s^{-1}}$, respectively. The comparison with other studies indicates that most likely the radioisotopes carrier species through the CNM are neutral molecules. In the particular cases neutral water, most likely THO, and carbon dioxide are assumed to be the preferred carriers. For the ionic species electrostatic effects were considered to prevent a diffusive transport through the carbon nanomembrane. Considering the lowered driving force in the case of CO_2, the apparent diffusion coefficient $D'_{^{14}\mathrm{CO}_2}(\mathrm{CNM}) \sim 10^{-11}\,\mathrm{m}^2\,\mathrm{s}^{-1}$ was calculated.

The phosphorous-32 radioisotope was restrained by the TPT CNM allowing its employment as an internal control agent for the intactness and quality of the specimen. The respective apparent diffusion coefficient was estimated to be $D'_{^{32}\mathrm{P}}(\mathrm{CNM}) \sim 10^{-16}\,\mathrm{m}^2\,\mathrm{s}^{-1}$, leading to its specific detection limit of around $C(\mathrm{LOD})_{^{32}\mathrm{P}} \sim 80\,\mathrm{fmol\,l}^{-1}$ for this method. Under the same conditions, the limit of detection for the other radioisotopes was estimated to be in the range of $C(\mathrm{LOD})_{^{3}\mathrm{H}} \sim \mathrm{pmol\,l}^{-1}$ and $C(\mathrm{LOD})_{^{14}\mathrm{C}} \sim \mathrm{nmol\,l}^{-1}$, respectively. By using the ^{32}P tracer the fraction of the defective area of a partially broken sample was quantified to a reasonable value of $A_{\mathrm{Def}}/A_{\mathrm{Tot}} \sim 12\,\%$.

The obtained results demonstrated the method's proof-of-principle and revealed its capabilities. Still, for future investigations some challenges need to be overcome. The outgassing effect could be reduced by an appropriate sealing of the permeation cell. Additionally, the reason for the apparent saturation of the phosphorus-32 needs to be identified and understood, which might lead to a change in the experimental setup. The developed mathematical model can be further refined by for instance considering the radioactive decay of the tracer molecules. Different combinations of the radioisotopes which are intended to be used need to be tested in advance to avoid intricacies during the data evaluation.

However, in principle almost every molecule of interest can be tagged by radioactive tracers facilitating a systematic analysis of the carbon nanomembrane's selectivity in aqueous solution. The prospective data will help to gain a better understanding of the involved transport mechanisms and could be the basis of sophisticated modeling attempts.

7. Carbon Nanomembranes from Alkanethiol Monolayers

The previous chapters dealt with the functionalization and characterization of conventional, aromatic-based carbon nanomembranes. The focus of the following five-parted chapter is related to the question whether it is possible to fabricate stable CNMs from structurally different precursor molecules and if so, to investigate the corresponding membrane's properties. Preceding studies are introductorily reviewed in the current state of the research and the motivation of the investigations performed in the present thesis is given. The obtained findings are subsequently shown and compared to the preliminary works. At the end of the chapter a summary with an outlook for future studies is provided.

7.1. Current State of Research

The investigation of Gölzhäuser *et al.* [46] reporting that aromatic monolayers serve as a negative resist in electron beam lithography, whereas aliphatic systems lead to a positive resist, marks one of the starting points of the discovery of carbon nanomembranes. Studies [47, 171] which address the irradiation damage of the utilized monolayers and indicate that for aliphatic systems the destructive processes, e.g. decomposition and desorption, prevail over the cross-linking into a quasipolymeric film, were conducted. In contrast, self-assembled monolayers of aromatic precursor molecules survive the electron irradiation. Based on these observations the aromatic systems were the logical choice for the fabrication of detachable molecularly films. Carbon nanomembranes are for that reason conventionally fabricated from aromatic precursor molecules. Angelova *et al.* [7] intensively explored the effect of the aromatic compound's bulkiness on the properties of the resulting free-standing carbon nanomembrane. It was found that the longer or bulkier the precursor molecule, the thicker or more porous the respective CNM is. The presence of pores was attributed to a less ordered and densely packed SAM. Recently, Neumann *et al.* [44] demonstrated the fabrication of a chemically inert all-carbonaceous carbon nanomembrane by employing hybrid aliphatic-aromatic precursor molecules with carboxylic anchoring groups. In 2012, Waske *et al.* [45] studied the effect of electron irradiation on monomolecular films of the cycloaliphatic molecule 4-cyclohexylcyclohexanethiol (CCHT). Reference measurements were conducted with the SAMs made of the well-known aromatic precursor biphenyl-4-thiol (BPT) and the linear, aliphatic compound 1-dodecanethiol (DDT).

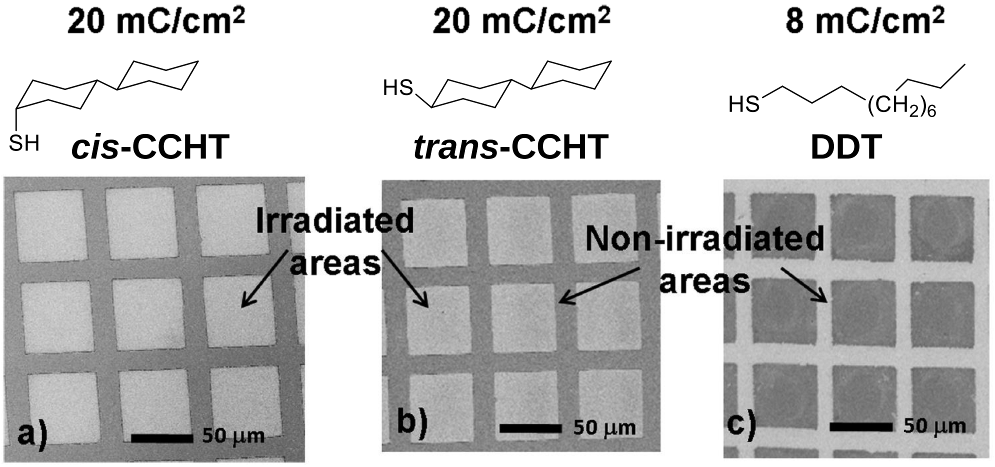

Figure 7.1.: SEM imaged of patterned and etched 4-cyclohexylcyclohexanethiol (CCHT) and 1-dodecanethiol (DDT) samples. Reprinted and adapted with permission from Waske *et al.* [45]. Copyright 2012 American Chemical Society.

The choice of these molecules was justified on the one hand due to the same number of carbon atoms and on the other hand with the fact that CCHT is the cycloaliphatic equivalent of BPT. In figure 7.1 SEM images of patterned CCHT (a/b) and DDT (c) samples on Au(111) after the wet-chemical Au-etching procedure are shown. It can be clearly seen that the irradiated areas were protected by the CCHT leaving a gold pattern, whereas in the case of DDT the inverse behavior was observed. The cycloaliphatic molecules behave as a negative resist like their aromatic counterpart BPT. As it was expected, the DDT acts as a positive resist at even lower doses. Additional measurements have been performed and it was concluded that the cyclic structure is the stabilizing key property. However, the proof that cycloaliphatic molecules form a self-supporting, free-standing carbon nanomembrane by showing a transferred specimen has not been provided.

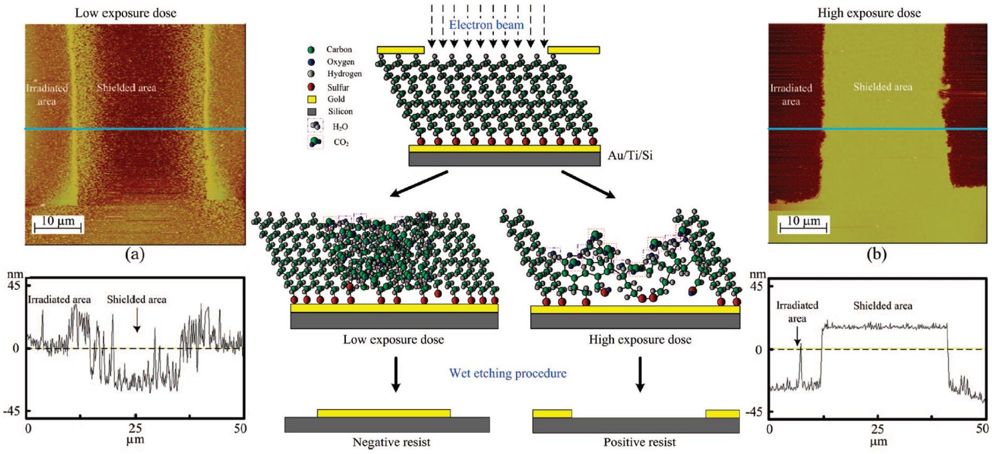

Figure 7.2.: Schematic depiction of the 1-octadecanethiol's (ODT) electron resist behavior with corresponding AFM images as well as depth profiles. Reprinted and adapted with permission from Wu *et al.* [48]. Copyright 2009 American Chemical Society.

Coming back to the self-assembled monolayers made of alkanethiols, Wu *et al.* [48] further examined the effect of electron irradiation on these systems and added interesting findings to the overall picture: A SAM of 1-octadecanethiol

(ODT) on Au(111) has an irradiation dose-depending transition from a negative to a positive electron resist. In figure 7.2 a scheme of the resist behavior and the corresponding AFM images including depth profiles are given. It was found that a dose of around $D \sim (8-10)\,\mathrm{mC\,cm^{-2}}$ with an energy of $E = 50\,\mathrm{eV}$ is sufficient to cause the transition. At lower doses the SAM forms a dense network better protecting the underlying gold substrate during the wet etching procedure than the pristine molecular film. Consequently, the AFM image shows that the etching occurred preferably in the shielded areas. Further irradiation above the transition dose leads to decomposition of the ODT and a partial desorption. A disordered and loosely cross-linked network, which cannot prevent the etching solution from reaching the substrate, results. The edge between the elevated, shielded and SAM-protected area and the irradiated and etched region can be clearly seen in the AFM image. An attempt to detach the irradiated SAMs to examine the formation of a carbon nanomembrane has not been made.

Hamoudi *et al.* [146] demonstrated that the longer the alkyl chain of the precursor molecule, the more prevails the species' decomposition upon irradiation over the desorption. Compounds with shorter alkyl chains mainly leave the system as the entire molecule, whereas species with longer alkyl chains decompose to a certain extend, forming new intermolecular bonds with captured fragments (branching). An idea about the mechanism of the electron-induced structural changes was proposed by Zhou *et al.* [49]. The cross-linking of adjacent carbon chains and the appearance of unsaturated carbon-carbon bonds would be caused by a combination of the release of atomic hydrogen and the uptake of electrons. The effect of the electron's primary energy and the dose on the self-assembled monolayer was studied by Schmidt *et al.* [50] in 2019 using SAMs of the aliphatic DDT as a test system. It was determined that the thickness of the remaining material asymptotically decreases with increasing dose, reaching a saturation value. The saturation value itself increases exponentially with higher primary energies revealing a constant value at energies above $E = 100\,\text{eV}$. The reported behaviors were explained by the balance between destructive processes and cross-linking. Most important is the drawn conclusion that the higher the irradiation dose, the more cross-linked the carbon network becomes, allowing no mass transport or desorption of fragments anymore. The transformation of the pristine SAM was best described by the authors themselves, proposing "*a 'sealed', extensively cross-linked, chemically inhomogeneous hydrocarbon film*" (reprinted with permission from Schmidt *et al.* [50]. Copyright 2019 American Chemical Society.), which is basically a generalized definition of a carbon nanomembrane. Unfortunately, the publication lacks the ultimate proof by fabricating a free-standing specimen due to the purely spectroscopic investigation.

However, although there are indications for the formation of CNMs by using cycloaliphatic or aliphatic precursor molecules, no evidencing reports have been published so far. Because of the preliminary studies on cycloaliphatic systems the fabrication of a free-standing CNM is not hard to imagine, but the available literature is inconclusive concerning aliphatic systems. Thus, it is still unclear whether it is possible to fabricate carbon nanomembranes from such SAMs. The motivation of the following investigations is to provide an answer to the arisen question utilizing alkanethiol monolayers. A successful realization would extend the range of the commercially available molecular building blocks, allowing to screen for custom-made carbon nanomembranes which exhibit the desired properties of interest.

7.2. Fundamental Feasibility Check

In order to find out whether the fabrication of carbon nanomembranes from alkanethiol monolayers is possible or not, self-assembled monolayers on Au(111) made from alkanethiols of different lengths were prepared. The general chemical structure of a linear alkanethiol is $\text{HS-(CH}_2\text{)}_{\text{n-1}}\text{-CH}_3$ with n representing the total number of the alkyl chain's carbon atoms. In this study the compounds 1-dodecanethiol (DDT), 1-tetradecanethiol (TDT), 1-hexadecanethiol (HDT), 1-octadecanethiol (ODT) and 1-docosanethiol (DST) were used as precursor molecules having an overall number of carbon atoms $n = 12$, 14, 16, 18 and 22, respectively. The production of the utilized samples is given in detail in appendix B. The prepared SAMs have been analyzed by XPS and were subsequently irradiated with low energy electrons in the same system under ultra-high vacuum conditions to study its effect on the self-assembled monolayer. The irradiation should lead to a rearrangement of the carbon network similar to carbon nanomembranes. For that reason the data were labeled as CNM. To ensure the comparability to the aromatic systems the standard dose of $D = 50\,\mathrm{mC\,cm^{-2}}$ was chosen, using an energy of $E = 50\,\mathrm{eV}$. The specimen was afterwards again analyzed by XPS. Typical XP spectra of the alkanethiol monolayers before and after the electron irradiation are shown in figure 7.3a using the example of ODT.

For the SAM a narrow C1s peak at $\sim$ 284.9 eV can be observed, which is characteristic for the sp^3-hybridized carbon alkyl chain. The spectrum of the sulfur region nicely shows a doublet originating at $\sim$ 162.1 eV with an energy separation of $\Delta E = 1.2$ eV. The doublet validates the presence of sulfur gold bonds. Furthermore, a small amount of oxygen is detectable, which can be attributed to oxygen-containing adsorbates like water or carbon dioxide on the SAM due to the wet chemical assembly process and to the exposure to ambient air. After the irradiation procedure the oxygen as well as the sulfur peak decrease. Interestingly, the scan of the S2p region reveals a slight shift to higher binding energies but no significant broadening as for the aromatic systems. An explanation for this could be the direct desorption of the molecules and the branching yielding thioether moieties. The adsorbates in the O1s spectrum were released from the surface due to the fragmentation of the precursor molecule. The carbon loss can be clearly seen in the detailed C1s scan. The peak itself broadens and is shifted to lower binding energies at $\sim$ 284.3 eV, indicating a change of the carbon network with a higher amount of sp^2-hybridized carbon. The particular values for the different SAMs are displayed in figure 7.3b. Independent from the length of the alkyl chain the former pure sp^3-hybridized monolayers having all a mixture of sp^3- and sp^2-hybridized carbon after the irradiation. The deconvolution of the C1s peak into the differently hybridized species reveal that the sp^2-hybridized carbon's ratio prevails with increasing length of the precursor molecule. The amount rises from $\sim 65\,\%$ for the DDT (C12) over $\sim 75\,\%$ for the TDT (C14) and seemingly saturates for even longer alkyl chains ($C > 16$) at a value of around $\sim 83\,\%$.

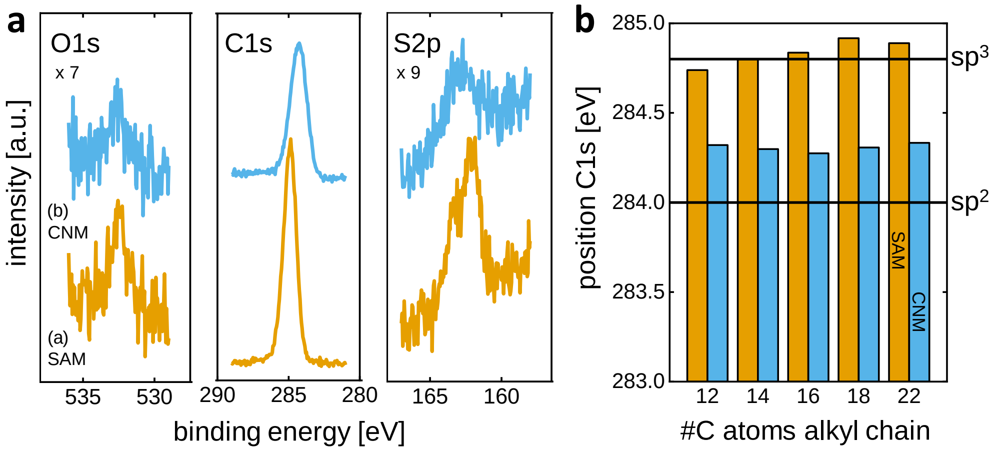

Figure 7.3.: (a) Typical XP spectra in the regions of oxygen, carbon and sulfur of a SAM made of an alkanethiol monolayer and the resulting CNM after the irradiation with low energy electrons under ultra-high vacuum conditions. The data shown exemplary correspond to a 1-octadecanethiol (ODT) SAM and CNM. (b) C1s peak positions of an alkanthiol SAM following the general formula HS-$(CH_2)_{n-1}$-CH_3 and of the respective CNM extracted from the XP spectra. The benchmarks of the hybridization are taken from the literature [149].

The thicknesses of the self-assembled monolayers were determined by the attenuation of the gold signal. During the performed investigations the intensity of the X-ray source changed over time, which is shown in figure 7.4a. Over a time period of around $\Delta t = 10\,\mathrm{h}$ the intensity increased by $12\,\%$, which would cause an error of up to ~ 35 % in the calculated thickness if only one gold reference would have been measured at the beginning or at the end of the experiments. For that reason it was important to measure the gold reference multiple times close to the respective specimen. In figure 7.4b the determined thicknesses are displayed. As known from the literature the thickness of the SAM roughly depends on the length of the used precursor molecule. The program Chem3D Professional 16.0.1.4 [159] was used to estimate the size of each alkanethiol from the sulfur atom to the last carbon atom. A linear dependence between the number of carbon atoms in the alkyl chain of the precursor molecule and the thickness can be seen. The thicknesses of the SAMs derived from the experimental data are shown in orange following the same linear trend as expected.

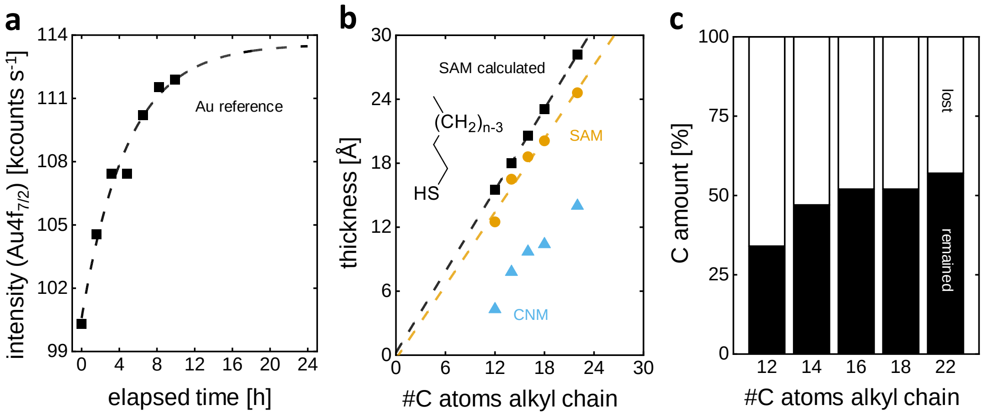

Figure 7.4.: (a) Time-dependent Au4f$_{7/2}$ intensity of a clean gold reference with a curve shape according to $y = A_1 \exp(x/t_1) + y_0$. (b) Determined thicknesses of the SAMs (orange) made from alkanethiol monolayers of different lengths. The general chemical structure is shown with n as the total number of carbon atoms of the alkyl chain. The thicknesses of the SAMs (black) were estimated using Chem3D Professional 16.0.1.4 [159]. Linear relations between n and the SAM's thicknesses are displayed. The values of the specimens after the electron irradiation under ultra-high vacuum conditions are shown in blue. (c) Relative amount of carbon which remained on the surface after the irradiation as a function of the length of the alkyl chain.

The values are always smaller compared to the estimated sizes with a deviation of around 13 %, but still agree well with the predictions. An explanation for this is the tilting of the alkanethiols on the gold surface when the self-assembled monolayer is formed, which was not taken into account for the computer prediction. After the electron irradiation the determined thicknesses (blue) significantly decrease due to the irradiation damage. Consequently, the attenuation of the gold signal is in all cases less than before. This can be attributed to the fragmentation and material loss from the surface. Additionally, the formation of a loosely cross-linked carbon network could occur. Due to the change in the IMFP, which is assumed to remain constant for the SAM and CNM, the determination suffers from some inaccuracies. Nevertheless, it can be stated that the longer the alkyl chain, the less is the reduction of the thickness. Thicknesses of around one nanometer are reported for stable carbon nanomembranes. Only for the shortest alkanethiol DDT (C12) the thickness is far below this reference value having a value of only $d \sim 0.4\,\text{nm}$. On that basis it was expected that a detachable and stable monomolecularly film can be fabricated using precursor molecules with at least fourteen carbon atoms in the alkyl chain. The precise values of the remaining carbon amount are shown in figure 7.4c. DDT lost two-third of its carbon, whereas the loss decreases down to two-fifth for DST (C22). This observation indicates that longer alkyl chains with more carbon material prevent fragments from the desorption of the surface by capturing them into the carbon matrix. The same behavior was reported by Hamoudi *et al.* [146] who compared self-assembled monolayers made of C6 and C12 alkanethiol precursor molecules.

The spectroscopic analysis strongly suggests a rearrangement of the SAM's carbon network. An ultimate proof whether the change in hybridization resulted in the formation of a stable carbon nanomembrane or simply indicated the destructive fragmentation of the monolayer is provided by transferring the irradiated sample onto a TEM grid in order to fabricate a free-standing specimen. In figure 7.5a the irradiation procedure of a mounted sample is schematically shown. The periphery of the specimen is shielded due to the design of the XPS sample holder so that no electrons will reach the underlying SAM. The electron gun of the system was calibrated in advance for each of the alkanethiol monolayers ensuring the precise knowledge of the applied dose. An average dose of $D = 50\,\mathrm{mC\,cm^{-2}}$ was utilized for the complete sample resulting in several local doses as displayed in a typical dose map in figure 7.5b. It can be seen that some areas exhibit twice the average dose (top left), whereas others have values which are below the intended one (top and bottom right).

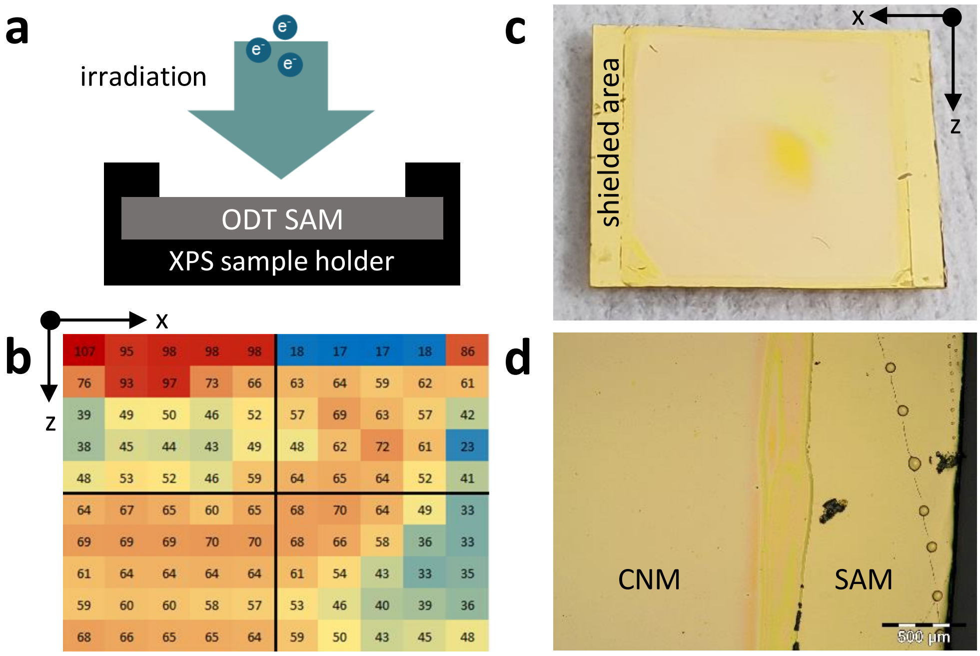

107	95	98	98	98	18	17	17	18	86
76	93	97	73	66	63	64	59	62	61
39	49	50	46	52	57	69	63	57	42
38	45	44	43	49	48	62	72	61	23
48	53	52	46	59	64	65	64	52	41
64	67	65	60	65	68	70	64	49	33
69	69	69	70	70	68	66	58	36	33
61	64	64	64	64	61	54	43	33	35
59	60	60	58	57	53	46	40	39	36
68	66	65	65	64	59	50	43	45	48

Figure 7.5.: (a) Schematic depiction (side view) of the electron irradiation in the XPS system. (b) Calibrated dose map with doses in $\mathrm{mC\,cm^{-2}}$ used for the electron irradiation of an ODT specimen in the XPS system under ultra-high vacuum conditions utilizing an average dose of $D = 50\,\mathrm{mC\,cm^{-2}}$. Areas with local doses lower than the average dose (yellow) appear more bluish, whereas the ones with a higher one are more reddish. (c) Photography of the irradiated ODT specimen after the coating with PMMA. (d) Optical microscopy image of the sample's periphery.

The irradiated specimen needs to be stabilized by PMMA for the transfer procedure. It was found that the polymer exclusively adheres on the irradiated regions, where the light pink shimmer corresponds to the PMMA. Using ODT as a typical example, a photography and an optical microscopy image of the spin-coated sample are given in figure 7.5c and d, respectively. The shielded areas and thus the SAM are too hydrophobic, preventing the adhesion of the solvated polymer. This hypothesis is strengthened by the appearance of spherical droplets indicating its spin-off directly after the formation on the hydrophobic surface. For ODT monolayers it is known that they become more hydrophilic [48] when they are irradiated with electrons. The spin-coating of PMMA should be benefited in these areas. The dose map of (b) corresponds well with the coated regions, validating the mentioned hypothesis. It can be nicely seen that the areas with local doses below the average dose (c, bottom left corner) repel the polymer, whereas the irradiated regions are covered by the PMMA. Consequently, an inspection by eye after the spin-coating process facilitates the verification of the change in the carbon network revealing SAM and CNM areas.

The spin-coated samples were transferred onto quantifoil multi A holey carbon film grids to fabricate free-standing carbon nanomembranes. The imaging was done by using an helium ion microscope in the dark field transmission mode. In figure 7.6 a low magnification image of each alkanethiol is provided. It is obvious that a transferable carbon membrane can be formed starting with a overall number of fourteen carbon atoms in the alkyl chain. For the shortest alkanethiol DDT (C12) only isolated residues of a former hydrocarbon film can be seen as the high magnification image in (b) shows. The carbon nanomembrane from TDT (C14) seems to be very fragile and thus ruptures very easily. The resulting CNM is characterized by large defects all over the free-standing areas. From HDT (C16) on no defects can be recognized at this magnification.

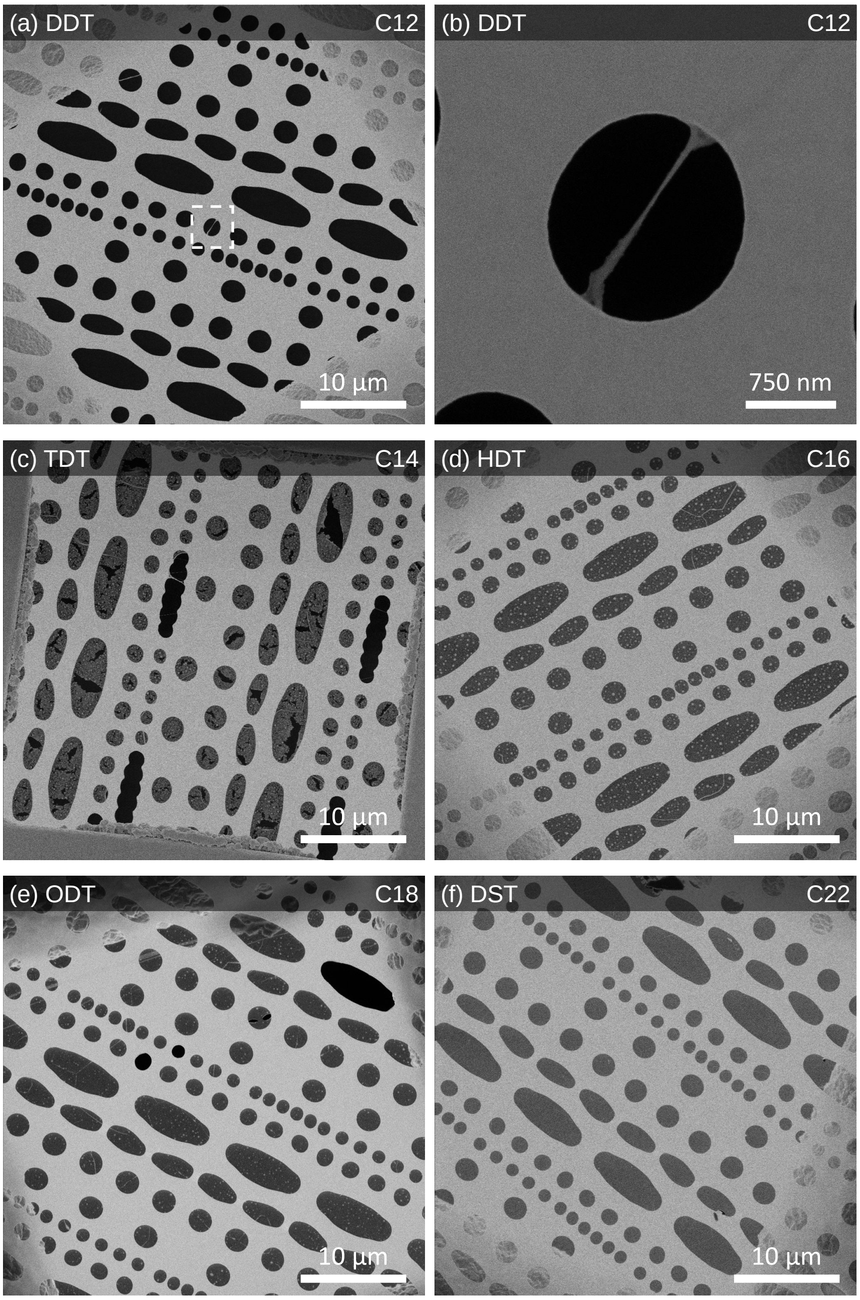

Figure 7.6.: Low magnification HIM images (dark field transmission mode) of different alkanthiol monolayers which were irradiated under ultra-high vacuum conditions. The samples were transferred onto quantifoil multi A holey carbon films. Only for DDT a high magnification image is provided.

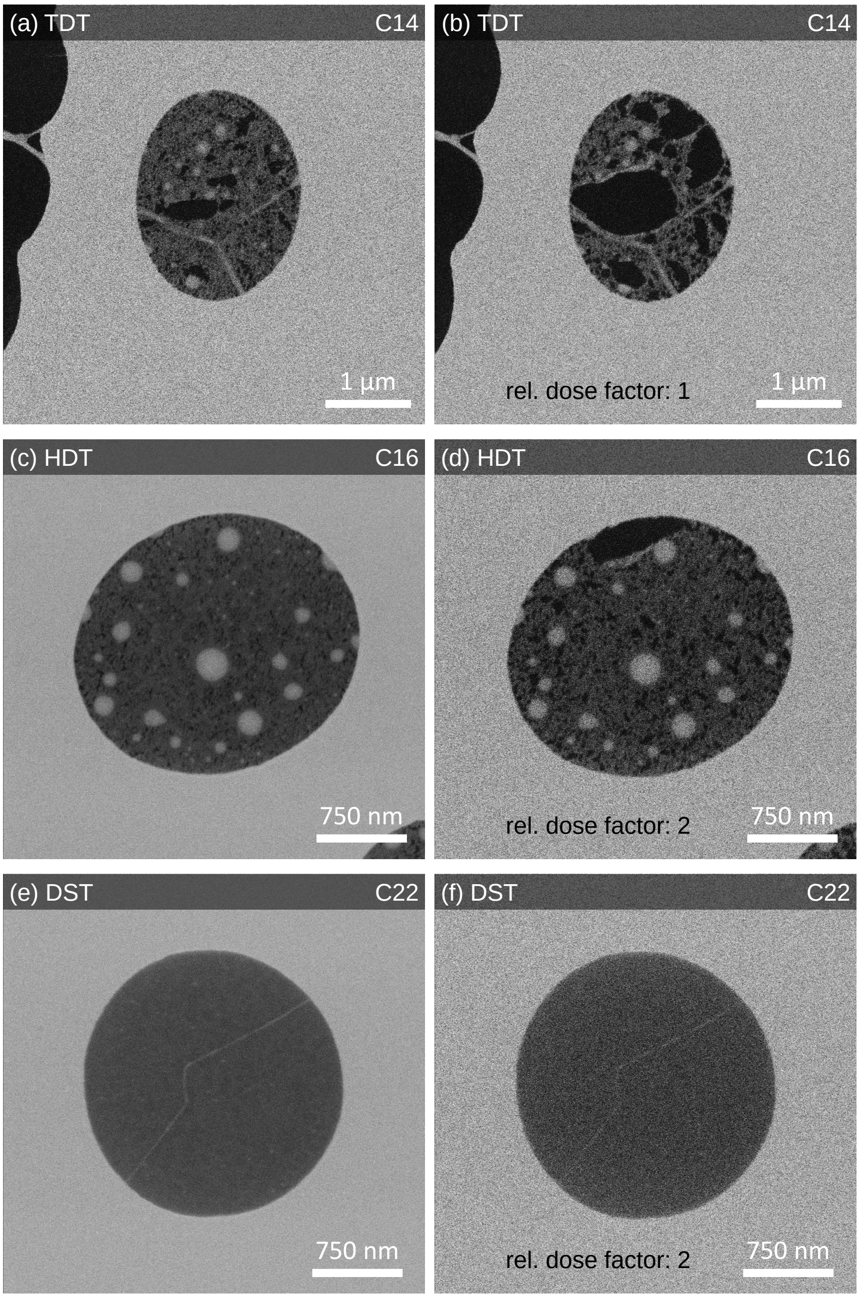

Figure 7.7.: Series of high magnification HIM images (dark field transmission mode) of the transferred CNMs from different alkanethiol monolayers as in figure 7.6. The left column displays the first image of each series and the right column the last one with the corresponding dose normalized to the dose of TDT.

In figure 7.7 the corresponding high magnification images of the same samples are displayed. The same region of a CNM was subsequently imaged multiple times to study the stability of the membrane. The deposited doses were normalized to the applied dose of TDT and written into the respective image. The left column shows the first image and the right column the last image of the series. Smaller defects can be seen on the first HDT-image at this magnification. For ODT, which is not shown due to space restrictions, and DST such openings cannot be observed. Interestingly, the bright areas, which are assumed to be regions of higher carbon density, do not appear for the DST (C22). The reason for the appearance could not be clarified in the present thesis. The applied dose causes the TDT membrane to collapse, whereas the HDT CNM suffers noticeably less even at twice the dose. ODT and DST withstand the imaging process without any visible ruptures. The taken HIM images clearly prove the fabrication of self-supporting carbon nanomembranes from alkanethiol monolayers. It is noticeable that the destructive processes of fragmentation and desorption prevail over the cross-linking in the case of DDT so that no stable CNM can be transferred. The increase of the number of carbon atoms in the alkyl chain shifts the balance between the two competing processes towards the constructive one, leading to an enhanced mechanical stability of the carbon nanomembrane.

For the investigation of the membrane's properties more samples needed to be prepared. In terms of the CNMs' fabrication the irradiation of the self-assembled monolayers in the XPS system is not suitable. The electron irradiation is typically performed in another system which is equipped with a FG 15/40 electron gun. The base pressure of this system is roughly three orders of magnitude higher compared to the XPS system, allowing the deposition of carbon contaminations from the surroundings on the sample. To exclude the formation of a transferable membrane solely from the carbon species inside of the instrument control experiments have been performed. The same procedure for the preparation and the transfer has been applied but no precursor molecules were added to the absolute ethanol. The results are shown in figure 7.8. Some small particles were visible after the cleaning of the gold substrate as displayed in panel (a). However, such minor contaminations are not present every time, indicating that the particles originate most likely from the used glass ware and not from the used absolute ethanol.

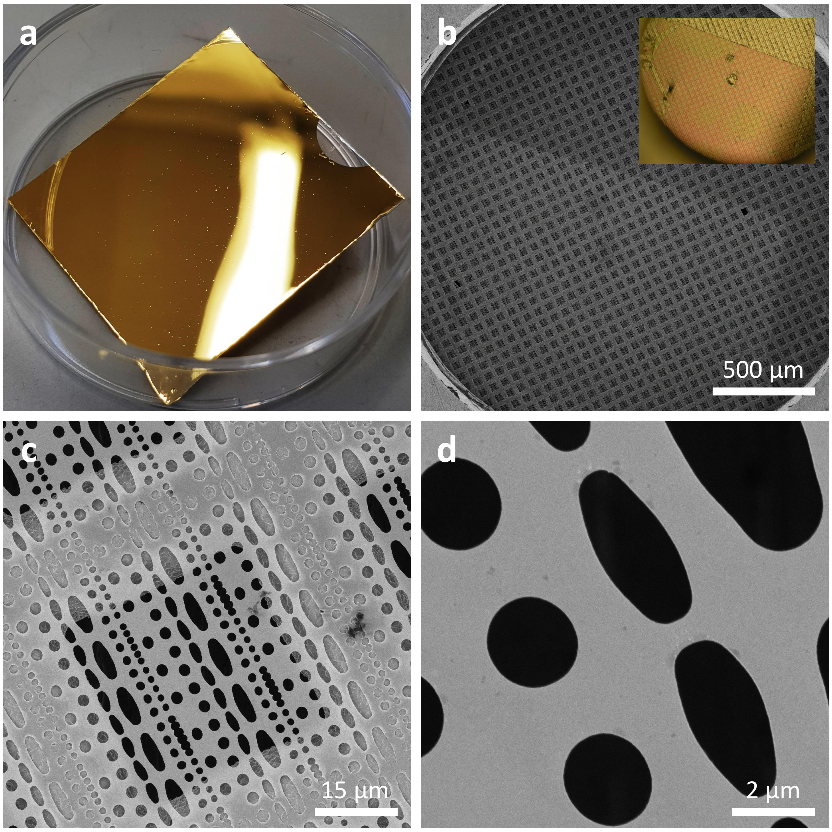

Figure 7.8.: (a) Photography of the cleaned gold substrate before the preparation procedure. (b), (c), (d) HIM images (SE mode) of the transferred specimen of the control experiment without precursor molecules. The inset in (b) shows an optical microscopy image of the transferred and PMMA-stabilized sample.

In figure 7.8b a low magnification HIM image of the transferred specimen is shown. The inset provides an optical microscopy image of the same sample before the dissolution of the PMMA coating, which exactly matches the position and orientation of the bright area in the HIM image. One might assume that a carbon nanomembrane is present in that region, but taking a closer look to the panels (c) and (d) reveals only the uncovered support structure. The contaminations from panel (a) can be identified as dark spots on the quantifoil in panel (d). Consequently, it is not possible to form a CNM by contaminations from the glass ware, the used solvents or the carbon residues inside the electron irradiation chamber.

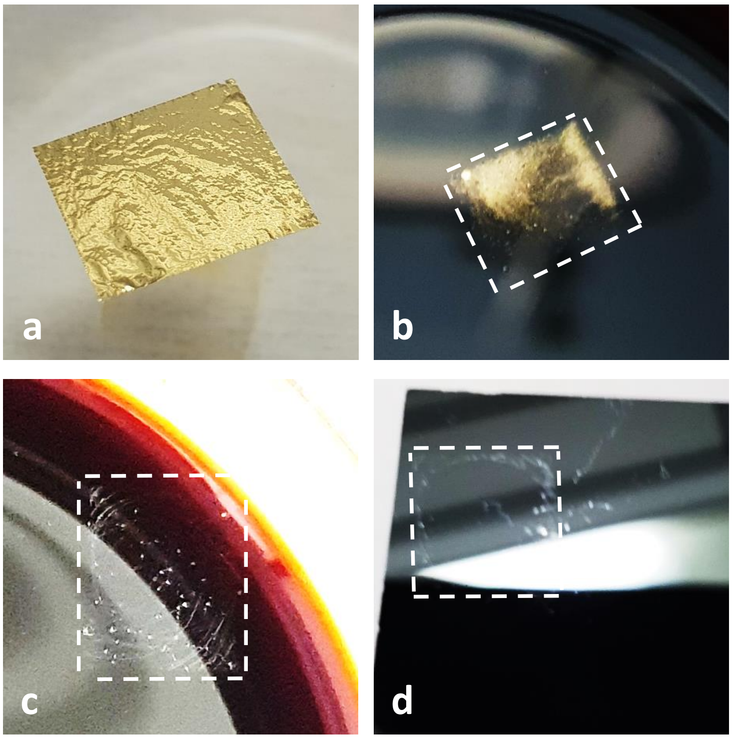

Figure 7.9.: Transfer of a PMMA spin-coated ODT SAM. (a) Detached specimen floating on Millipore water. (b)/(c) Etching of the underlying gold substrate. (d) Residues on a silicon wafer piece.

It was further investigated whether the self-assembled monolayer itself is stable enough to be transferred onto another support. An ODT SAM was spin-coated with PMMA and subsequently transferred. Photographs of the procedure are given in figure 7.9. The SAM on the gold substrate was detached from the mica support (a) and placed onto the surface of an etching solution (b, c) to dissolve the underlying noble metal. In panel (c) it can be seen that a very thin film is floating on the etching solution. Based on the aforementioned experiments, it is assumed that only an insignificant amount of PMMA covered the thin film. On the attempt to transfer this floating film onto a silicon wafer the fragile layer dissipates. Only residues could be captured with the transfer wafer (d), which could not be released from its surface anymore. Even if the SAM has been detached from the gold substrate and if it was kept together by the negligible PMMA coating, a transfer was not successful. Thus, the results of the performed control experiments validated that the observed carbon nanomembranes could have originated only from the irradiated alkanethiol monolayers.

To finalize this section an ODT SAM was irradiated with the FG 15/40 electron gun system and subsequently analyzed in order to compare its properties with the samples which were fabricated under ultra-high vacuum conditions. The RAIRS measurements are shown in figure 7.10a. Peaks at $\tilde{\nu} \sim 2960$ cm^{-1} and $\tilde{\nu} \sim 2870$ cm^{-1} as well as at $\tilde{\nu} \sim 2920$ cm^{-1} and $\tilde{\nu} \sim 2850$ cm^{-1}, which are typical for the asymmetric and symmetric stretching vibrations of the alkyl chain's methyl ($-CH_3$) and methylene ($-CH_2$) groups, can be observed in the spectrum of the self-assembled monolayer. After the treatment with electrons these vibrations were measurably weakened, but did not vanish completely. The data agree with the previous experiments, demonstrating the rearrangement of the alkanethiol SAM into an amorphous carbon network with a mixture of sp^2- and sp^3-hybridized carbon atoms. The XP spectra of the oxygen, carbon and sulfur regions of the ODT CNM are provided in figure 7.10b. The higher amount of oxygen and the asymmetric shape of the C1s peak compared to the data in figure 7.3a are striking. The carbon peak of the sp^3/sp^2-hybridized network with the main contribution at $\sim$ 284.3 eV broadens towards higher binding energies. Together with the higher oxygen content on the sample it is most likely that the energetically higher carbon species are oxidized. Besides that, the presence of oxygen-containing carbonaceous adsorbates cannot be excluded. The sulfur scan is in principle similar to the one in figure 7.3a, but the signal-to-noise ratio is worse due to the increased attenuation of the ejected electrons within the thicker layer. The analysis of the gold signal's attenuation reveals a membrane thickness of $d \sim 1.6\,\mathrm{nm}$. This is around $\Delta d \sim 0.5\,\mathrm{nm}$ thicker than the specimen which was irradiated in the XPS system. However, it needs to be considered that the determined value has some uncertainty due to the adsorbates on top of the sample so that the thickness of the carbon nanomembrane would be overestimated.

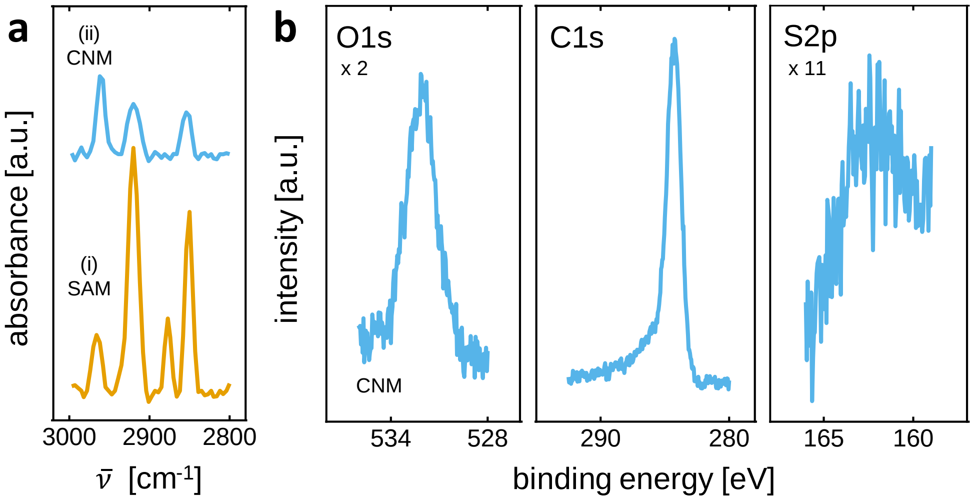

Figure 7.10.: (a) RAIRS measurement of the 1-octadecanethiol SAM (i) and the corresponding CNM (ii) after the electron irradiation treatment within the FG 15/40 electron gun system. (b) Respective XP spectra of the carbon nanomembrane in the regions of oxygen, carbon and sulfur.

A free-standing specimen on a quantifoil multi A holey carbon film grid on a TEM grid was prepared from these type of samples. AFM measurements in contact mode (constant force) were performed. The results are given in figure 7.11a/b. In panel (a) the SensHeight signal and in panel (b) the phase contrast are displayed. The transferred CNM is mechanically stable and withstands the imaging procedure without any damages. Circular spots with a height difference of $\Delta h \sim (10 - 30)\,\mathrm{nm}$ appear throughout the complete sample. Due to the same phase of these areas compared to the rest of the carbon nanomembrane it is assumed that they are composed of a carbonaceous material. The elevated regions occur in the corresponding HIM image as bright regions. Taking a look at the ruptured elliptic orifice in panel (c) shows that the heightened areas fold together with the CNM. However, it can be stated that the formed carbon nanomembrane is comparable to the one in figure 7.6.

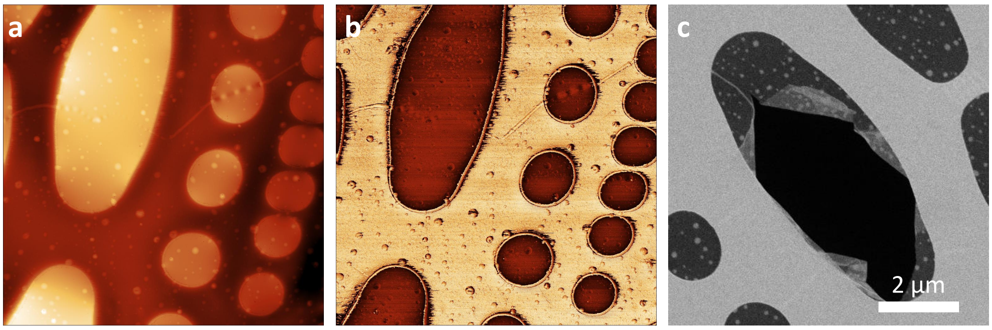

Figure 7.11.: (a)/(b) AFM images of a free-standing ODT CNM on a quantifoil multi A holey carbon film grid on a TEM grid measured in contact mode (constant force). The image sizes are 10x10 µm. (a) SensHeight signal with a total height difference of $\Delta h = 195\,\mathrm{nm}$. (b) Phase contrast signal displayed with an adaptive non linear color mapping. (c) Low magnification HIM image (dark field transmission mode) of the same sample.

The preparation of carbon nanomembranes from alkanethiol monolayers was validated in the course of this section. Spectroscopic evidence have been provided and HIM images of transferred specimens showed self-supporting, free-standing CNMs. Major contributions from contaminations during the fabrication of the carbon nanomembrane have been excluded and it was shown that the electron irradiation at higher pressures does not significantly affect the formation of the resulting CNM.

7.3. Detailed Study of 1-Octadecanethiol (ODT)

To characterize the carbon nanomembranes from alkanethiol monolayers the membranes which originate from the precursor molecule 1-octadecanethiol (ODT, C18) were chosen to be an appropriate model system. The following section will explore the mechanical properties, the topography and the permeation behavior in detail. Among the macroscopic non-defective CNMs the fabrication of ODT specimens from an ethanolic solution is comparably simple, whereas the conditions for the preparation of DST (C22) monolayers has some potential to be optimized. The detailed description of the used samples is provided in appendix B. However, more important is the comparability of the obtained results to previous investigations. Up to now, the carbon nanomembranes made from 1,1',4',1"-terphenyl-4-thiol (TPT) are studied the most and the properties of these CNMs are well-known. Both precursor molecules TPT and ODT have the same number of carbon atoms, which allows the direct comparison of the different chemical structures on the resulting CNM.

The mechanical properties of the ODT samples were explored by employing the bulge test method. Due to an applied pressure a free-standing specimen bulges to a certain extend, which can be monitored by the deflection of the AFM cantilever. The Young's modulus E and the residual stress σ_0 can be derived from the resulting pressure-deflection curve using the Beam's equation (4.1). A typical example is shown in figure 7.12a demonstrating the applicability of the model to describe the experimental data.

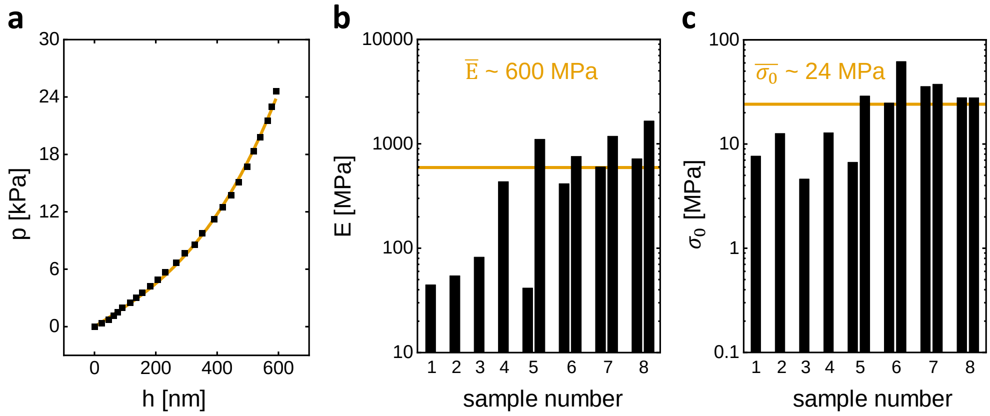

Figure 7.12.: (a) Bulge test: Typical pressure-deflection curve of an ODT sample. The data were fitted according to the Beam's equation (4.1) to extract the Young's modulus E and the residual stress σ_0. (b)/(c) Derived mechanical properties of the measurement series displayed with the respective average value.

In figure 7.12b/c the extracted mechanical properties of the measurements series are provided. It can be seen that the values do not only differ between different samples but also deviate within the same one. The obtained results roughly scatter within one order of magnitude, which is known to be a typic range for carbon nanomembranes. The mean values of the Young's modulus and the residual stress are $\bar{E} = (592 \pm 151)\,\mathrm{MPa}$ and $\bar{\sigma_0} = (24 \pm 5)\,\mathrm{MPa}$, respectively. The standard error of mean was used for the error estimation. The residual stress is in the same range as for other CNMs reported by Zhang *et al.* [23]. Lower values of the residual stress were explained by an interplay of the structural-dependent agility during the cross-linking process and the existence of pores, which prevails in the case of less densely packed SAMs. ODT forms a densely packed monolayer and has an aliphatic hydrocarbon chain ensuring a high degree of freedom. Nevertheless, its residual stress is about eight times higher compared to the value of TPT, which consists of more rigid aromatic rings. As a consequence, the pores' geometry and distribution need to be different. HIM images of an ODT specimen after the bulge test are given in figure 7.13a/b proving the presence of an intact carbon nanomembrane over the orifice. Even at higher magnifications no nanopores could be observed.

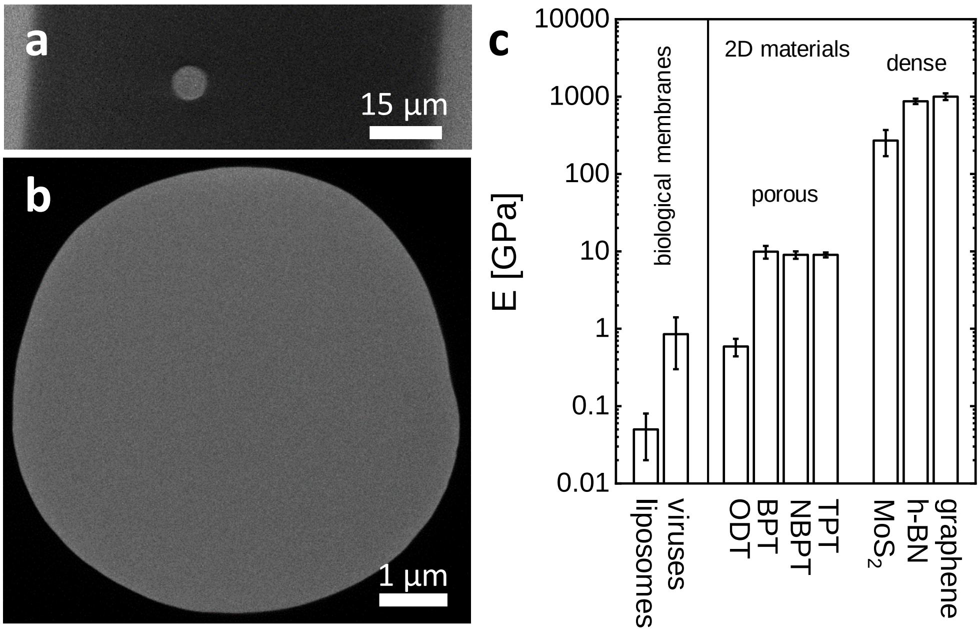

Figure 7.13.: (a)/(b) HIM images (SE mode) of an ODT sample after the bulge test. (c) Comparison of the obtained Young's modulus E with ranges of Young's moduli of liposomes [172, 173], viruses [174–180], carbon nanomembranes [23, 70] and dense 2D materials [181–183].

The Young's modulus is compared to other materials in figure 7.13c. The porous carbon nanomembranes from oligophenylthiols have Young's moduli of $E \sim 10\,\mathrm{GPa}$, which is around two orders of magnitude lower than the ones of dense and rigid 2D materials like graphene. Biological membranes are comparably soft and the Young's moduli of liposomes or viruses are in the megapascal range. The ODT CNM counts to the class of porous 2D materials but shows a Young's modulus which is about seventeen times lower than other carbon nanomembranes. Thus, it is rather situated in the same range as biological membranes. An explanation for this finding would be that the alkyl chains have on the one hand enough rotational freedom to cross-link with other precursor's chains but on the other hand cannot form a network as dense as the aromatic systems due to the enhanced carbon loss. The resulting carbon nanomembrane would exhibit a spiderweb-like structure where the self-supporting membrane is comparably soft but still mechanically stable.

In the next step, the permeation of water through the ODT CNM was investigated. Gravimetric analyses using the improved cup design were employed to derive the water permeance. In this way the accessible area could be determined before and after the measurements and ensure the cleanliness and intactness of the specimens. To guarantee the reliability of the obtained data the developed design was trialed in advance by using a closed silicon nitride window without any openings. In figure 7.14a the mounting of a sample is shown. It turned out that it is important to carefully tighten the socket head screws one after the other in consecutive order to avoid the breaking of the silicon chip. Teflon and copper gaskets were utilized to seal the containers, which were filled with Millipore water. The leakage test was performed in a Memmert UF 110$^{\mathrm{PLUS}}$ oven at a temperature of $T = (30.4 \pm 0.4)\,^{\circ}\mathrm{C}$ and under a low relative humidity environment of $\mathrm{RH} = (20 \pm 2)\ \%$ inside of the oven. After a certain time period the cups have been allowed to reach room temperature and were weighed four times. Additionally solid reference weights were weighed to estimate the accuracy of the determined masses, because these should neither loose nor gain weight. The evaluation of the reference data allows to determine how accurately the masses can be reproduced. The daily average value of each cup was calculated and all daily average values were averaged again to determine the overall average value. The deviation of the daily average masses to the overall average is exemplarily shown for the Teflon gaskets in figure 7.14b with the respective standard deviations. The last data point was taken after one day under ambient conditions to exclude temperature effects on the obtained values due to insufficient cooling times.

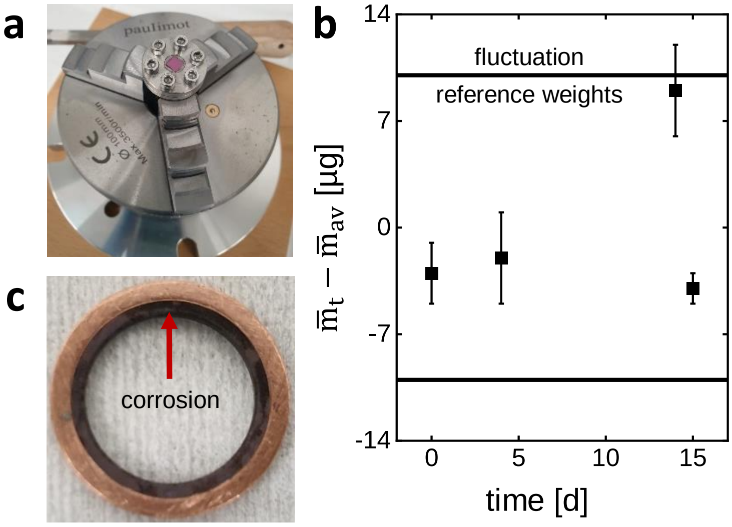

Figure 7.14.: (a) Sample for the gravimetric analysis mounted on the improved cup design by the aid of a three-jaw chuck. (b) Leakage test with a Teflon-sealed and closed specimen filled with Millipore water. The difference to the overall average with the respective standard deviation is shown. The black lines indicate the fluctuations' range of solid reference weights. (c) Copper gasket after the leakage test with Millipore water. The red arrow points towards the corroded darker regions.

The black lines limit the range of the deviations of the solid reference weights determining the accuracy of the balance to be $\Delta m = \pm 10\,\mu\mathrm{g}$ under the used conditions. It is obvious to see that the acquired sample masses lie within the balance's accuracy window. Consequently, no mass loss occurred over a time period of two weeks, proving the tightness of the developed design for Millipore water. The values for the copper gasket are similar. However, in the case of Millipore water the copper ring corroded as it is displayed in figure 7.14c. It is clearly visible where the sealing separated the outside from the inside of the container. Although Teflon turned out to be the material of choice, the new cup design can in principle be used with copper gaskets. This might be advantageous for other liquids which may be incompatible with Teflon. In any case, an additional leakage test needs to be performed to validate the applicability of the design for the compound under investigation.

The gravimetric analysis of the specimen covered by an ODT CNM was performed in the same manner. The containers were stored for seven days under the controlled environment. Each cup was measured three times. The water permeance P was calculated using equation (4.3). The precise values of the sample area were obtained from HIM images taken in the transmission mode. In figure 7.15a an image of an ODT carbon nanomembrane after the cup test is provided. Besides the typical pattern of the ODT CNM, some darker areas, for instance around the rim, can be seen. Most likely carbon contaminations from the ambient air are responsible for these regions. Nevertheless, the HIM image reveals an intact carbon nanomembrane covering the orifice of the silicon nitride window. The derived water permeances are displayed in figure 7.15b. The CNM-covered samples could be divided into intact and defective specimens. The latter ones show permeances in the same range as the non-covered reference cups. The samples considered as intact have water permeances which are on average seven times lower compared to the defective and reference samples. The overall yield of intact specimens was 69 % resulting in an average permeance of $\bar{P}\,(\mathrm{H_2O}) = (4.30 \pm 1.07) \cdot 10^{-4}\,\mathrm{mol\,m^{-2}\,s^{-1}\,Pa^{-1}}$. The standard deviation was used for the error estimation. Compared to the outstanding water permeance of TPT CNMs [8] the carbon nanomembranes made from ODT monolayers show a permeance which is even higher by a factor of four. The finding indicates the existence of a highly porous membrane, which was already suggested by the bulge tests. A high permeance is in most cases accompanied by a lack of selectivity. Thinking about the membrane's potential application for separation processes, the ability to reject certain compounds needed to be characterized. In order to determine the selectivity of one and the same membrane, gas permeation measurements of free-standing ODT CNMs were conducted.

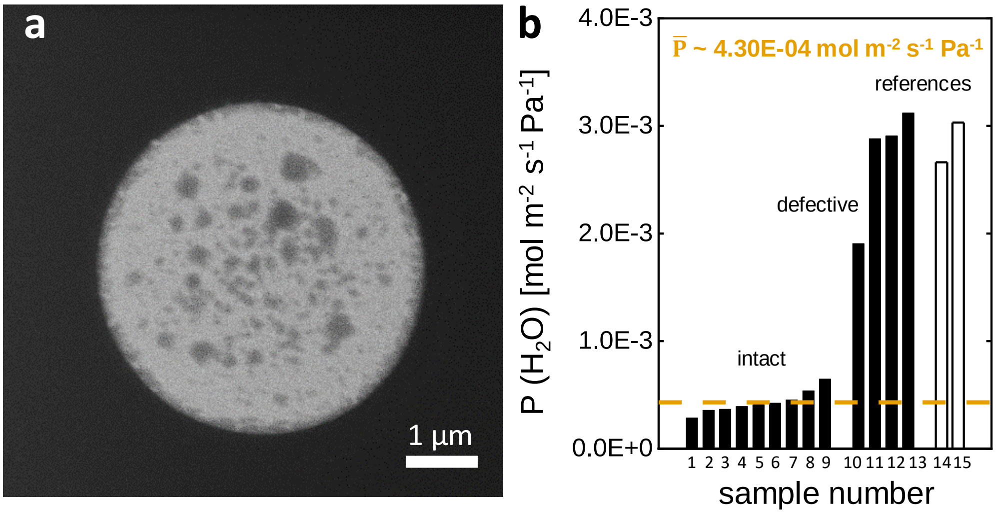

Figure 7.15.: (a) HIM image (transmission mode) of an ODT sample after the gravimetric analysis (∼ 7 d). (b) Derived water permeances from the mass loss experiments. The black bars represent specimens covered by an ODT CNM, whereas the white bars correspond to open orifices. The average value of the intact samples is written in the graph and displayed as a horizontal line.

The samples have been glued on a copper disc, which simultaneously acted as a gasket for the vacuum apparatus. A certain amount of gas or vapor was introduced into the feed side. The permeating species were detected by a mass spectrometer. The quality and intactness of the specimen have been checked after the permeation measurements by helium ion microscopy, guaranteeing the reliability of the acquired data. An example of a clearly broken specimen can be seen in figure 7.16a. The ruptured and folded ODT CNM is visible at the rim of the orifice. The fabrication of intact samples could be achieved with a yield of 50 %. Several gases and (organic) vapors of different sizes were tested. Typical results are provided in figure 7.16b/c. The permeances were plotted as a function of the inserve square root of the molar mass in panel (b). The gaseous species follow the prediction of the Knudsen diffusion, whereas the (organic) vapors differ from the ideal curve with heavy water as the most prominent compound. This observation most likely originates from the fact that the vapors are able to condense at the membrane's surface, which allows additional lateral diffusion to the pores, enhancing the permeation through the carbon nanomembrane. In panel (c) the different permeances through the ODT CNM are compared to obtained data from previous studies on TPT CNMs. Four ODT samples were averaged to obtain the average permeance, which is shown with the standard error of mean. TPT represents the prototype of a highly selective carbon nanomembrane, which allows only helium and heavy water to pass through the membrane. All other compounds were rejected.

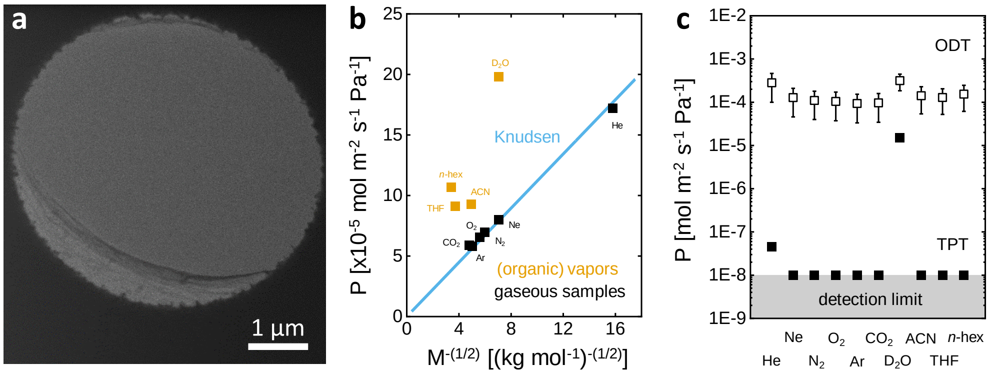

Figure 7.16.: (a) HIM image (transmission mode) of a broken ODT CNM after the gas permeation measurement. (b) Permeances of different gases and (organic) vapors through an ODT CNM as a function of the inverse square root of the molar mass. The Knudsen relation is plotted as a reference line. (c) Permeances of the compounds used in (b) through ODT and TPT CNMs. Four ODT CNMs were averaged and displayed with the standard error of mean. The values for the TPT CNM were taken from the literature [8, 41].

In the case of ODT all species under investigation were able to permeate through the CNM. The gas permeation measurement shows that, in contrast to the TPT CNM, the carbon nanomembrane prepared from 1-octadecanethiol is not selective. The lack of selectivity indicates a broader average size of the carbon nanomembrane's pores, enabling the transport of larger molecules through the CNM. To investigate the membrane's structure AFM images were taken. A pristine ODT SAM was measured, *in-situ* irradiated with electrons and imaged again to monitor the structural changes.

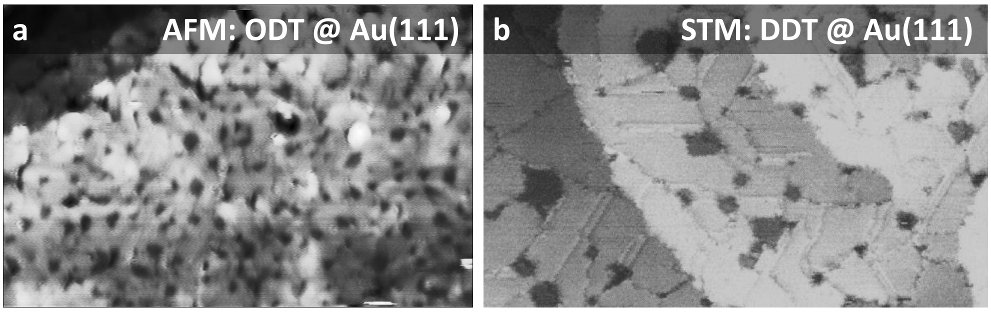

Figure 7.17.: (a) AFM image of an ODT specimen on Au(111) displayed with an adaptive non linear color mapping. The measurements were done at $T = 90\,\text{K}$ in the non-contact mode under ultra-high vacuum conditions. (b) STM image of a 1-dodecanethiol monolayer on Au(111), which was annealed at $T \sim 85°\text{C}$ during 20 min. Panel (b) was reprinted and adapted with permission from Schoenenberger *et al.* [184]. Copyright 1995 American Chemical Society. Both images have a size of 100 x 65 nm.

The self-assembled monolayer was measured at a temperature of $T = 90\,\text{K}$ under ultra-high vacuum conditions. The resulting AFM image is given in figure 7.17a. A typical STM measurement of an annealed alkanethiol SAM on Au(111) using 1-dodecanethiol as an example is shown in panel (b) for comparison. Despite the fact that the obtained AFM image is more blurry, the characteristic surface of a SAM with its different domains and depressions can be observed. The structures are comparable with the STM image, proving the formation of a self-assembled monolayer of ODT on the substrate. In figure 7.18a a higher magnification scan of the SAM is shown. Although measured at low temperatures and under ultra-high vacuum conditions, it was challenging to obtain a clear image because of the high mobility of the alkyl chains. Nevertheless, the ordered arrangement of the precursor molecules can be seen as indicated by the yellow lines. A line scan, which is provided in detail in panel (b), reveals an intermolecular distance of around $d \sim 0.42\,\text{nm}$. It is known that SAMs of alkanethiols on Au(111) have a $\left(\sqrt{3}\,\sqrt{3}\right)\mathrm{R}30\,^\circ$ unit cell [185] for which a schematic depiction is given in figure 7.18c. The edge length of this arrangement has a value of around $d \sim 0.43\,\mathrm{nm}$. The observed distance agrees very well with the theoretical one, validating further the presence of an 1-octadecanethiol monolayer.

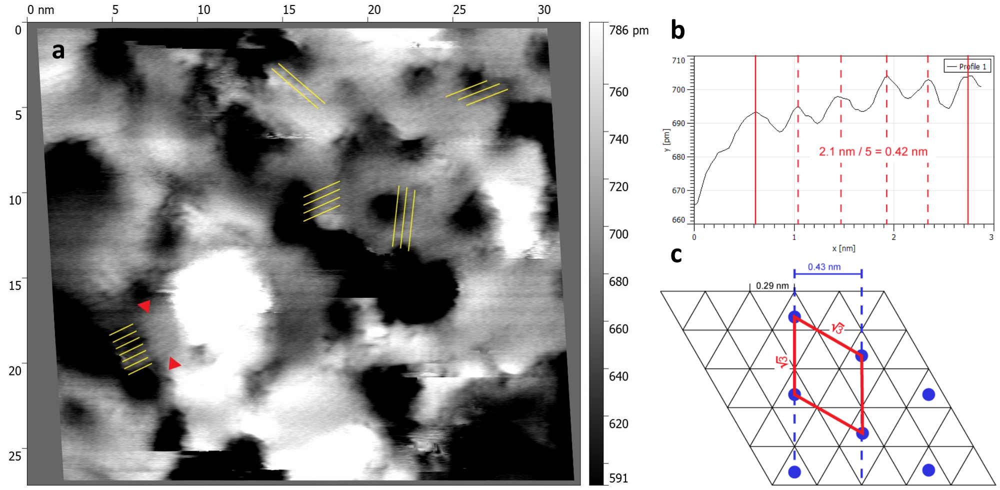

Figure 7.18.: (a) UHV-AFM image (non-contact mode) of an ODT SAM on Au(111) at $T = 90\,\mathrm{K}$. The yellow lines indicate alignment of the ordered molecular structure. The red arrows mark the points of the line profile, which is shown in panel (b). (c) Schematic illustration of a $\left(\sqrt{3}\,\sqrt{3}\right)\mathrm{R}30\,^\circ$ unit cell on Au(111). Reprinted with permission of Niklas Biere, Experimental Biophysics & Applied Nanoscience at Bielefeld University, 2020.

As mentioned in the previous section bright spots can be seen on a transferred specimen imaged with a HIM. The hypothesis that they were caused by residues of PMMA during the transfer procedure could be disproved by the taken AFM images of the pristine ODT SAM, where these features are already present directly after the formation of the self-assembled monolayer. In figure 7.19a a low magnification scan shows the same bright features as they appear in the HIM images of a free-standing sample. An extract of such an image is given in panel (b) for comparison. The AFM image was scaled to the same dimensions and inserted as an inset into the HIM image, revealing that the elevated regions are comparable with the detected bright spots. The height of those features is around $\Delta h \sim 10\,\mathrm{nm}$.

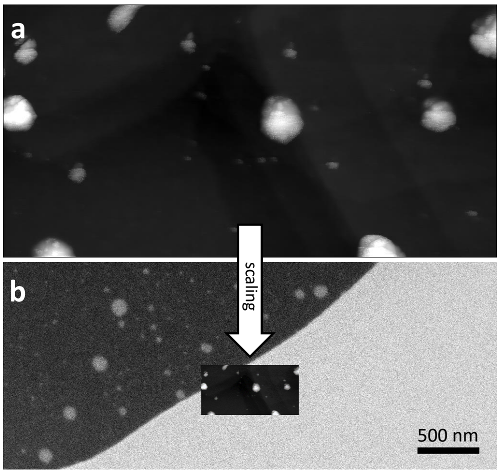

Figure 7.19.: (a) UHV-AFM image (non-contact mode) of an ODT SAM on Au(111) at $T = 90\,\mathrm{K}$. The image size is 800 x 400 nm with a total height difference of $\Delta h \sim 10\,\mathrm{nm}$. (b) HIM image (dark field transmission mode) of a transferred ODT CNM displayed with an inset of the AFM image shown in (a). The inset has been adapted to the same scale as the HIM image.

Hypotheses on the origin of these features are the clustering of precursor molecules or the deposition of carbonaceous contaminations during the preparation procedure from the utilized solvents or glass ware. The deviation in the height difference between the SAM and free-standing CNM measurements (cf. figure 7.11) could be caused by the favorable deposition of contaminations onto the elevated areas during the electron irradiation. However, the definite reason for the appearance of the features could not be identified in the present thesis.

The pristine ODT SAM was irradiated inside of the AFM system over a time period of thirty minutes with electrons having an energy of $E = 100\,\mathrm{eV}$. The irradiated specimen was subsequently imaged at room temperature using the tapping mode. In figure 7.20a the respective AFM image is shown and compared to a similar image of a TPT specimen in panel (b). The structural change of the surface in comparison to the pristine SAM is obvious to see. The former self-assembled monolayer was converted into a heterogeneous network. Taking a closer look at the elevated areas one could assume a spiderweb-like arrangement. The ODT CNM has in principle a similar surface structure compared to the displayed TPT sample, but it is clear to see that the imaging conditions were better in the case of the ODT specimen and this is why the taken AFM image exhibits a sharper definition of the depressions. The line profiles in figure 7.20c exemplarily illustrate the height difference of the observed depressions. The depressions of four different sample positions at different magnifications were marked and considered for the evaluation of the depression distribution, which is shown in panel (d). For the evaluation the equivalent diameter, which assumes a circular area of the depression, was used. The distribution of the TPT CNM is provided for comparison. The range of the equivalent diameter for the ODT CNM can be described by an asymmetrical distribution function, whereas it follows a Gaussian distribution in the case of TPT. The average equivalent depression diameters do not differ much from each other. The TPT specimen exhibits an average diameter of $\bar{d}_{\mathrm{eq}} = (7 \pm 1)\,\text{Å}$. The value of the investigated ODT sample is $\bar{d}_{\mathrm{eq}} = (8 \pm 3)\,\text{Å}$ for which the standard deviation already indicates a broader size distribution. The carbon density of a SAM can be calculated from the space per molecule inside the unit cell (area per molecule) and the amount of carbon per molecule. The carbon density of the CNM can be estimated by the product of the SAM's carbon density and the remaining carbon on the surface. The latter value was obtained from the reduction of the carbon signal during XPS measurements. Taking the respective values from the literature [7, 185, 186] and from the previous experiments leads to a lower carbon density of an ODT CNM of at least $\sim 23\,\%$ compared to carbon nanomembranes made of TPT precursor molecules.

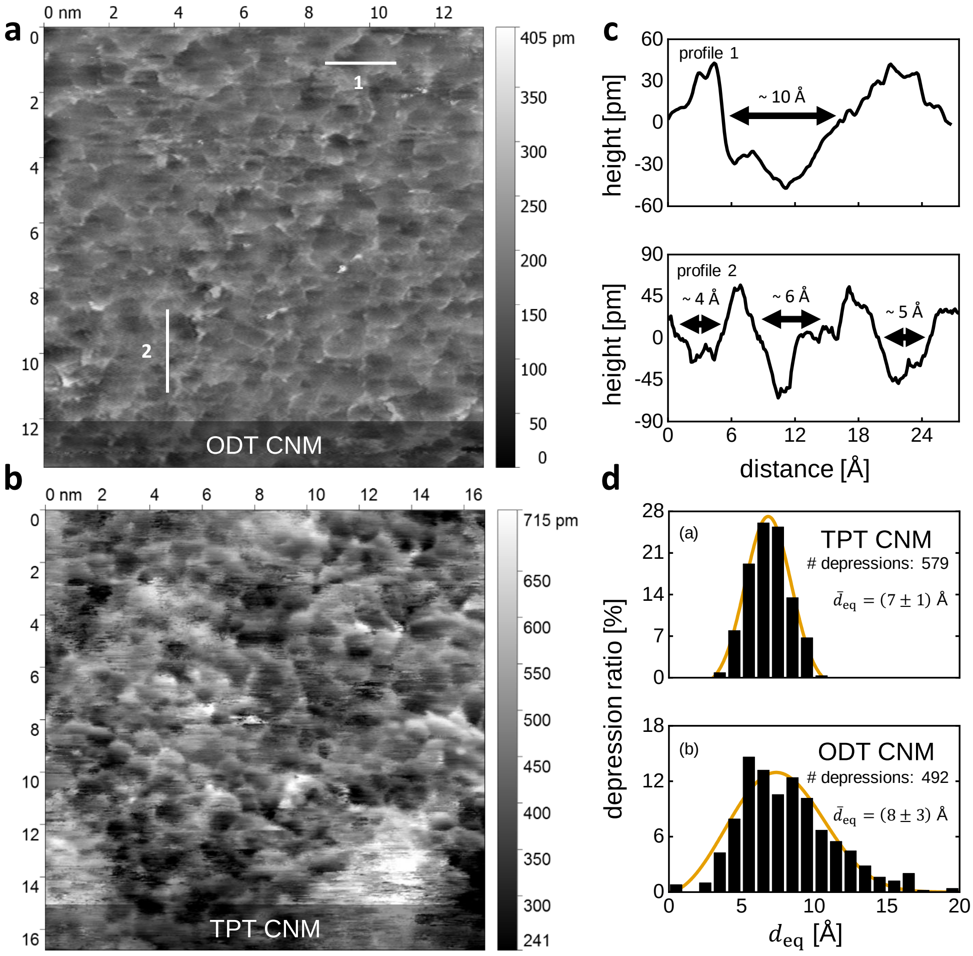

Figure 7.20.: (a) AFM image of an irradiated ODT specimen. The measurement was performed under ultra-high vacuum conditions at room temperature employing the tapping mode. The pristine SAM was irradiated over thirty minutes with electrons having an energy of $E = 100\,\mathrm{eV}$. (b) AFM image of an irradiated TPT sample imaged at $T = 93\,\mathrm{K}$ under similar conditions. Reprinted and adapted with permission from Yang *et al.* [8]. Copyright 2018 American Chemical Society. (c) Height profiles corresponding to the white lines in panel (a). (d) Depression distribution with respective distribution functions (TPT: Gaussian; ODT: Weibull) as a guide for the eye. The data for TPT have been taken from the literature [8]. The values for ODT were derived from the measured ODT sample extracted from the analysis of four different sample positions at different magnifications.

Nevertheless, the depression density of an ODT CNM was determined to be in the same range of a TPT membrane having a value of $\sim 10^{-18}\,\mathrm{m}^{-2}$ [8]. This consequently yields a more porous ODT CNM.

The porosity of an ODT carbon nanomembrane was estimated to be around $\sim (38-45)\,\%$. None of the observed depressions of TPT have a diameter which is bigger than $\bar{d}_{\mathrm{eq}} > 11\,\text{Å}$. The narrow distribution was proven to be the reason for the high selectivity of the TPT CNM. [8] The obtained results for ODT demonstrated that the CNM is not selective, which was assumed to originate from bigger pores. The AFM data point out that $18\,\%$ of the depressions have an equivalent diameter of at least $\bar{d}_{\mathrm{eq}} > 11\,\text{Å}$ and the largest observed depression has equivalent diameter of $\bar{d}_{\mathrm{eq}} \sim 20\,\text{Å}$. This fraction would also allow larger species to pass through the carbon nanomembrane and would dominate the permeation property of the ODT CNM under the assumption that the obtained depression distribution really represents the situation of a free-standing specimen. To verify this hypothesis ODT specimens have been transferred onto supportive grid structures to fabricate free-standing sample regions and TEM measurements were performed.

Due to temporary issues in the fabrication process of the CNM, the successful fabrication was verified directly in advance of the TEM investigations through the imaging with a SEM. One sample was taken from a batch of transferred specimens to check the quality of the carbon nanomembrane. In figure 7.21a an optical microscopy image of such a PMMA-stabilized ODT specimen is shown. The same sample was imaged after the solvation of PMMA by acetone by a SEM as shown in panel (b). The position and orientation of the CNM exactly matches the optical microscopy image, proving the formation of a self-supporting CNM. It was assumed that the rest of the batch exhibits the same quality. A detailed check of every specimen was not done to avoid the modification of the samples by electrons due to the imaging process. Three samples with eleven different sample areas at different magnifications were analyzed. A typical TEM image is provided in figure 7.21c.

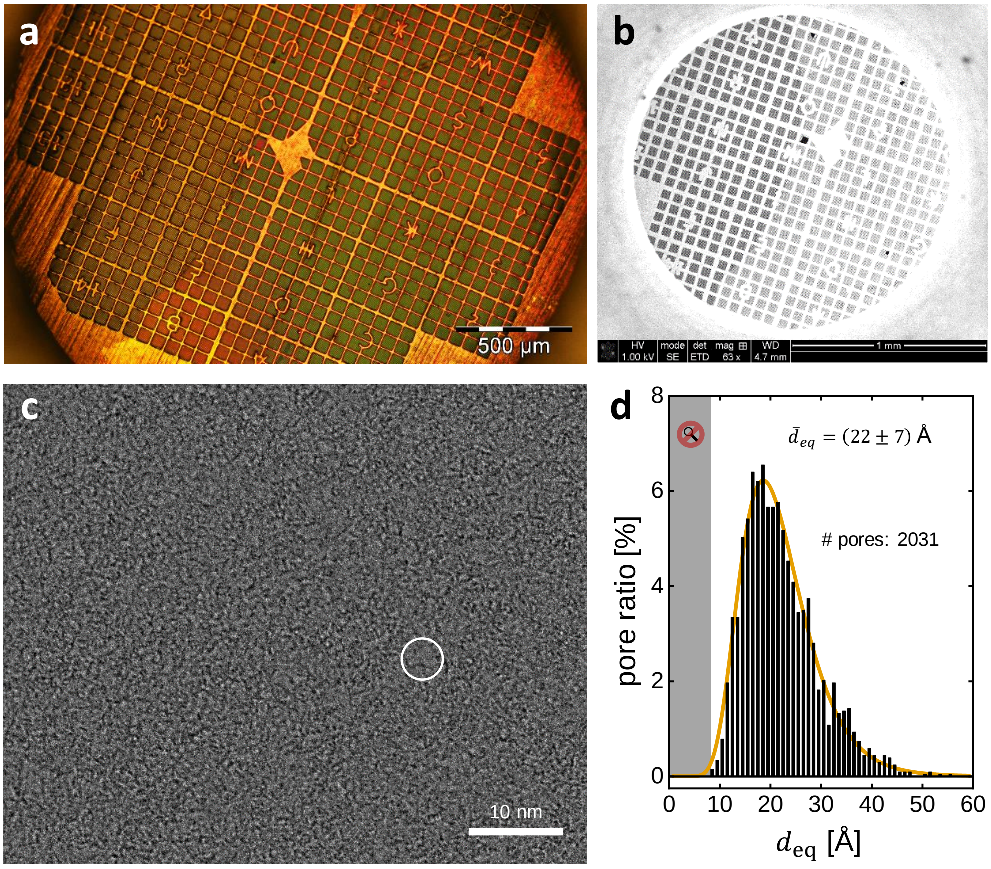

Figure 7.21.: (a) Optical microscopy image of a PMMA-coated and transferred ODT specimen. (b) SEM image of the same sample. (c) Typical TEM image of an ODT's free-standing area. The white circle visualizes the location of a pore. (d) Determined pore distribution of ODT CNMs extracted from the TEM images ($V = 80\,\mathrm{kV}$) with a respective distribution function as a guide for the eye. In total three samples with eleven different sample areas at different magnifications were taken into account. Equivalent pore diameters smaller than $\bar{d}_{\mathrm{eq}} < 8\,\text{Å}$ could not be resolved.

An amorphous membrane with intrinsic pores can be identified. The inserted white circle exemplarily illustrates the position of a pore. It was ensured that the imaging process with the used magnifications did not affect the specimen itself. An area was imaged once and the diameter of one certain pore was measured. The same spot was measured over two minutes and the diameter of the same pore matched the previously determined value. The distribution of the analyzed pores is given in panel (d). Equivalent pore diameters smaller than $\bar{d}_{\mathrm{eq}} < 8\,\text{Å}$ were not accessible due to the utilized magnification factor and the stability of the carbon nanomembrane. The distribution follows an asymmetric distribution function and has an average equivalent pore diameter of $\bar{d}_{\mathrm{eq}} = (22 \pm 7)\,\text{Å}$. Compared to the results of the AFM investigations, which were shown in figure 7.20d, the average diameter is roughly three times larger and pores with openings up to $\bar{d}_{\mathrm{eq}} = 60\,\text{Å}$ are observable. The increase of the equivalent pore diameter after the transfer procedure could be attributed to the applied mechanical stress, which led to a widening of the comparably soft carbon nanomembrane. A minimal pore density of $\sim 10^{-16}\,\mathrm{m}^{-2}$, which is two orders of magnitude lower compared to the depression density, was estimated from the data. Explanations would be on the one hand a merging process where several small pores fuse to bigger pores during the transfer process across the complete specimen, leading to a reduced density. On the other hand smaller openings were not detectable causing a deviation to the real value. The porosity was determined to be around $\sim (18 - 29)\,\%$. However, the TEM measurements reveal a broad pore distribution of free-standing ODT CNMs as it was already expected from the exploration of the permeation behavior and which is in agreement to the non-selective behavior compared to TPT carbon nanomembranes.

It was shown that self-assembled monolayers from 1-octadecanethiol (ODT) form comparably soft, highly permeable, but non-selective carbon nanomembranes with a broad pore distribution. The aliphatic chain is less stable during the cross-linking procedure compared to their aromatic counterpart TPT causing the formation of a porous and relatively open network. For this study the standard electron dose of $D = 50\,\mathrm{mC\,cm^{-2}}$ was chosen facilitating the comparison to the CNMs made form oligophenylthiols. It was found that ODT CNMs which were fabricated in that way are not suitable for the same kind of application in separation processes like TPT CNMs. Wu *et al.* [48] reported the negative resist behavior of ODT SAMs when exposed to low doses of electron irradiation ($D \geq 10\,\mathrm{mC\,cm^{-2}}$). It would be interesting to investigate whether free-standing CNMs could be produced from such samples. If so, it is imaginable that they have a narrower pore size distribution due to less material loss and might be more selective than the studied specimens. An adjustable permeation behavior, which depends on the applied electron dose to the SAM, would result. Furthermore, the properties of CNMs from alkanethiols with more than eighteen carbon atoms need to be characterized in detail. It is not inconceivable that there is a certain length of the alkyl chain which provides enough carbon material to form a denser and more selective CNM.

7.4. Fabrication of Mixed CNMs

Another approach to establish the alkanethiols as valuable precursor molecules is the modification of “classical” - meaning aromatic - carbon nanomembranes. Prior to the electron irradiation, oligophenylthiols of the SAM could be exchanged by alkanethiols. Altered properties of the resulting CNM are expected due to the different response to the electron irradiation. The subsequent section explores the last mentioned idea namely the fabrication of mixed SAMs using self-assembled monolayers of TPT from which some precursor molecules were exchanged by ODT.

In order to classify the properties of mixed carbon nanomembranes the corresponding pristine CNMs need to be well-known. Because of this it was chosen to fabricate mixed self-assembled monolayers from TPT and ODT. The first one was extensively studied in the past, whereas the latter one was investigated in the present thesis. A schematic illustration of the fabrication procedure is given in figure 7.22a. A conventionally prepared TPT SAM on Au(111) was immersed into a ethanolic solution of the alkanethiol.

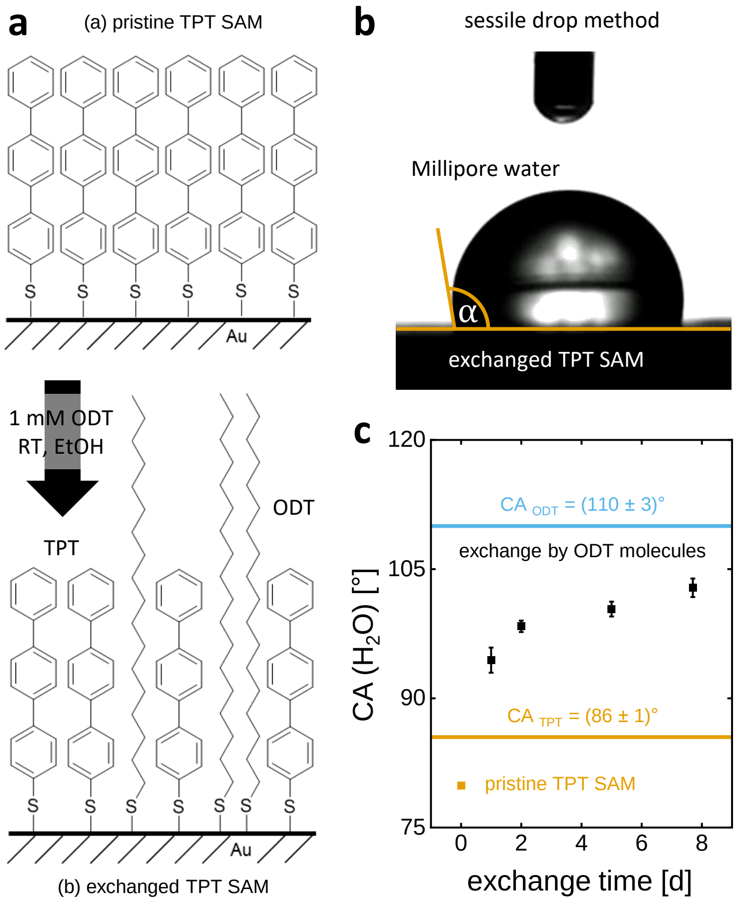

Figure 7.22.: (a) Schematic illustration of the mixed CNMs' fabrication by the exchange of the SAM's precursor molecules. (b) Typical photography for determining the contact angle α through the sessile drop method. (c) Millipore water contact angles of TPT SAMs on Au(111), which were immersed into an ethanolic ODT solution. Each sample was measured three times and the mean value is displayed with its standard deviation. The horizontal lines represent the contact angles for pure TPT [76] (orange) and ODT [187] (blue) SAMs taken from the literature.

Some of the oligophenylthiol precursor molecules were exchanged by the ODT over time leading to a mixed SAM on the gold surface. To monitor whether an exchange actually occurs the relatively simple determination of the water contact angle was used.

The sessile drop method has been employed where a drop of Millipore water was carefully placed onto the surface. A typical image is provided in figure 7.22b schematically showing the definition of the contact angle. Each sample was consecutively measured three times. The averaged values were displayed with their respective standard deviation as a function of the exchange time in panel (c). Literature values for the contact angles of the pristine SAMs were inserted as horizontal lines for comparison. The contact angle of the pure TPT SAM was determined to be CA $\sim 80\,^\circ$. A former study [76] on contact angles found a value of CA $= (86 \pm 1)\,^\circ$. The deviation of the measured pristine TPT SAM to the known contact angle can be explained by the age of the sample. The TPT sample has been measured about three weeks after its fabrication, whereas in the literature the specimen was investigated shortly after its formation. It cannot be excluded that some minor adsorbates made the TPT SAM more hydrophilic. However, the investigation of the exchanged samples was also not done directly after their fabrication so that at least a qualitative statement can be made from the data. It was found that with increasing time in the ethanolic ODT solution the contact angle increases. The surfaces become more hydrophobic indicating an exchange of the TPT precursor molecules by ODT. After a time period of nearly eight days the contact angle is CA $\sim 103\,^\circ$ showing the growth of the fraction of ODT molecules adsorbed on the surface. The comparison with the literature value of CA $= (110 \pm 3)\,^\circ$ [187] reveals that the contact angles indeed approach but do not reach the value of the pristine ODT SAM. Nevertheless, the substitution of the TPT SAM by ODT precursor molecules can be confirmed on the basis of these findings. The data also show that the exchange of the TPT self-assembled monolayer is comparably slow in contrast to the reported [160] complete substitution of a nitro-terminated biphenylthiol SAM (NBPT) by 1-octadecanethiol after five minutes under similar experimental conditions. The obvious difference in the exchange times needs to be directly related to the structure of the oligophenylthiol. Explanations could be in the case of NBPT the increased dipole moment causing an eased release of the molecules or in the case of TPT the additional phenyl nucleus strengthening the intermolecular interactions and thus retarding the exchange.

To quantify the rate of the substitution in more detail RAIRS and XPS measurements were conducted. The two precursor molecules have different characteristic vibrations in the infrared absorption spectrum which were used to identify them. For the alkanethiol ODT the asymmetric stretching vibration of its methylene (-CH_2) groups at $\tilde{\nu} \sim 2920$ cm^{-1} and for the oligophenylthiol TPT its phenyl nucleus' stretching vibration at $\tilde{\nu} \sim 1477$ cm^{-1} were the most pronounced peaks. In figure 7.23a the regions of interest of a RAIRS spectrum of a TPT specimen which was immersed into an ethanolic ODT solution for about $\sim$ 7.5 days is provided. The two characteristic peaks are clearly visible proving the existence of a mixed SAM. RAIRS measurements for different exchange times as well as for the pristine SAMs were performed and the absorbance values of the two stretching vibrations were used to extract a ratio between the two different precursor molecules. The resulting curve is given in figure 7.23b. The pure SAMs do not fit to the theoretical values of zero and one in the case of TPT and ODT, respectively. The deviation most likely originates from some minor impurities on the surface which absorb in the same range of the monitoring peaks. Nevertheless, the pristine values can still serve as a benchmark. The data follow a similar trend as the contact angle measurements. The longer the exchange time, the larger becomes the proportion of ODT. Interestingly, the fraction seems to saturate after an exchange time of $\sim$ 4 days, indicating a stagnation of the substitution and thus an equilibrium between the molecules' adsorption and desorption processes.

With regard to its high surface sensitivity XPS was further employed to evaluate the composition of the specimens. In figure 7.23c the C1s scan of the same sample as in panel (a) is shown.

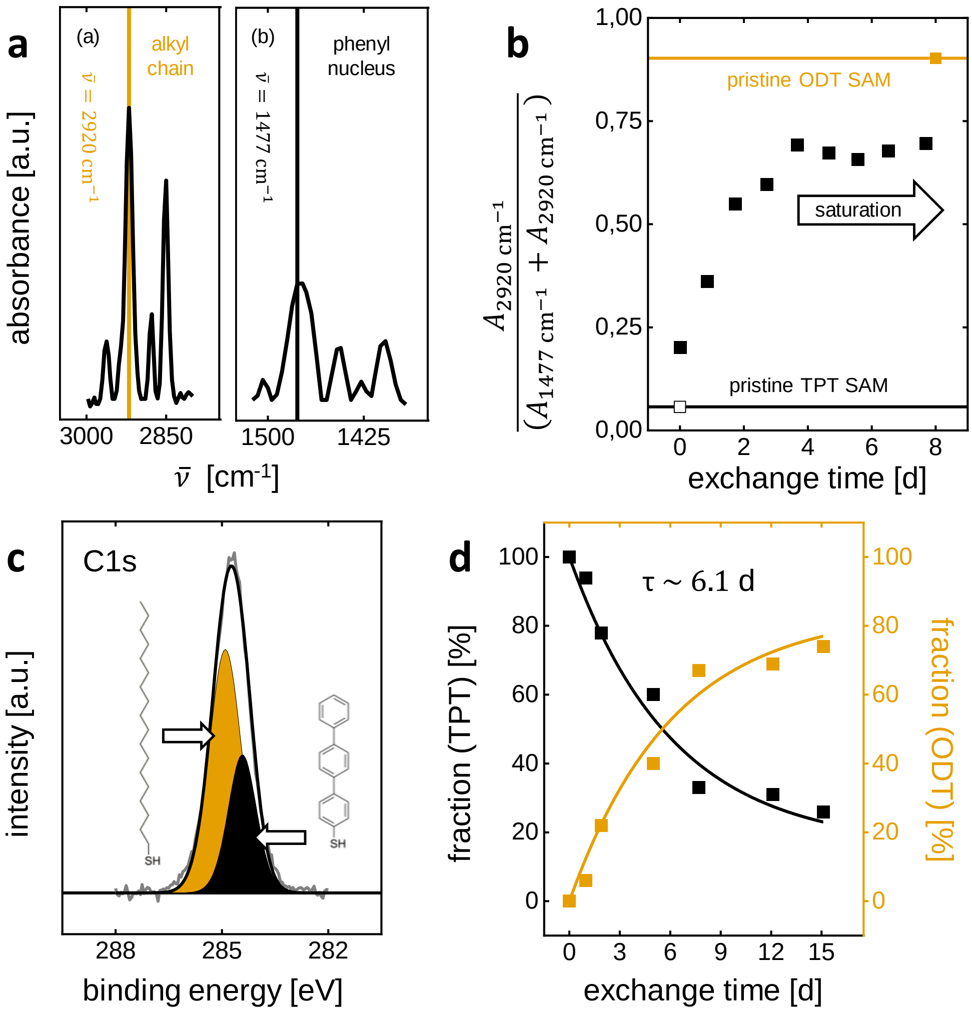

Figure 7.23.: (a) Selected regions of an exchanged TPT specimen's RAIRS spectrum. The sample was exchanged by ODT for about ~ 7.5 days. The respective vibrations of the different precursor molecules which were chosen for further analysis are highlighted. (b) RAIRS absorbance ratio of the characteristic vibration of the alkyl chain as a function of the TPT SAM's exchange time. (c) C1s XP spectra of the same sample as in panel (a). The peak was deconvoluted into the contribution of the ODT and TPT precursor molecule. (d) Precursor fractions extracted from the XPS analysis of exchanged TPT specimens with a fitted exponential decay according to $y = A_1 \exp(-x/t_1) + y_0$ to estimate the time constant $t_1 = \tau$ of the exchange.

The overall peak was deconvoluted into the contributions of the ODT and TPT precursor molecule. The center position for each peak was obtained from the pristine SAMs. These binding energies were fixed when fitting the carbon peak of the mixed SAMs. The processing of the data revealed a ratio of $\sim 33\,\%$ TPT and $\sim 67\,\%$ ODT for the mixed SAM, which is comparable to the ratio derived from the RAIRS measurements. Taking a look at the proportions of the other samples in figure 7.23d shows that there is no saturation in the substitution of the TPT molecules during the investigated time period. Instead, an exponential curve shape could be assumed leading to a time constant of the exchange kinetic of $\tau \sim 6.1\,\mathrm{d}$. A complete substitution could not even be achieved after two weeks. The SAM has still an amount of roughly $\sim 20\,\%$ of the former TPT precursor molecules. Thus, the XPS study proved the slow kinetic of the substitution and demonstrates that is not suitable for the determination of the exchange kinetics in this case RAIRS. From the time constant derived by XPS an easy control of the amount of exchanged molecules and consequently the adjustable CNM's properties are expected.

For the characterization of the CNMs' properties it needed to be shown that the mixed SAMs form stable and self-supporting carbon nanomembranes. HIM images were taken in the dark field mode after the electron irradiation and the subsequent transfer onto a supportive structure. In figure 7.24 and figure 7.25 the images for a mixed CNM which rested around $\sim 7\,\mathrm{days}$ in the ethanolic ODT solution are provided. A low magnification image of the CNM is shown in figure 7.24. An almost perfect coverage of the quantifoil holey carbon foil can be seen. No macroscopic defects are detectable at higher magnification views. This finding is in contrast to the study of Chinaryan [160] in which nanopores could be reproducibly formed. In that study NBPT was utilized as a precursor molecule. It might be that the nitro-terminated biphenylthiol could not cross-link with the present ODT molecules in a proper way yielding a porous membrane. However, the inability of ODT to form a CNM by itself is disproved by the present thesis. Another explanation for the differing results could be the unintended milling of pores caused by the imaging procedure in the secondary electron mode.

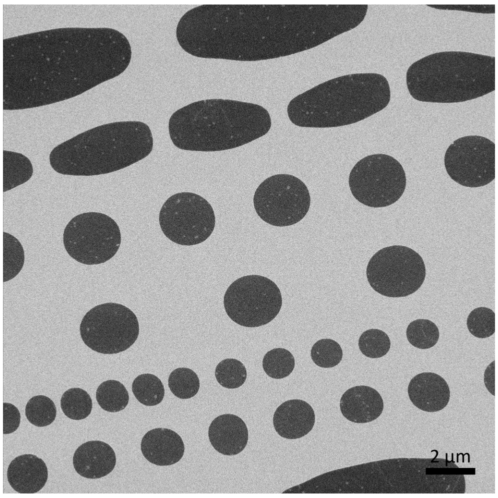

Figure 7.24.: Low magnification HIM image (dark field transmission mode) of a mixed CNM. The mixed SAM was fabricated by the immersion of a TPT SAM into an ethanolic ODT solution for roughly seven days.

The stability of the mixed TPT-ODT carbon nanomembrane was tested by the subsequent imaging of the same sample area. An image series with sixteen images in total was measured. The first and the last image is given in panel (a) and (b) of figure 7.25, respectively. The CNM in panel (b) shows some scattered nanopores, which originate from the applied dose. Assuming a circular area, the diameters of some randomly chosen pores were in a range of maximum 15 nm. Due to the increase of carbon contaminations with each acquired image, the carbon nanomembrane appears brighter over the course of the series. Apart from that a robust and mechanically stable mixed CNM could be verified.

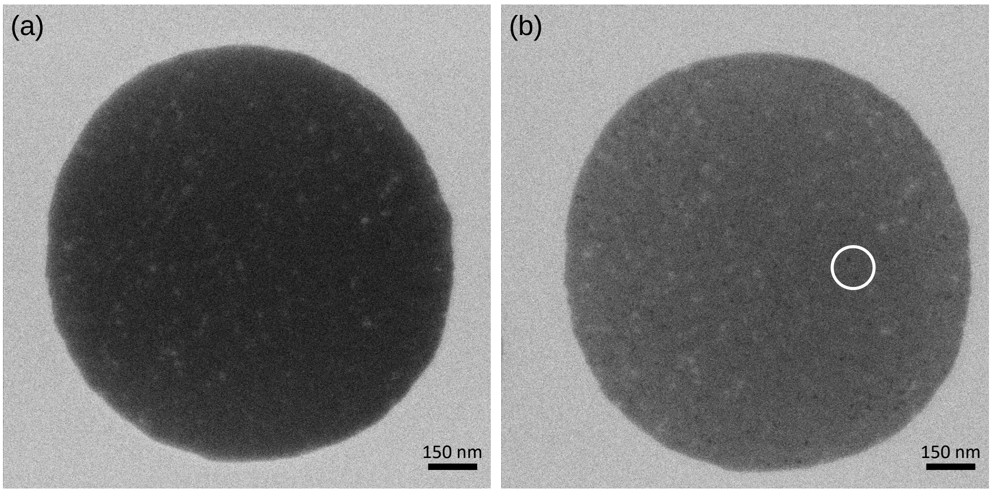

Figure 7.25.: High magnification HIM image (dark field transmission mode) series, with sixteen images in total, of the same mixed CNM as in figure 7.24. First (a) and last (b) image of the image series. The white circle exemplarily marks induced nanopores.

The possibility to fabricate mechanically stable mixed carbon nanomembranes with a comparably slow exchange rate was found. Based on this outcome and on the results of the previous section with respect to the properties of ODT CNMs, the investigation of the permeation properties of mixed carbon nanomembranes outlines an interesting starting point for further studies. The determination through gas permeation measurements seems to be most appropriate for this purpose. The ability to investigate multiple gases and vapors with the same specimen without touching the sample facilitates a fast screening under the same experimental conditions. As an alternative the gravimetric anlaysis could be used to explore the water permeation first to get to know the effect of the different immersion times. It is expected that the substitution with ODT leads to an enhanced water permeation. On the other hand the lack of selectivity of the ODT CNM needs to be considered, which might enable larger species to pass through the mixed CNM. It is assumed that the amount of permeating species can be controlled by the proportion of exchanged TPT precursor molecules. Another way to modify the permeation properties would be the usage of 1-dodecanethiol (DDT, C12) as a substitution agent. As it was shown in section 7.2 the precursor molecule is not able to form a free-standing carbon nanomembrane and would most likely induce the formation of defects in the resulting mixed CNM. Of course, the respective exchange kinetic of the desired combination of precursor molecules needs to be determined in advance. Further, the overall rate of the substitution can be promoted by applying very low electron doses or by the usage of ultraviolet light as shown by Zharnikov and coworkers [147, 188–190]. The latter approach additionally allows to easily control the exchanged regions, which could lead in combination with the former ideas to custom-made and patterned mixed CNMs.

7.5. Summary of the Chapter

This chapter focused on the question whether it is possible to fabricate carbon nanomembranes from alkanethiol precursor molecules and explored the application potential of the respective CNMs.

In the first section the influence of the alkyl chain length on the formation process of self-supporting carbon nanomembranes was investigated. Among other results, spectroscopic evidence was provided, clearly proving the change of the SAM's hybridization during the electron irradiation. It was outlined that the stability of the carbon nanomembrane depends on the amount of carbon material which had been available on the surface. Two distinct transitions were found through the HIM analysis under the given experimental conditions. SAMs from 1-dodecanethiol (DDT, C12) are not sufficient to form a stable carbon nanomembrane. Fragile and porous CNMs could be produced form self-assembled monolayers of 1-tetradecanethiol (TDT, C14) and 1-hexadecanethiol (HDT, C16). Stable carbon nanomembranes were obtained from precursor molecules which have at least a total number of eighteen carbon atoms in the alkyl chain. In the present thesis 1-octadecanethiol (ODT, C18) and 1-docosanethiol (DST, C22) were utilized. Performed control experiments disproved the possibility to form a CNM, as they were observed in the course of the experiments, from solely carbon contaminations. Consequently, it was shown for the first time to the best of my knowledge that alkanethiols can serve as molecular building blocks for the preparation of carbon nanomembranes.

The second section was concerned with the detailed characterization of CNMs made of ODT precursor molecules. It was found that the carbon nanomembrane is mechanically stable, but rather soft compared to other CNMs. The corresponding Young's modulus is $\bar{E} = (592 \pm 151)\,\mathrm{MPa}$ and thus similar in rigidity to biological membranes. The investigation of the membrane's permeation behavior revealed a remarkable water permeance of $\bar{P}\,(\mathrm{H_2O}) = (4.30 \pm 1.07) \cdot 10^{-4}\ \mathrm{mol\,m^{-2}\,s^{-1}\,Pa^{-1}}$, but it is accompanied by a lack of selectivity so that even larger species like tetrahydrofuran or *n*-hexane are able to pass through the membrane. The topographical analysis showed a broad depression distribution on the surface having an average diameter of $\bar{d}_{\mathrm{eq}} = (8 \pm 3)\,\mathrm{Å}$. 18 % of the depressions were determined to be bigger than $\bar{d}_{\mathrm{eq}} > 11\,\mathrm{Å}$, indicating an unselective CNM. The apparent porosity of $\sim\ (38 - 45)\,\%$ and depression density of $\sim\ 10^{-18}\,\mathrm{m^{-2}}$ were in the same range like TPT CNMs. The free-standing TEM analysis finally proved pores up to $\bar{d}_{\mathrm{eq}} = 60\,\mathrm{Å}$ and an average equivalent pore diameter of $\bar{d}_{\mathrm{eq}} = (22 \pm 7)\,\mathrm{Å}$, which explained the observed permeation behavior. A minimal pore density of $\sim 10^{-16}\,\mathrm{m^{-2}}$ and a porosity of $\sim\ (18 - 29)\,\%$ could be estimated from the data. The differing results of the depressions on the support and the free-standing pores could be caused (i) by a large number of small pores which could not be observed during the TEM investigation or (ii) by the fact that not all of the depressions which were observed with the AFM are continuous. Although the ODT carbon nanomembrane cannot be used for separation processes where the cut-off is below six nanometer, it might be used in the field of ultrafiltration. Furthermore, it demonstrated the opportunity to employ alkanethiol precursor molecules for tailoring the properties of mixed CNMs.

The last section dealt with the fabrication of mixed carbon nanomembranes with custom-made properties. A TPT SAM served as a exemplary system and ODT was taken as a substitution agent. Spectroscopic analyses defined the time constant of the exchange kinetic to be around $\tau \sim 6.1\,\mathrm{d}$. Provided HIM images demonstrated a self-supporting mixed CNM without any macroscopic defects. The performed experiments provide a profound basis for future studies on that topic.

8. Conclusion of the Thesis

The present thesis covered three different issues, namely (i) the functionalization of carbon nanomembranes with an emphasis on the immobilization of proteins, (ii) the detection of permeating species in aqueous solution through free-standing carbon nanomembranes, and (iii) the fabrication and application of carbon nanomembranes which were produced from self-assembled monolayers of alkanethiol precursor molecules. This conclusion will outline major results. For a more detailed description it is kindly referred to the respective summaries at the end of each chapter.

Studies on transmembrane processes involving proteins are still challenging due to a lack of a suitable test systems. The surface of the nanometer-thin carbon nanomembrane could be functionalized in a proper way making the new material an attractive template. It was found that for the coupling of proteins to the carbon nanomembrane, comparably harsh reaction conditions for the linker attachment are required. An efficient way to functionalize the surface is the usage of the copper-free click chemistry involving 2-azidoacetyl chloride as the mediator molecule and dibenzocyclooctyne derivatives which are responsible for the interaction with the protein. The shown approach to irreversibly immobilize the proteins to the carbon nanomembrane was most promising. The bonding occurs through the formation of a thioether moiety between the functional maleimide group of the linker molecule and the cysteine moieties of the protein. Advantages of this method are the relative short length of the resulting coupling structure, which in principle facilitates the possibility to perform transmembrane FRET measurements, and the easily subclonable cysteine tag if the desired protein lacks of accessible moieties. The presented results can be further deployed to investigate biological processes with the carbon nanomembrane as a robust model system or to explore its surface functionalization for specific detection reactions in terms of the lab-on-a-chip design.

The characterization of the carbon nanomembrane's selectivity is important when thinking of its potential application in industrial separation processes. Up to now, gravimetric analyses as well as gas permeation and ion conductance measurements were employed to define the separation ability of carbon nanomembranes. However, it was still challenging to measure uncharged permeating species in the liquid phase. In the course of the present thesis the determination of apparent diffusion coefficients in aqueous solution by using radioactive tracers has been demonstrated. A mathematical model has been developed to extract the respective coefficients. The method was validated by reference measurements through an open orifice. The obtained apparent diffusion coefficients matched the typical range of reported literature values. TPT carbon nanomembranes were chosen to serve as a test system. It turned out that phosphorous-32 can be used as an internal control agent because the tracer was not able to pass through the carbon nanomembrane. Surprisingly, the derived apparent diffusion coefficients of hydrogen-3 and carbon-14 were quite similar having values of $D'_{^3\mathrm{H}}(\mathrm{CNM}) \sim 10^{-13}\,\mathrm{m^2\,s^{-1}}$ and $D'_{^{14}\mathrm{C}}(\mathrm{CNM}) \sim 10^{-12}\,\mathrm{m^2\,s^{-1}}$, respectively. To the best of my knowledge, it was the first time that the permeation through CNMs in an aqueous solution was investigated with such a method. The results indicated neutral compounds to be the favorable carrier species through the carbon nanomembrane. For the carbonaceous species carbon dioxide is believed to be the transport compound. Due to the lowered driving force, the apparent diffusion coefficient was determined to be $D'_{^{14}\mathrm{CO_2}}(\mathrm{CNM}) \sim 10^{-11}\,\mathrm{m^2\,s^{-1}}$. The presented approach can be applied to study almost every radioactively labeled molecule and lays the foundation for a systematic analysis of the separation efficiency in aqueous solution. The prospective knowledge will contribute to advance the evaluation of the commercial application of carbon nanomembranes and modeling attempts regarding the involved transport mechanisms.

Carbon nanomembranes are typically made from oligophenylthiol precursor molecules like TPT. The higher homologous compounds or compounds with certain functional chemical groups are often not commercially available, which entails costly customized syntheses and limits the range of available molecular building blocks. An alternative would be the usage of alkanethiols, but the literature was inconclusive about the stability of those compounds during the cross-linking procedure. Different aliphatic molecules with a variation in the alkyl chain length were investigated to tackle this ambiguity. The results of the HIM analysis impressively proved the formation of free-standing, but fragile and porous, carbon nanomembranes from molecules with at least fourteen carbon atoms in the alkyl chain. Starting with 1-octadecanethiol (ODT, C18) mechanically stable and non-defective samples could be prepared. ODT carbon nanomembranes were chosen to be characterized in more detail due to the same number of carbon atoms as the well-known TPT. The Young's modulus was determined to be $\bar{E} = (592 \pm 151)\,\mathrm{MPa}$ indicating a comparably soft membrane. The investigation of the permeation behavior revealed an unselective carbon nanomembrane, whose free-standing samples exhibit an average equivalent pore diameter of $\bar{d}_{\mathrm{eq}} = (22 \pm 7)\,\text{Å}$. For comparison, on the metallic substrate the average diameter of the depressions is $\bar{d}_{\mathrm{eq}} = (8 \pm 3)\,\text{Å}$. In general, this example points out that differences can occur between the CNMs on the metallic substrate and the corresponding free-standing ones. Based on the permeation results, the modification of conventionally prepared carbon nanomembranes by exchanging a certain proportion of the self-assembled monolayer's precursor molecules is an attractive approach to control the selectivity of the membrane. Initial studies for the mixed CNM consisting of TPT and ODT molecules were performed. It was found that the rate of substitution is rather slow, having a time constant of $\tau \sim 6.1\,\mathrm{d}$. Thus, an easy control of the exchanged proportion is given. To the best of my knowledge, the performed experiments demonstrated the fabrication of carbon nanomembranes from alkanethiol self-assembled monolayers for the first time and further underlined their application potential revealing the capabilities of these molecular building blocks.

A functionalization strategy was presented to irreversibly bind proteins to the surface of the CNM. Due to proteins' high efficiency in executing specific tasks, it is conceivable that the overall performance of such a designed membrane will benefit. Furthermore, a complete new class of molecular building blocks was introduced, allowing (i) to screen for undiscovered membrane materials and (ii) to attune the performance of existing carbon nanomembranes to a specified application. The presented radioactive tracer method complements the available monitoring techniques in order to judge the separating efficiency of tailored CNMs. To conclude, the findings of the present thesis provide some fundamental knowledge about new ways to alter and monitor the properties of carbon nanomembranes. Hopefully, this will help to develop efficient custom-made separation membranes to meet the world's emerging demands in the next decades.

9. Bibliography

[1] United Nations, Department of Economic and Social Affairs, Population Division. *World Population Prospects 2019: Highlights (ST/ESA/SER.A/423)* 978-92-1-148316-1. `https://population.un.org/wpp/Publications/Files/WPP2019_Highlights.pdf` (United Nations, New York, NY, 2019).

[2] Rolfe Eberhard. *Access to Water and Sanitation in Sub-Saharan Africa: Part I - Sythesis Report: Review of Sector Reforms and Investments, Key Findings to Inform Future Support to Sector Development* `http://www.oecd.org/water/GIZ_2018_Access_Study_Part%20I_Synthesis_Report.pdf` (Deutsche Gesellschaft für Internationale Zusammenarbeit (GIZ) GmbH, Eschborn, 2019).

[3] IEA - International Energy Agency. *Africa Energy Outlook 2019: World Energy Outlook Special Report* `https://www.iea.org/reports/africa-energy-outlook-2019` (IEA Publications, Paris, France, 2019).

[4] Strathmann, H. Membrane Separation Processes: Current Relevance and Future Opportunities. *AIChE Journal* **47,** 1077–1087. doi:`10.1002/aic.690470514` (2001).

[5] *Membrane Separation Principles and Applications: From Material Selection to Mechanisms and Industrial Uses* (eds Ismail, A. F., Rahman, M. A., Othman, M. H. D. & Matsuura, T.) 978-0-12-812815-2. doi:`10.1016/C2016-0-04031-7` (Elsevier, Amsterdam, Netherlands, 2019).

[6] Turchanin, A. & Gölzhäuser, A. Carbon Nanomembranes. *Advanced materials (Deerfield Beach, Fla.)* **28,** 6075–6103. doi:`10.1002/adma.201506058` (2016).

[7] Angelova, P., Vieker, H., Weber, N.-E., Matei, D., Reimer, O., *et al.* A universal scheme to convert aromatic molecular monolayers into functional carbon nanomembranes. *ACS nano* **7,** 6489–6497. doi:`10.1021/nn402652f` (2013).

[8] Yang, Y., Dementyev, P., Biere, N., Emmrich, D., Stohmann, P., *et al.* Rapid Water Permeation Through Carbon Nanomembranes with Sub-Nanometer Channels. *ACS nano* **12,** 4695–4701. doi:`10.1021/acsnano.8b01266` (2018).

[9] Naberezhnyi, D., Gölzhäuser, A. & Dementyev, P. Water-Assisted Permeation of Gases in Carbon Nanomembranes. *The Journal of Physical Chemistry Letters* **10,** 5598–5601. doi:`10.1021/acs.jpclett.9b02321` (2019).

[10] Yang, Y., Hillmann, R., Qi, Y., Korzetz, R., Biere, N., *et al.* Ultrahigh Ionic Exclusion through Carbon Nanomembranes. *Advanced materials (Deerfield Beach, Fla.),* e1907850. doi:`10.1002/adma.201907850` (2020).

[11] Zhang, B. in *Physical fundamentals of nanomaterials* (ed Zhang, B.) 177–210 (Chemical Industry Press, Oxford, 2018). 9780124104174. doi:`10.1016/B978-0-12-410417-4.00005-8`.

[12] Zheng, Y. in *Bioinspired Design of Materials Surfaces* (ed Zheng, Y.) 99–146 (Elsevier, [S.l.], 2019). 9780128148433. doi:`10.1016/B978-0-12-814843-3.00003-X`.

[13] Bigelow, W. C., Pickett, D. L. & Zisman, W. A. Oleophobic monolayers. *Journal of Colloid Science* **1,** 513–538. doi:`10.1016/0095-8522(46)90059-1` (1946).

[14] Ulman, A. Formation and Structure of Self-Assembled Monolayers. *Chemical reviews* **96,** 1533–1554. doi:`10.1021/cr9502357` (1996).

[15] Love, J. C., Estroff, L. A., Kriebel, J. K., Nuzzo, R. G. & Whitesides, G. M. Self-assembled monolayers of thiolates on metals as a form of nanotechnology. *Chemical reviews* **105,** 1103–1169. doi:`10.1021/cr0300789` (2005).

[16] Kumar, A., Biebuyck, H. A. & Whitesides, G. M. Patterning Self-Assembled Monolayers: Applications in Materials Science. *Langmuir* **10,** 1498–1511. doi:`10.1021/la00017a030` (1994).

[17] Bishop, A. R. & Nuzzo, R. G. Self-assembled monolayers: Recent developments and applications. *Current Opinion in Colloid & Interface Science* **1,** 127–136. doi:`10.1016/S1359-0294(96)80053-7` (1996).

[18] Chaki, N. K., Aslam, M., Sharma, J. & Vijayamohanan, K. Applications of self-assembled monolayers in materials chemistry. *Journal of Chemical Sciences* **113,** 659–670. doi:`10.1007/BF02708798` (2001).

[19] Aslam, M., Chaki, N. K., Sharma, J. & Vijayamohanan, K. Device applications of self-assembled monolayers and monolayer-protected nanoclusters. *Current Applied Physics* **3,** 115–127. doi:`10.1016/S1567-1739(02)00180-3` (2003).

[20] Turchanin, A. & Gölzhäuser, A. Carbon nanomembranes from self-assembled monolayers: Functional surfaces without bulk. *Progress in Surface Science* **87,** 108–162. doi:`10.1016/j.progsurf.2012.05.001` (2012).

[21] Eck, W., Küller, A., Grunze, M., Völkel, B. & Gölzhäuser, A. Freestanding Nanosheets from Crosslinked Biphenyl Self-Assembled Monolayers. *Advanced Materials* **17,** 2583–2587. doi:`10.1002/adma.200500900` (2005).

[22] Rhinow, D., Vonck, J., Schranz, M., Beyer, A., Gölzhäuser, A. & Hampp, N. Ultrathin conductive carbon nanomembranes as support films for structural analysis of biological specimens. *Physical chemistry chemical physics : PCCP* **12,** 4345–4350. doi:`10.1039/b923756a` (2010).

[23] Zhang, X., Neumann, C., Angelova, P., Beyer, A. & Gölzhäuser, A. Tailoring the mechanics of ultrathin carbon nanomembranes by molecular design. *Langmuir* **30,** 8221–8227. doi:`10.1021/la501961d` (2014).

[24] Turchanin, A., Beyer, A., Nottbohm, C. T., Zhang, X., Stosch, R., Sologubenko, A., Mayer, J., Hinze, P., Weimann, T. & Gölzhäuser, A. One Nanometer Thin Carbon Nanosheets with Tunable Conductivity and Stiffness. *Advanced Materials* **21,** 1233–1237. doi:`10.1002/adma.200803078` (2009).

[25] Zhang, X., Beyer, A. & Gölzhäuser, A. Mechanical characterization of carbon nanomembranes from self-assembled monolayers. *Beilstein Journal of Nanotechnology* **2,** 826–833. doi:`10.3762/bjnano.2.92` (2011).

[26] Penner, P., Zhang, X., Marschewski, E., Behler, F., Angelova, P., Beyer, A., Christoffers, J. & Gölzhäuser, A. Charge Transport through Carbon Nanomembranes. *The Journal of Physical Chemistry C* **118,** 21687–21694. doi:`10.1021/jp506689n` (2014).

[27] Zhang, X., Marschewski, E., Penner, P., Beyer, A. & Gölzhäuser, A. Investigation of electronic transport through ultrathin carbon nanomembrane junctions by conductive probe atomic force microscopy and eutectic Ga–In top contacts. *Journal of Applied Physics* **122,** 055103. doi:`10.1063/1.4995533` (2017).

[28] Paul Penner. *Untersuchung der elektrischen und dielektrischen Eigenschaften von Kohlenstoffnanomembrane und ihre Anwendungen in Kohlenstoffnanokondensatoren* PhD Thesis (Bielefeld University, Bielefeld, 2018). `https://pub.uni-bielefeld.de/record/2931045`.

[29] Zhang, X., Marschewski, E., Penner, P., Weimann, T., Hinze, P., Beyer, A. & Gölzhäuser, A. Large-Area All-Carbon Nanocapacitors from Graphene and Carbon Nanomembranes. *ACS nano* **12,** 10301–10309. doi:`10.1021/acsnano.8b05490` (2018).

[30] Turchanin, A., Weber, D., Büenfeld, M., Kisielowski, C., Fistul, M. V., Efetov, K. B., Weimann, T., Stosch, R., Mayer, J. & Gölzhäuser, A. Conversion of self-assembled monolayers into nanocrystalline graphene: structure and electric transport. *ACS nano* **5,** 3896–3904. doi:`10.1021/nn200297n` (2011).

[31] Rhinow, D., Weber, N.-E. & Turchanin, A. Atmospheric Pressure, Temperature-Induced Conversion of Organic Monolayers into Nanocrystalline Graphene. *The Journal of Physical Chemistry C* **116,** 12295–12303. doi:`10.1021/jp301877p` (2012).

[32] Matei, D. G., Weber, N.-E., Kurasch, S., Wundrack, S., Woszczyna, M., *et al.* Functional single-layer graphene sheets from aromatic monolayers. *Advanced materials (Deerfield Beach, Fla.)* **25,** 4146–4151. doi:`10.1002/adma.201300651` (2013).

[33] Neumann, C., Kaiser, D., Mohn, M. J., Füser, M., Weber, N.-E., *et al.* Bottom-Up Synthesis of Graphene Monolayers with Tunable Crystallinity and Porosity. *ACS nano* **13,** 7310–7322. doi:`10.1021/acsnano.9b03475` (2019).

[34] Zheng, Z., Nottbohm, C. T., Turchanin, A., Muzik, H., Beyer, A., Heilemann, M., Sauer, M. & Gölzhäuser, A. Janus nanomembranes: a generic platform for chemistry in two dimensions. *Angewandte Chemie (International ed. in English)* **49,** 8493–8497. doi:`10.1002/anie.201004053` (2010).

[35] Schmelmer, U., Paul, A., Küller, A., Steenackers, M., Ulman, A., Grunze, M., Gölzhäuser, A. & Jordan, R. Nanostructured polymer brushes. *Small (Weinheim an der Bergstrasse, Germany)* **3,** 459–465. doi:`10.1002/smll.200600528` (2007).

[36] Turchanin, A., Tinazli, A., El-Desawy, M., Großmann, H., Schnietz, M., Solak, H. H., Tampé, R. & Gölzhäuser, A. Molecular Self-Assembly, Chem-

ical Lithography, and Biochemical Tweezers: A Path for the Fabrication of Functional Nanometer-Scale Protein Arrays. *Advanced Materials* **20,** 471–477. doi:`10.1002/adma.200702189` (2008).

[37] Amin, I., Steenackers, M., Zhang, N., Beyer, A., Zhang, X., Pirzer, T., Hugel, T., Jordan, R. & Gölzhäuser, A. Polymer carpets. *Small (Weinheim an der Bergstrasse, Germany)* **6,** 1623–1630. doi:`10.1002/smll.201000448` (2010).

[38] Kankate, L., Aguf, A., Großmann, H., Schnietz, M., Tampé, R., Turchanin, A. & Gölzhäuser, A. Vapor Phase Exchange of Self-Assembled Monolayers for Engineering of Biofunctional Surfaces. *Langmuir* **33,** 3847–3854. doi:`10.1021/acs.langmuir.6b04207` (2017).

[39] Ai, M., Shishatskiy, S., Wind, J., Zhang, X., Nottbohm, C. T., *et al.* Carbon nanomembranes (CNMs) supported by polymer: mechanics and gas permeation. *Advanced materials (Deerfield Beach, Fla.)* **26,** 3421–3426. doi:`10.1002/adma.201304536` (2014).

[40] Yang, Y. *Mass Transport Through Freestanding Carbon Nanomembranes* PhD Thesis (Bielefeld University, Bielefeld, 2019). doi:`10.4119/unibi/2935598`. `https://pub.uni-bielefeld.de/record/2935598`.

[41] Dementyev, P., Wilke, T., Naberezhnyi, D., Emmrich, D. & Gölzhäuser, A. Vapour permeation measurements with free-standing nanomembranes. *Physical chemistry chemical physics : PCCP* **21,** 15471–15477. doi:`10.1039/c9cp03038g` (2019).

[42] Dementyev, P., Yang, Y., Rezvova, M. & Gölzhäuser, A. Molecular Jamming in Tortuous Nanochannels. *The Journal of Physical Chemistry Letters* **11,** 238–242. doi:`10.1021/acs.jpclett.9b03256` (2020).

[43] Turchanin, A., Käfer, D., El-Desawy, M., Wöll, C., Witte, G. & Gölzhäuser, A. Molecular mechanisms of electron-induced cross-linking in aromatic SAMs. *Langmuir* **25,** 7342–7352. doi:`10.1021/la803538z` (2009).

[44] Neumann, C., Szwed, M., Frey, M., Tang, Z., Kozieł, K., Cyganik, P. & Turchanin, A. Preparation of Carbon Nanomembranes without Chemically Active Groups. *ACS applied materials & interfaces* **11,** 31176–31181. doi:`10.1021/acsami.9b09603` (2019).

[45] Waske, P. A., Meyerbröker, N., Eck, W. & Zharnikov, M. Self-Assembled Monolayers of Cyclic Aliphatic Thiols and Their Reaction toward Electron Irradiation. *The Journal of Physical Chemistry C* **116,** 13559–13568. doi:`10.1021/jp210768y` (2012).

[46] Gölzhäuser, A., Geyer, W., Stadler, V., Eck, W., Grunze, M., Edinger, K., Weimann, T. & Hinze, P. Nanoscale patterning of self-assembled monolayers with electrons. *Journal of Vacuum Science & Technology B: Microelectronics and Nanometer Structures* **18,** 3414–3418. doi:`10.1116/1.1319711` (2000).

[47] Zharnikov, M. & Grunze, M. Modification of thiol-derived self-assembling monolayers by electron and x-ray irradiation: Scientific and lithographic aspects. *Journal of Vacuum Science & Technology B: Microelectronics and Nanometer Structures* **20,** 1793–1807. doi:`10.1116/1.1514665` (2002).

[48] Wu, Y.-T., Liao, J.-D., Weng, C.-C., Hesieh, Y.-T., Chen, C.-H., Wang, M.-C. & Zharnikov, M. Alkanethiolate Self-Assembled Monolayers As a Negative or Positive Resist for Electron Lithography. *The Journal of Physical Chemistry C* **113,** 4543–4548. doi:`10.1021/jp808617y` (2009).

[49] Zhou, C., Jones, J. C., Trionfi, A., Hsu, J. W. P. & Walker, A. V. Electron Beam-Induced Damage of Alkanethiolate Self-Assembled Monolayers Adsorbed on GaAs (001): A Static SIMS Investigation. *The Journal of Physical Chemistry C* **114,** 5400–5409. doi:`10.1021/jp905612p` (2010).

[50] Schmid, M., Wan, X., Asyuda, A. & Zharnikov, M. Modification of Self-Assembled Monolayers by Electron Irradiation: The Effect of Primary En-

ergy (10–500 eV). *The Journal of Physical Chemistry C* **123,** 28301–28309. doi:`10.1021/acs.jpcc.9b09125` (2019).

[51] Kärger, J., Ruthven, D. M. & Theodorou, D. N. *Diffusion in Nanoporous Materials* 978-3-527-31024-1 (Wiley-VCH Verlag GmbH & Co. KGaA, Weinheim, 2012).

[52] Crank, J. *The Mathematics of Diffusion* 2. ed., reprint. 0 19 853344 6 (Clarendon Press, Oxford, 1976).

[53] Atkins, P. W. & de Paula, J. *Atkins' Physical Chemistry* Tenth edition. 978-0-19-969740-3 (Oxford University Press, Oxford, 2014).

[54] Saito, Y. A Theoretical Study on the Diffusion Current at the Stationary Electrodes of Circular and Narrow Band Types. *Review of Polarography* **15,** 177–187. doi:`10.5189/revpolarography.15.177` (1968).

[55] Cussler, E. L. *Diffusion: Mass Transfer in Fluid Systems* 3rd ed. 978-0-511-47892-5 (Cambridge University Press, Leiden, 2009).

[56] Ismail, A. F., Chandra Khulbe, K. & Matsuura, T. *Gas Separation Membranes* 978-3-319-01094-6. doi:`10.1007/978-3-319-01095-3` (Springer International Publishing, Cham, 2015).

[57] Baker, R. W. *Membrane Technology and Applications* 2. ed., reprinted. 0-470-85445-6 (Wiley & Sons, Ltd., Chichester, 2004).

[58] Baker, R. W., Wijmans, J. G. & Huang, Y. Permeability, permeance and selectivity: A preferred way of reporting pervaporation performance data. *Journal of Membrane Science* **348,** 346–352. doi:`10.1016/j.memsci.2009.11.022` (2010).

[59] Chapman, S. & Cowling, T. G. *The mathematical theory of non-uniform gases: An account of the kinetic theory of viscosity, thermal conduction and diffusion in gases* 2. ed., reprinted (Cambridge Univ. Press, Cambridge, 1953).

[60] Liboff, R. L. *Kinetic Theory: Classical, Quantum, and Relativistic Descriptions* 3rd ed. 0387955518 (Springer, New York, 2003).

[61] Demtröder, W. *Experimentalphysik 1: Mechanik und Wärme* 5., neu bearb. und aktualisierte Aufl. 978-3-540-79294-9. doi:`10.1007/978-3-540-79295-6` (Springer-Verlag, Berlin, 2008).

[62] Luis, P. in *Fundamental Modeling of Membrane Systems* (ed Luis, P.) 1–23 (Elsevier, Amsterdam, Netherlands, 2018). 978-0-12-813483-2.

[63] Van der Bruggen, B. in *Fundamental Modeling of Membrane Systems* (ed Luis, P.) 25–70 (Elsevier, Amsterdam, Netherlands, 2018). 978-0-12-813483-2.

[64] Morita, S. in *Noncontact Atomic Force Microscopy* (eds Morita, S., Wiesendanger, R. & Meyer, E.) 1–10 (Springer, Berlin and Heidelberg, 2002). 978-3-642-62772-9.

[65] Haugstad, G. *Atomic force microscopy: Exploring basic modes and advanced applications* 9781118360699. doi:`10.1002/9781118360668` (John Wiley & Sons, Hoboken, N.J, 2012).

[66] Ricci, D. & Braga, P. C. in *Atomic force microscopy* (eds Braga, P. C. & Ricci, D.) 3–12 (Humana Press, Totowa N.J., 2004). 1588290948.

[67] Meyer, E., Hug, H. J. & Bennewitz, R. *Scanning Probe Microscopy: The Lab on a Tip* 978-3-662-09801-1. doi:`10.1007/978-3-662-09801-1` (Springer Berlin Heidelberg, Berlin, Heidelberg, 2004).

[68] Ricci, D. & Braga, P. C. in *Atomic force microscopy* (eds Braga, P. C. & Ricci, D.) 13–24 (Humana Press, Totowa N.J., 2004). 1588290948.

[69] Vlassak, J. J. & Nix, W. D. A new bulge test technique for the determination of Young's modulus and Poisson's ratio of thin films. *Journal of Materials Research* **7,** 3242–3249. doi:`10.1557/JMR.1992.3242` (1992).

[70] Zhang, X. *Mechanical Charcterization of Carbon Nanosheets* PhD thesis (Bielefeld University, Bielefeld, 2010). `https://pub.uni-bielefeld.de/record/2305751`.

[71] Nečas, D. & Klapetek, P. *Gwyddion: An SPM data visualization and analysis tool* version 2.55. Czech Metrology Institue, Nov. 4, 2019. `http://gwyddion.net/`.

[72] Lakowicz, J. R. *Principles of fluorescence spectroscopy* 3rd ed. 0387312781 (Springer, New York, 2006).

[73] Paddock, S. W. & Eliceiri, K. W. in *Confocal microscopy* (ed Paddock, S. W.) 9–47 (Humana Press, New York, 2014). 978-1-58829-351-0.

[74] Steiner, G. in *Handbook of spectroscopy* (eds Gauglitz, G. & Vo-Dinh, T.) 70–88 (Wiley-VCH, Weinheim, 2005). 978-3-527-29782-0.

[75] Butt, H.-J., Graf, K. & Kappl, M. *Physics and chemistry of interfaces* 1. ed. 3527404139. doi:`10.1002/3527602313` (Wiley-VCH, Weinheim, 2003).

[76] Thies, S. *Benetzbarkeit und Oberflächenenergie von aromatischen SAMs und CNMs* Bachelor thesis (Bielefeld University, Bielefeld, 2015).

[77] Rasband, W. *Image Processing and Analysis in Java* version 1.52a. National Institues of Health. `https://imagej.nih.gov/ij/`.

[78] Brugnara, M. *Contact Angle* `https://imagej.nih.gov/ij/plugins/contact-angle.html`.

[79] Tremblay, P., Savard, M., Vermette, J. & Paquin, R. Gas permeability, diffusivity and solubility of nitrogen, helium, methane, carbon dioxide and formaldehyde in dense polymeric membranes using a new on-line permeation apparatus. *Journal of Membrane Science* **282,** 245–256. doi:`10.1016/j.memsci.2006.05.030` (2006).

[80] Firpo, G., Repetto, L., Buatier de Mongeot, F. & Valbusa, U. Focused-ion beam fabrication of nanometer orifices for leak detection. *Journal of Vacuum Science & Technology B: Microelectronics and Nanometer Structures* **27,** 2347. doi:`10.1116/1.3243229` (2009).

[81] Firpo, G., Angeli, E., Repetto, L. & Valbusa, U. Permeability thickness dependence of polydimethylsiloxane (PDMS) membranes. *Journal of Membrane Science* **481,** 1–8. doi:`10.1016/j.memsci.2014.12.043` (2015).

[82] Suits, L. D. in *Geosynthetics in civil engineering* (ed Sarsby, R. W.) 66–93 (Woodhead Pub, Cambridge, England and Boca Raton, 2007). 9781855736078. doi:`10.1533/9781845692490.1.66`.

[83] *ASTM E96 / E96M-16. Standard Test Methods for Water Vapor Transmission of Materials* West Conshohocken, PA: ASTM International, 2016. doi:`10.1520/E0096_E0096M-16`. `www.astm.org`.

[84] Lenz, S. Bielefeld University: Mechanical Workshop, 2019.

[85] Allan H. Harvey. in *CRC Handbook of Chemistry and Physics* (ed Haynes, W. M.) 6–9 (CRC Press, Boca Raton, London, and New York, 2017). 978-1-4987-5429-3.

[86] Eric W. Lemmon. in *CRC Handbook of Chemistry and Physics* (ed Haynes, W. M.) 6-5–6-6 (CRC Press, Boca Raton, London, and New York, 2017). 978-1-4987-5429-3.

[87] Ward, B. W., Notte, J. A. & Economou, N. P. Helium ion microscope: A new tool for nanoscale microscopy and metrology. *Journal of Vacuum Science & Technology B: Microelectronics and Nanometer Structures* **24,** 2871. doi:`10.1116/1.2357967` (2006).

[88] Hill, R. & Faridur Rahman, F. Advances in helium ion microscopy. *Nuclear Instruments and Methods in Physics Research Section A: Accelerators, Spectrometers, Detectors and Associated Equipment* **645,** 96–101. doi:`10.1016/j.nima.2010.12.123` (2011).

[89] Notte, J., Hill, R., McVey, S. M., Ramachandra, R., Griffin, B. & Joy, D. Diffraction imaging in a He+ ion beam scanning transmission microscope. *Microscopy and Microanalysis* **16,** 599–603. doi:`10.1017/S1431927610093682` (2010).

[90] Hall, A. R. In situ thickness assessment during ion milling of a free-standing membrane using transmission helium ion microscopy. *Microscopy and Microanalysis* **19,** 740–744. doi:`10.1017/S1431927613000500` (2013).

[91] Hill, R., Notte, J. & Ward, B. The ALIS He ion source and its application to high resolution microscopy. *Physics Procedia* **1,** 135–141. doi:`10.1016/j.phpro.2008.07.088` (2008).

[92] *Helium Ion Microscopy* (eds Hlawacek, G. & Gölzhäuser, A.) 9783319419886. doi:`10.1007/978-3-319-41990-9` (Springer International Publishing, Cham and s.l., 2016).

[93] Wiseman, T., Williston, S., Brandts, J. F. & Lin, L.-N. Rapid measurement of binding constants and heats of binding using a new titration calorimeter. *Analytical Biochemistry* **179,** 131–137. doi:`10.1016/0003-2697(89)90213-3` (1989).

[94] Pierce, M. M., Raman, C. S. & Nall, B. T. Isothermal titration calorimetry of protein-protein interactions. *Methods* **19,** 213–221. doi:`10.1006/meth.1999.0852` (1999).

[95] Kobayashi, Y. & Maudsley, D. V. *Biological applications of liquid scintillation counting* 0-12-417250-4 (Acad. Press, New York, NY, 1974).

[96] Neame, K. D. & Homewood, C. A. *Introduction to liquid scintillation counting* 0408706376 (Butterworth, London, 1974).

[97] Zerbe, O. & Jurt, S. *Applied NMR spectroscopy for chemists and life scientists* 9783527677856 (Wiley-VCH, Weinheim, Germany, 2014).

[98] Friebolin, H. *Basic one- and two-dimensional NMR spectroscopy* 5., completely revised and enlarged edition. 978-3-527-32782-9 (Wiley-VCH, Weinheim, 2011).

[99] Günther, H. *NMR Spectroscopy: Basic Principles, Concepts and Applications in Chemistry* 3rd, completely revised and updated edition. 978-3-527-33004-1 (Wiley-VCH Verlag GmbH & Co. KGaA, Weinheim, 2013).

[100] Haynes, R. *Optical Microscopy of Materials* 978-1-4757-6085-9. doi:`10.1007/978-1-4757-6085-9` (Springer, Boston, MA, 1984).

[101] Wang, G. & Fang, N. Detecting and tracking nonfluorescent nanoparticle probes in live cells. *Methods in enzymology* **504,** 83–108. doi:`10.1016/B978-0-12-391857-4.00004-5` (2012).

[102] Pluta, M. Nomarski's DIC microscopy: a review. *Proceedings of the Society of Photo-Optical Instrumentation Engineers* **1846,** 10–25. doi:`10.1117/12.171873` (1994).

[103] Nakanishi, K. *Infrared Absorption Spectroscopy. -Practical-* (Holden-Day Incorporated, Nankodo Company Limited, San Francisco, Tokyo, 1962).

[104] Wartewig, S. *IR and Raman spectroscopy: Fundamental processing* 3-527-30245-X. doi:`10.1002/3527601635` (Wiley-VCH, Weinheim, 2003).

[105] Hoffmann, F. Infrared reflection-absorption spectroscopy of adsorbed molecules. *Surface Science Reports* **3,** 107. doi:`10.1016/0167-5729(83)90001-8` (1983).

[106] Ryberg, R. Oxidation of Methanol on Cu(100) Studied by Infrared Spectroscopy. *Physical Review Letters* **49,** 1579–1582. doi:`10.1103/PhysRevLett.49.1579` (1982).

[107] Bates, J. B. Fourier transform infrared spectroscopy. *Science* **191,** 31–37. doi:`10.1126/science.1246596` (1976).

[108] Jaggi, N. & Vij, D. R. in *Handbook of Applied Solid State Spectroscopy* (ed Vij, D. R.) 411–450 (Springer US, Boston, MA, 2006). 0387324976. doi:`10.1007/0-387-37590-2_9`.

[109] Jasperson, S. N. & Schnatterly, S. E. An Improved Method for High Reflectivity Ellipsometry Based on a New Polarization Modulation Technique. *Review of Scientific Instruments* **40,** 761–767. doi:`10.1063/1.1684062` (1969).

[110] Neckel, A. In situ-Untersuchungen der Grenzfläche Festkörper/Lösung. *Fresenius' Zeitschrift für Analytische Chemie* **319,** 682–694. doi:`10.1007/BF01226750` (1984).

[111] Greenler, R. G. Infrared Study of Adsorbed Molecules on Metal Surfaces by Reflection Techniques. *The Journal of Chemical Physics* **44,** 310–315. doi:`10.1063/1.1726462` (1966).

[112] *PMA50 User's Manual* version Version 1.01. Bruker.

[113] *PEM-90^{TM}Photoelastic Modulator Systems User Manual* Hinds Instruments.

[114] *Optics User Software (OPUS)* version 5.5. Bruker Optik GmbH, Apr. 11, 2005.

[115] Gray, P. & Waddington, T. C. Fundamental vibration frequencies and force constants in the azide ion. *Transactions of the Faraday Society* **53,** 901. doi:`10.1039/TF9575300901` (1957).

[116] Lieber, E., Rao, C. N. R., Chao, T. S. & Hoffman, C. W. W. Infrared Spectra of Organic Azides. *Analytical Chemistry* **29,** 916–918. doi:`10.1021/ac60126a016` (1957).

[117] Bertilsson, L. & Liedberg, B. Infrared Study of Thiol Monolayer Assemblies on Gold: Preparation, Characterization, and Functionalization of Mixed Monolayers. *Langmuir* **9,** 141–149. doi:`10.1021/la00025a032` (1993).

[118] Lapin, N. A. & Chabal, Y. J. Infrared characterization of biotinylated silicon oxide surfaces, surface stability, and specific attachment of streptavidin. *The journal of physical chemistry. B* **113,** 8776–8783. doi:`10.1021/jp809096m` (2009).

[119] Schnieders, A., Meyerbröker, N., Vater, A., Maasch, C. & Bethge, D. L. WO 2018/220173 A9. `https://worldwide.espacenet.com/patent/search/family/059506323/publication/WO2018220173A1?q=WO%202018%2F220173%20A9`(2018).

[120] Reimer, L. *Scanning Electron Microscopy: Physics of Image Formation and Microanalysis* 978-3-662-13562-4 (Springer Berlin Heidelberg, Berlin, Heidelberg and s.l., 1985).

[121] Reimer, L. *Transmission Electron Microscopy: Physics of Image Formation and Microanalysis* Second Edition. 9783662215791 (Springer Berlin Heidelberg, Berlin, Heidelberg and s.l., 1989).

[122] *Gatan Microscopy Suite: DigitalMicrograph®* version 3.32.2403.0. Gatan. `https://www.gatan.com/installation-instructions`.

[123] Kimball, S. & Mattis, P. *GNU Image Manipulation Program (GIMP)* version 2.10.14. `https://www.gimp.org/`.

[124] Skoog, D. A. & Leary, J. J. *Instrumentelle Analytik: Grundlagen - Geräte - Anwendungen* 978-3-662-07917-1 (Springer, Berlin and Heidelberg, 1996).

[125] Green, J. in *Handbook of Spectroscopy* (eds Gauglitz, G. & Vo-Dinh, T.) 279–296 (Wiley-VCH, Weinheim, 2005). 978-3-527-29782-0.

[126] Briggs, D. & Grant, J. T. in *Surface analysis by Auger and X-ray photoelectron spectroscopy* (eds Briggs, D. & Grant, J. T.) 1–30 (IM Publ, Chichester, 2003). 1-901019-04-7.

[127] Briggs, D. in *Surface analysis by Auger and X-ray photoelectron spectroscopy* (eds Briggs, D. & Grant, J. T.) 31–56 (IM Publ, Chichester, 2003). 1-901019-04-7.

[128] Tanuma, S. in *Surface analysis by Auger and X-ray photoelectron spectroscopy* (eds Briggs, D. & Grant, J. T.) 259–294 (IM Publ, Chichester, 2003). 1-901019-04-7.

[129] Kövér, L. in *Surface analysis by Auger and X-ray photoelectron spectroscopy* (eds Briggs, D. & Grant, J. T.) 421–464 (IM Publ, Chichester, 2003). 1-901019-04-7.

[130] Hertz, H. Ueber einen Einfluss des ultravioletten Lichtes auf die electrische Entladung. *Annalen der Physik* **267,** 983–1000. doi:`10.1002/andp.18872670827` (1887).

[131] Einstein, A. Über einen die Erzeugung und Verwandlung des Lichtes betreffenden heuristischen Gesichtspunkt. *Annalen der Physik* **322,** 132–148. doi:`10.1002/andp.19053220607` (1905).

[132] Seah, M. P. A review of the analysis of surfaces and thin films by AES and XPS. *Vacuum* **34,** 463–478. doi:`10.1016/0042-207X(84)90084-8` (1984).

[133] Andrade, J. D. in *Surface and Interfacial Aspects of Biomedical Polymers* (ed Andrade, J. D.) 105–195 (Springer US, Boston, MA, 1985). 978-1-4684-8612-4.

[134] Lindgren, I. Chemical shifts in X-ray and photo-electron spectroscopy: a historical review. *Journal of Electron Spectroscopy and Related Phenomena* **137-140,** 59–71. doi:`10.1016/j.elspec.2004.02.086` (2004).

[135] Taucher, T. C., Hehn, I., Hofmann, O. T., Zharnikov, M. & Zojer, E. Understanding Chemical versus Electrostatic Shifts in X-ray Photoelectron Spectra of Organic Self-Assembled Monolayers. *The Journal of Physical Chemistry C* **120,** 3428–3437. doi:`10.1021/acs.jpcc.5b12387` (2016).

[136] Tanuma, S., Powell, C. J. & Penn, D. R. Calculations of electorn inelastic mean free paths. II. Data for 27 elements over the 50-2000 eV range. *Surface and Interface Analysis* **17,** 911–926. doi:`10.1002/sia.740171304` (1991).

[137] Tanuma, S., Powell, C. J. & Penn, D. R. Calculations of electron inelastic mean free paths. III. Data for 15 inorganic compounds over the 50-2000 eV range. *Surface and Interface Analysis* **17,** 927–939. doi:`10.1002/sia.740171305` (1991).

[138] Tanuma, S., Powell, C. J. & Penn, D. R. Calculations of electron inelastic mean free paths (IMFPS). IV. Evaluation of calculated IMFPs and of the predictive IMFP formula TPP-2 for electron energies between 50 and 2000 eV. *Surface and Interface Analysis* **20,** 77–89. doi:`10.1002/sia.740200112` (1993).

[139] Tanuma, S., Powell, C. J. & Penn, D. R. Calculations of electron inelastic mean free paths. V. Data for 14 organic compounds over the 50-2000 eV range. *Surface and Interface Analysis* **21,** 165–176. doi:`10.1002/sia.740210302` (1994).

[140] Seah, M. P. & Dench, W. A. Quantitative electron spectroscopy of surfaces: A standard data base for electron inelastic mean free paths in solids. *Surface and Interface Analysis* **1,** 2–11. doi:`10.1002/sia.740010103` (1979).

[141] Bain, C. D. & Whitesides, G. M. Attenuation lengths of photoelectrons in hydrocarbon films. *The Journal of Physical Chemistry* **93,** 1670–1673. doi:`10.1021/j100341a095` (1989).

[142] *CasaXPS: Processing Software for XPS, AES, SIMS and More* version 2.3.22PR1.0. Casa Software Limited. `http://www.casaxps.com/`.

[143] Cheng, F., Gamble, L. J. & Castner, D. G. XPS, TOF-SIMS, NEXAFS, and SPR characterization of nitrilotriacetic acid-terminated self-assembled monolayers for controllable immobilization of proteins. *Analytical chemistry* **80,** 2564–2573. doi:`10.1021/ac702380w` (2008).

[144] Eck, W., Stadler, V., Geyer, W., Zharnikov, M., Gölzhäuser, A. & Grunze, M. Generation of Surface Amino Groups on Aromatic Self-Assembled Monolayers by Low Energy Electron Beams—A First Step Towards Chemical

Lithography. *Advanced Materials* **12,** 805–808. doi:`10.1002/(SICI)1521-4095(200006)12:11<C805::AID-ADMA805>3.0.CO;2-0` (2000).

[145] Graf, N., Yegen, E., Gross, T., Lippitz, A., Weigel, W., Krakert, S., Terfort, A. & Unger, W. E. XPS and NEXAFS studies of aliphatic and aromatic amine species on functionalized surfaces. *Surface Science* **603,** 2849–2860. doi:`10.1016/j.susc.2009.07.029` (2009).

[146] Hamoudi, H., Chesneau, F., Patze, C. & Zharnikov, M. Chain-Length-Dependent Branching of Irradiation-Induced Processes in Alkanethiolate Self-Assembled Monolayers. *The Journal of Physical Chemistry C* **115,** 534–541. doi:`10.1021/jp109434k` (2011).

[147] Yan, R., Le Pleux, L., Mayor, M. & Zharnikov, M. Promoted Exchange Reaction between Alkanethiolate Self-Assembled Monolayers and an Azide-Bearing Substituent. *The Journal of Physical Chemistry C* **120,** 25967–25976. doi:`10.1021/acs.jpcc.6b09565` (2016).

[148] Tim Nunney. *XPS Characterization of 'Click' Surface Chemistry: Application Note: 52130* 2015. `https://www.thermofisher.com/content/dam/tfs/ATG/CAD/CAD%20Documents/Application%20&%20Technical%20Notes/Surface%20Analysis/AN52130_E%200411M_H_1.pdf` (2020).

[149] *XPS Reference Table of Elements* Thermo Fisher Scientific Inc., © 2013-2020. `https://xpssimplified.com/elements/carbon.php` (2020).

[150] *XPS Reference Table of Elements* Thermo Fisher Scientific Inc., © 2013-2020. `https://xpssimplified.com/elements/nitrogen.php` (2020).

[151] *XPS Reference Table of Elements* Thermo Fisher Scientific Inc., © 2013-2020. `https://xpssimplified.com/elements/oxygen.php` (2020).

[152] *XPS Reference Table of Elements* Thermo Fisher Scientific Inc., © 2013-2020. `https://xpssimplified.com/elements/fluorine.php` (2020).

[153] *XPS Reference Table of Elements* Thermo Fisher Scientific Inc., © 2013-2020. `https://xpssimplified.com/elements/sulfur.php` (2020).

[154] Amin, I., Steenackers, M., Zhang, N., Schubel, R., Beyer, A., Gölzhäuser, A. & Jordan, R. Patterned polymer carpets. *Small (Weinheim an der Bergstrasse, Germany)* **7,** 683–687. doi:`10.1002/smll.201001658` (2011).

[155] Biebricher, A., Paul, A., Tinnefeld, P., Gölzhäuser, A. & Sauer, M. Controlled three-dimensional immobilization of biomolecules on chemically patterned surfaces. *Journal of biotechnology* **112,** 97–107. doi:`10.1016/j.jbiotec.2004.03.019` (2004).

[156] *2YE0: X-ray Structure of the Cyan Fluorescent Protein mTurquoise (K206A Mutant). 3AKO: Crystal Structure of the Reassembled Venus* RCSB PDB Protein Data Bank. `https://www.rcsb.org/` (2018).

[157] Kotagiri, N., Li, Z., Xu, X., Mondal, S., Nehorai, A. & Achilefu, S. Antibody quantum dot conjugates developed via copper-free click chemistry for rapid analysis of biological samples using a microfluidic microsphere array system. *Bioconjugate chemistry* **25,** 1272–1281. doi:`10.1021/bc500139u` (2014).

[158] Click Chemistry Tools. *2019/20 Catalog & Reference Manual* (ed Click Chemistry Tools, 8341 E. Gelding Drive, Scottsdale, AZ 85260) 2019. `https://clickchemistrytools.com/wp-content/uploads/2018/11/Click-Chemistry-Toolbox.pdf`.

[159] *Chem3D Professional* version 16.0.1.4. PerkinElmer Informatics Incorporated. `https://www.perkinelmer.com/de/product/chemoffice-professional-chemofficepro`.

[160] Chinaryan, V. *Gas permeation of carbon nanomembranes* PhD Thesis (Bielefeld University, Bielefeld, 2017). `https://pub.uni-bielefeld.de/record/2914121`.

[161] Silberstein, E. B., Elgazzar, A. H. & Kapilivsky, A. Phosphorus-32 radiopharmaceuticals for the treatment of painful osseous metastases. *Seminars in Nuclear Medicine* **22,** 17–27. doi:`10.1016/S0001-2998(05)80153-9` (1992).

[162] Harald Kalka. *Table of Diffusion Coefficients* PHREEQC (Version 3) – A Computer Program for Speciation, Batch-Reaction, One-Dimensional Transport, and Inverse Geochemical Calculations. The Diffusion Coefficients are taken from the Thermodynamic Database "phreeqc.dat". 2015-12-30. `https://www.aqion.de/site/194` (2020).

[163] Tang, A. & Sandall, O. C. Diffusion Coefficient of Chlorine in Water at 25-60 °C. *Journal of Chemical & Engineering Data* **30,** 189–191. doi:`10.1021/je00040a017` (1985).

[164] Wang, J. H. Self-Diffusion Coefficients of Water. *The Journal of Physical Chemistry* **69,** 4412. doi:`10.1021/j100782a510` (1965).

[165] Woolf, L. A. Tracer Diffusion of Tritiated Water (THO) in Ordinary Water (H2O) under Pressure. *Journal of the Chemical Society, Faraday Transactions 1: Physical Chemistry in Condensed Phases* **71,** 784. doi:`10.1039/F19757100784` (1975).

[166] Svishchev, I. M. & Kusalik, P. G. Dynamics in Liquid Water, Water-D2, and Water-T2: A Comparative Simulation Study. *The Journal of Physical Chemistry* **98,** 728–733. doi:`10.1021/j100054a002` (1994).

[167] Dellago, C. & Hummer, G. Kinetics and Mechanism of Proton Transport across Membrane Nanopores. *Physical review letters* **97,** 245901. doi:`10.1103/PhysRevLett.97.245901` (2006).

[168] De Groot, B. L., Frigato, T., Helms, V. & Grubmüller, H. The Mechanism of Proton Exclusion in the Aquaporin-1 Water Channel. *Journal of molecular biology* **333,** 279–293. doi:`10.1016/j.jmb.2003.08.003` (2003).

[169] Burykin, A. & Warshel, A. What Really Prevents Proton Transport through Aquaporin? Charge Self-Energy versus Proton Wire Proposals. *Biophysical Journal* **85,** 3696–3706. doi:`10.1016/S0006-3495(03)74786-9` (2003).

[170] Gutknecht, J., Bisson, M. A. & Tosteson, F. C. Diffusion of Carbon Dioxide through Lipid Bilayer Membranes: Effects of Carbonic Anhydrase, Bicarbonate, and Unstirred Layers. *The Journal of general physiology* **69,** 779–794. doi:`10.1085/jgp.69.6.779` (1977).

[171] Zharnikov, M., Geyer, W., Gölzhäuser, A., Frey, S. & Grunze, M. Modification of alkanethiolate monolayers on Au-substrate by low energy electron irradiation: Alkyl chains and the S/Au interface. *Physical Chemistry Chemical Physics* **1,** 3163–3171. doi:`10.1039/A902013F` (1999).

[172] Li, S., Eghiaian, F., Sieben, C., Herrmann, A. & Schaap, I. A. T. Bending and puncturing the influenza lipid envelope. *Biophysical Journal* **100,** 637–645. doi:`10.1016/j.bpj.2010.12.3701` (2011).

[173] Delorme, N. & Fery, A. Direct method to study membrane rigidity of small vesicles based on atomic force microscope force spectroscopy. *Physical review. E, Statistical, nonlinear, and soft matter physics* **74,** 030901. doi:`10.1103/PhysRevE.74.030901` (2006).

[174] Carrasco, C., Carreira, A., Schaap, I. A. T., Serena, P. A., Gómez-Herrero, J., Mateu, M. G. & de Pablo, P. J. DNA-mediated anisotropic mechanical reinforcement of a virus. *Proceedings of the National Academy of Sciences of the United States of America* **103,** 13706–13711. doi:`10.1073/pnas.0601881103` (2006).

[175] Ivanovska, I. L., de Pablo, P. J., Ibarra, B., Sgalari, G., MacKintosh, F. C., Carrascosa, J. L., Schmidt, C. F. & Wuite, G. J. L. Bacteriophage capsids: tough nanoshells with complex elastic properties. *Proceedings of the National Academy of Sciences of the United States of America* **101,** 7600–7605. doi:`10.1073/pnas.0308198101` (2004).

[176] Ivanovska, I., Wuite, G., Jönsson, B. & Evilevitch, A. Internal DNA pressure modifies stability of WT phage. *Proceedings of the National Academy of*

Sciences of the United States of America **104,** 9603–9608. doi:`10.1073/pnas.0703166104` (2007).

[177] Michel, J. P., Ivanovska, I. L., Gibbons, M. M., Klug, W. S., Knobler, C. M., Wuite, G. J. L. & Schmidt, C. F. Nanoindentation studies of full and empty viral capsids and the effects of capsid protein mutations on elasticity and strength. *Proceedings of the National Academy of Sciences of the United States of America* **103,** 6184–6189. doi:`10.1073/pnas.0601744103` (2006).

[178] Roos, W. H., Radtke, K., Kniesmeijer, E., Geertsema, H., Sodeik, B. & Wuite, G. J. L. Scaffold expulsion and genome packaging trigger stabilization of herpes simplex virus capsids. *Proceedings of the National Academy of Sciences of the United States of America* **106,** 9673–9678. doi:`10.1073/pnas.0901514106` (2009).

[179] Uetrecht, C., Versluis, C., Watts, N. R., Roos, W. H., Wuite, G. J. L., Wingfield, P. T., Steven, A. C. & Heck, A. J. R. High-resolution mass spectrometry of viral assemblies: molecular composition and stability of dimorphic hepatitis B virus capsids. *Proceedings of the National Academy of Sciences of the United States of America* **105,** 9216–9220. doi:`10.1073/pnas.0800406105` (2008).

[180] Zhao, Y., Ge, Z. & Fang, J. Elastic modulus of viral nanotubes. *Physical review. E, Statistical, nonlinear, and soft matter physics* **78,** 031914. doi:`10.1103/PhysRevE.78.031914` (2008).

[181] Bertolazzi, S., Brivio, J. & Kis, A. Stretching and breaking of ultrathin MoS2. *ACS nano* **5,** 9703–9709. doi:`10.1021/nn203879f` (2011).

[182] Falin, A., Cai, Q., Santos, E. J. G., Scullion, D., Qian, D., *et al.* Mechanical properties of atomically thin boron nitride and the role of interlayer interactions. *Nature communications* **8,** 15815. doi:`10.1038/ncomms15815` (2017).

[183] Lee, C., Wei, X., Kysar, J. W. & Hone, J. Measurement of the elastic properties and intrinsic strength of monolayer graphene. *Science (New York, N.Y.)* **321,** 385–388. doi:`10.1126/science.1157996` (2008).

[184] Schoenenberger, C., Jorritsma, J., Sondag-Huethorst, J. A. M. & Fokkink, L. G. J. Domain Structure of Self-Assembled Alkanethiol Monolayers on Gold. *The Journal of Physical Chemistry* **99,** 3259–3271. doi:`10.1021/j100010a042` (1995).

[185] Poirier, G. E. Characterization of Organosulfur Molecular Monolayers on Au(111) using Scanning Tunneling Microscopy. *Chemical reviews* **97,** 1117–1128. doi:`10.1021/cr960074m` (1997).

[186] Bashir, A., Azzam, W., Rohwerder, M. & Terfort, A. Polymorphism in self-assembled terphenylthiolate monolayers on Au(111). *Langmuir : the ACS journal of surfaces and colloids* **29,** 13449–13456. doi:`10.1021/la403116r` (2013).

[187] Vaish, A., Vanderah, D. J., Richter, L. J., Dimitriou, M., Steffens, K. L. & Walker, M. L. Dithiol-based modification of poly(dopamine): enabling protein resistance via short-chain ethylene oxide oligomers. *Chemical communications (Cambridge, England)* **51,** 6591–6594. doi:`10.1039/c5cc00299k` (2015).

[188] Ballav, N. & Zharnikov, M. Reorientation-promoted Exchange Reaction in Aromatic Self-assembled Monolayers. *The Journal of Physical Chemistry C* **112,** 15037–15044. doi:`10.1021/jp8047357` (2008).

[189] Ballav, N., Terfort, A. & Zharnikov, M. Fabrication of mixed self-assembled monolayers designed for avidin immobilization by irradiation promoted exchange reaction. *Langmuir : the ACS journal of surfaces and colloids* **25,** 9189–9196. doi:`10.1021/la9007476` (2009).

[190] Khan, M. N. & Zharnikov, M. Irradiation Promoted Exchange Reaction with Disulfide Substituents. *The Journal of Physical Chemistry C* **117,** 14534–14543. doi:`10.1021/jp4006026` (2013).

[191] Radha, B., Esfandiar, A., Wang, F. C., Rooney, A. P., Gopinadhan, K., *et al.* Molecular transport through capillaries made with atomic-scale precision. *Nature* **538,** 222–225. doi:`10.1038/nature19363` (2016).

Declaration of Academic Honesty

I hereby declare that I have independently written the present dissertation and that none other than the quoted literature was used.

Bielefeld, July 20, 2020

Raphael Dalpke

A. Technical Drawings

Detailed technical drawings [84] of the modified container for performing gravimetric analyses. The top part and the bottom part are shown in figure A.1 and figure A.2 respectively. Stainless steel was used for the fabrication.

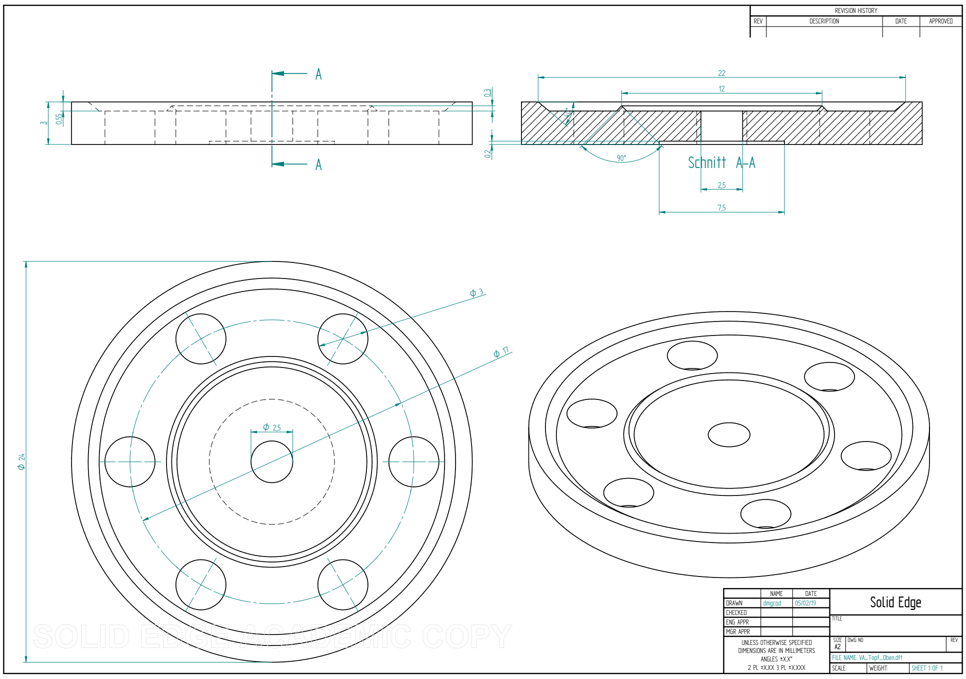

Figure A.1.: Detailed technical drawing [84] of the top part of the modified container design for performing mass loss experiments.

The copper or Teflon sealings have an inner diameter of $d_{in} \sim 10$ mm, an outer diameter of $d_{out} \sim 14$ mm with a thickness of $t \sim 1$ mm. Shortened M6 screws are used with a total length of $t \sim 9$ mm.

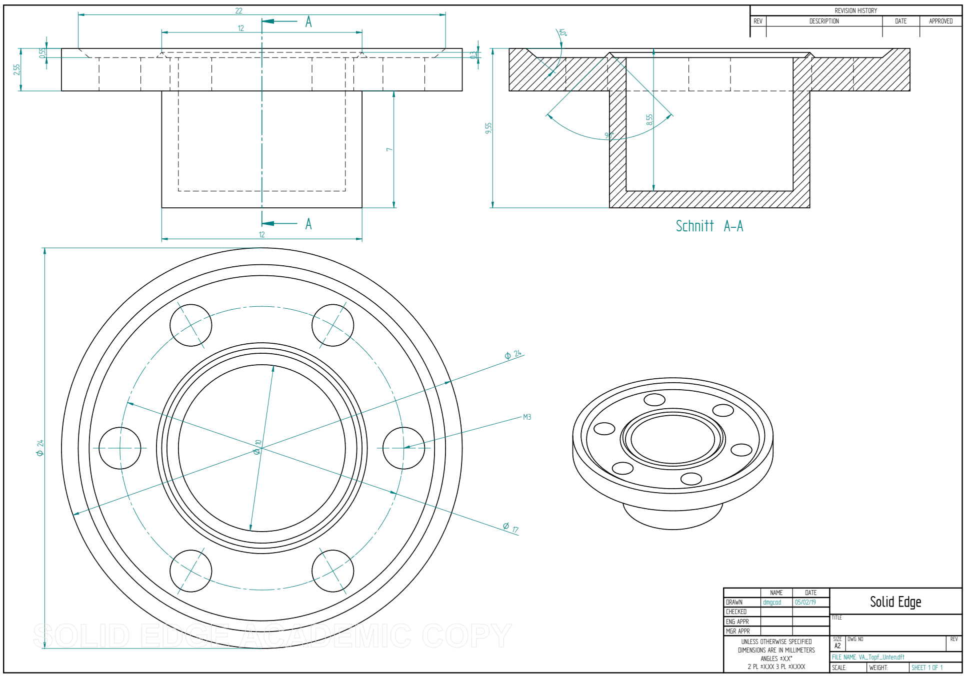

Figure A.2.: Detailed technical drawing [84] of the bottom part of the modified container design for performing mass loss experiments.

B. Preparation and Functionalization of CNMs

Complex Formation with L-Lysine-NTA. An Au(100 nm)Ti(5 nm)Si composite (Georg Albert PVD-Coatings) was used as a substrate. Surface cleaning was done by the treatment with ozone for six minutes at a oxygen (UN 1072, hydrocarbon-free, Linde AG) flow of 1.0 slm (standard liter per minute) employing the ozone cleaner UVOH 150 LAB (FHR Anlagenbau GmbH) and the subsequent immersion into ethanol (absolute, AnalaR NORMAPUR, VWR Chemicals) for at least thirty minutes. The substrate was rinsed with ethanol and blown dry using nitrogen (UN 1066, Linde AG). Piranha solution was freshly prepared from sulfuric acid (95 %, VWR Chemicals) and hydrogen peroxide (30 %, VWR Chemicals) in a schlenk flask using a volume ratio of 3:1 acid:peroxide and letting it rest for at least thirty minutes. Afterwards the flask was thoroughly washed with Millipore water (Super-Q$^{\mathrm{TM}}$ 4, Merck Millipore) and dried in a Memmert universal oven, model UNB 100. Air and residual water were removed from the baked schlenk flask by applying at least three vacuum nitrogen degassing cycles utilizing a heat gun (type 3484, Steinel) and a schlenk line equipped with a chemistry hybrid pump (model RC 6, combination of a two-stage rotary vane pump and a chemistry membrane pump) of Vacuubrand GmbH+Co KG.

The gold substrate was placed under a nitrogen flow into the schlenk flask and two additional degassing cycles were performed. Anhydrous *N*-*N*-dimethylformamide (DMF, 99.8 %, Sigma Aldrich) dried over a molecular sieve (beads, 4-8 mesh, 3 Å, $K_nNa_{12-n}[(AlO_2)_{12}(SiO_2)_{12}]\cdot xH_2O$, Sigma Aldrich) was pipetted under a nitrogen flow to the substrate and the solvent was degassed without the usage of the heat gun. A small amount of 4'-nitro-1,1'-biphenyl-4-thiol (NBPT, Taros Chemicals GmbH & Co. KG) was added under a nitrogen flow and the solution was degassed once again. The schlenk flask was covered with aluminum foil and allowed to rest for three days. The workup was done by the treatment of the specimen with an ultrasonic bath (T310, Elma) for six minutes in DMF (BioSyn, $\geq$ 99.9 %, Honeywell) and ethanol. Subsequently the SAM was rinsed with ethanol and blown dry in a nitrogen stream.

The irradiation with low energy electrons (100 eV, 50 $\mathrm{mC\,cm^{-2}}$) employing an FG 15/40 electron gun (SPECS Surface Nano Analysis GmbH) converted the SAM into a CNM.

For the first functionalization step 3-(maleimido)propionic acid *N*-hydroxysuccinimide ester (MI, $\geq$ 98.5 %, Sigma Aldrich) was taken from the freezer compartment and allowed to reach room temperature. It is important to note that molecules which were ordered close to the day of the functionalization need to be used due to the hydrolysis of the ester bond. A 20 mM solution in anhydrous DMF was prepared with the aid of an ultrasonic bath. A glass slide was cleaned with acetone ($\geq$ 99.8 %, Fisher Scientific), ethyl acetate ($\geq$ 99.8 %, Fisher Scientific) and ethanol. The CNM and the glass slide were blown dry with nitrogen. Two drops of the solution containing MI were placed on the surface of the CNM and covered with the glass slide avoiding any air bubbles. It was kept in the dark for forty minutes, rinsed with DMF and blown dry with nitrogen.

The second functionalization step involved N-[N_α,N_α-Bis(carboxymethyl)-L-lysine]-12-mercaptododecanamide (L-lysine-NTA, $\geq$ 90.0 %, Sigma Aldrich). The NTA taken from the freezer compartment was brought to room temperature. A 20 mM solution was prepared and applied to the specimen following the same procedure like the first functionalization step. After four hours in the dark, the aluminum foil was removed and the sample was cleaned with DMF and blown dry in a nitrogen stream. Whenever the specimen was not used immediately it had been stored under an argon (UN 1006, Linde AG) inert atmosphere.

Reversible Protein Immobilization. A nitro-terminated SAM on an aluminized polyethylene terephthalate (PET) substrate was used. The respective SAM or amino-terminated CNM was provided by CNM Technologies GmbH. The functionalization strategy is based on a patent [119] of CNM Technologies GmbH and Aptarion Biotech. Two slightly different preparation procedures were carried out. They differ in the used solvent, inert gas, in the application of aluminum foil for the coverage of the reaction mixture and in the storage of the specimens. However, these variations do not affect the reaction itself and were done due to the availability of substances and individual preferences. The differences have no influence on the behavior of the samples so that the comparability is still ensured.

For the spectroscopic analyses the samples were prepared according to the following strategy. The CNM was placed into a schlenk flask equipped with a septum (rubber, EC99.1, Carl Roth GmbH & Co) and three successive vacuum argon degassing cycles were applied with the onetime usage of a heat gun. The system was evacuated over night. Tetrahydrofuran (THF, $\geq$ 99.5 %, dried over sodium hydroxide, Carl Roth GmbH & Co) was pipetted under an argon flow into the flask, which was then immersed into a water/ice mixture. *N*-*N*-diisopropylethylamine (DIPEA, $\geq$ 99 %, Sigma Aldrich) was added under an argon stream to the solution. The mediator 2-azidoacetyl chloride (2-AAC, 97 %, 30 % solution in diethyl ether, SelectLab Chemicals GmbH) taken from the refrigerator was brought to room temperature and slowly dripped under argon into the schlenk flask. The volume ratio was $\sim$ 16:1:3 in relation to the components THF:DIPEA:2-AAC. A balloon filled with argon was connected to the flask and the reaction mixture was allowed to rest over night. The solution was carefully quenched with ethanol. The sample was rinsed with ethanol and 2-propanol (AnalaR NORMAPUR, VWR Chemicals) and blown dry with nitrogen. The sulfo-dibenzylcyclooctyne-biotin conjugate (SDBCOB, > 90 % HPLC, Jena Bioscience GmbH) was taken from the freezer compartment and allowed to reach room temperature. A 2 M sodium chloride (analytical reagent grade, Fisher Scientific) solution in Millipore water was prepared using an ultrasonic bath. The functionalized CNM was placed over night into a 84 μM solution of SDBCOB in sodium chloride. The specimen was rinsed with Millipore water, dried with a nitrogen stream and stored under an argon inert atmosphere.

The samples used for the fluorescence measurements were fabricated starting with the SAMs provided by CNM Technologies GmbH. The irradiation with low energy electrons was performed through a brass mask which exhibited an array of 3x3 orifices ($\varnothing = 100\,\mu$m, distance between two orifices $d = 50\,\mu$m, thickness $t = 100\,\mu$m). A self-built Teflon holder was treated with an ultrasonic bath for fifteen minutes in ethanol and 2-propanol. The patterned CNMs were plugged into the holder and placed in a schlenk flask, which was equipped with a septum. In figure B.1 a photograph of the arrangement is shown. Degassing cycles were applied as described before utilizing nitrogen as an inert gas.

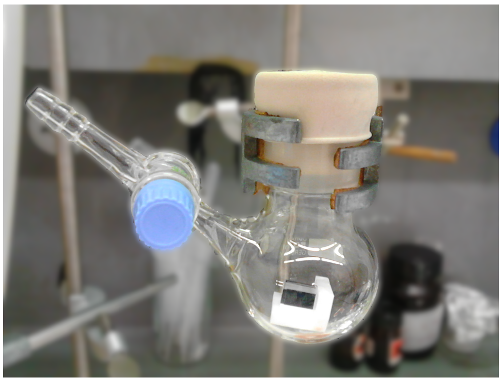

Figure B.1.: Sample arrangement: Patterned CNMs plugged into a self-built Teflon holder and placed into a schlenk flask, which was equipped with a septum.

The subsequent functionalization steps involving 2-AAC and SDBCOB were conducted in the same manner as reported above. Dichloromethane (CH_2Cl_2, anhydrous, $\geq$ 99.8 %, with 50-150 ppm amylene as stabilizing agent, Sigma Aldrich) was used as a solvent for the first step. The volume ratio was $\sim$ 25:1:3 in relation to the components CH_2Cl_2:DIPEA:2-AAC. The amount of solvent was increased due to the dimensions of the Teflon holder. The reaction mixture was covered with aluminum foil. The solution was transferred into a separate beaker after the reaction and quenched. The same procedure was followed for the specimen. For the functionalization with SDBCOB a concentration of at least 84 μM was used and the samples were wrapped in aluminum foil and stored under an argon inert gas atmosphere at a temperature of $T = -22\,°\mathrm{C}$.

Enhanced Coupling Density through Amino-Terminated Self-Assembled-Monolayers. The syntheses and purity analyses of 4'-(aminomethyl)-[1,1'-biphenyl]-4-thiol (AMBPT) and (4'-((methoxymethyl)thio)-[1,1'-biphenyl]-4-yl)methanamine (MOM-AMBPT) were performed by Nicole Wutke at the Max Planck Institute for Polymer Research in Mainz using 4'-mercapto-[1,1'-biphenyl]-4-carbonitril (97 % GC, Sigma Aldrich) as an educt.

A 300 nm gold layer on mica from Georg Albert PVD-Coatings was used as a substrate. The same procedure as reported above was applied for the cleaning of the substrate and the used schlenk flask and for the degassing of the solvent. Instead of using an ultrasonic bath for the cleaning, simple rinsing was applied. Nitrogen was employed as an inert gas and DMF as the solvent. The AMBPT was taken from the freezer compartment and allowed to reach room temperature. At least an $\sim$ 0.5 mM solution in DMF was prepared. The precursor molecule was dissolved in a snap-on lid in advance using a small amount of the solvent. The main part of the DMF was degassed in the schlenk flask. The amount utilized to solve the AMBPT and to rinse the snap-on lid afterwards were only degassed during the subsequent application of one degassing cycle. The reaction mixture was overlayed with an nitrogen atmosphere, covered with aluminum foil and let rest for three days. The specimen was rinsed with DMF and ethanol, blown dry under a nitrogen stream and stored under an argon inert gas atmosphere.

The irradiation with low energy electrons (50 eV, 50 $\mathrm{mC\,cm^{-2}}$) was conducted in the XPS system at a pressure better than $p < 8.0 \cdot 10^{-10}$ mbar.

For the transfer of the resulting CNMs the following method has been used. The specimen was spin-coated with two different photoresists (AR-P 639.04 (PMMA 50K) and AR-P 679.04 (PMMA 950K) in *n*-butyl acetate ethyl lactate, Allresist GmbH) starting with the PMMA 50K. A spin coater (Polos Spin150i, Spincoating, SPS-Europe B.V.) equipped with an oil-less piston vaccum pump (MAJP-140V(L), Micro-Air Engineering PTE LTD) was used as a device. Each spin-coating step was executed at four thousand revolutions per minute for thirty seconds and the sample was heated at $T = 90\,°\mathrm{C}$ for five minutes after each spin-coating step to evaporate the solvent.

The edges of the sample were narrowly cut and transferred on top of an etching solution containing a mass fraction of 1:4:40 in relation to I_2:KI:H_2O for ten minutes. The iodine (resublimed crystals, 99.8 %) and the potassium iodide ($\geq$ 99 %) were purchased from Alfa Aesar and Carl Roth GmbH & Co respectively. Millipore water was used for the solution. The PMMA-stabilized CNM on the gold layer was detached from the mica substrate by carefully dipping the specimen into Millipore water. The floating sample was transferred with a wafer piece (silicon (100) or 300 nm thermal silicon oxide on silicon, Si-Mat Silicon Materials) on top of the etching solution for ten minutes to dissolve the gold layer. Subsequently, the CNM was placed onto a Millipore water surface. After one minute it was transferred onto a 10 wt% solution of potassium iodide in Millipore water and let rest for ten minutes. Two subsequent washing steps of one minute on top of a fresh Millipore water surface were performed. Finally, the floating CNM was fished onto the respective target substrate and allowed to dry. For the HIM analyses quantifoil multi A holey carbon films on TEM grids (Quantifoil Micro Tools GmbH) and for the examination by optical microscopy 300 nm thermal silicon oxide on silicon were utilized as the target support.

The sample used for the investigation by optical microscopy was placed on the bottom of a beaker. Acetone was slowly added and the PMMA was allowed to dissolve for one hour. The specimen was taken out perpendicular to the surface and immersed in the same manner into fresh acetone for three times. Afterwards the CNM was dried in a nitrogen stream. The samples on quantifoil were placed into a TEM grid holder. A critical point dryer (autosamdri-815, Tousimis Research Corporation) filled with acetone and equipped with carbon dioxide (UN 1013, Linde AG) was employed to dissolve the resist.

Irreversible Protein Immobilization. Amino-terminated CNMs on aluminized PET provided by CNM Technologies GmbH were used as for the reversible protein immobilization approach. The schlenk flask was equipped with a septum and three vacuum nitrogen degassing cycles were applied. During that procedure the heat gun was utilized several times to bake the schlenk flask. The system has been evacuated for four hours before the CNM was placed into the schlenk flask and additional three degassing cycles without the usage of the heat gun were applied. It was evacuated over night. The functionalization with the linker 2-AAC was performed like described above utilizing nitrogen as an inert gas and molecular sieve-dried THF and DIPEA. The volume ratio was $\sim$ 17:1:3 in relation to the components THF:DIPEA:2-AAC. During the addition of 2-AAC an extra cannula was stung into the septum to release the evolving gaseous hydrogen chloride. The reaction mixture was overlayed with nitrogen, covered with aluminum foil and allowed to rest for 4.5 hours. Onetime rinsing with Millipore water was conducted as a final step during the workup procedure. For the second functionalization step dibenzocyclooctyne-maleimide (DBCOM, $>$ 88 %, Sigma Aldrich) was taken from the freezer compartment and allowed to reach room temperature. The functionalized CNM was placed into a 0.5 mM solution of DBCOM in dried DMF and covered with aluminum foil. After one day the sample was subsequently rinsed with DMF, ethanol, onetime Millipore water and blown dry in a nitrogen stream. If not stated differently, the specimen were stored under an argon inert gas atmosphere, covered with aluminum foil and at a temperature of $T = -22\,°\mathrm{C}$.

Aqueous Apparent Diffusion Coefficients Determined by Radioactive Tracers. An Au(300 nm) gold layer on mica from Georg Albert PVD-Coatings served as a substrate. The cleaning of the schlenk flask and the substrate followed the reported method described in the paragraph of the "Complex Formation with L-Lysine-NTA". The gold substrate was placed into the schlenk flask and three vaccum nitrogen degassing cycles with onetime usage of the heat gun were applied. The system was evacuated over night. DMF was pipetted under a nitrogen flow to the composite and the solvent was degassed. 1,1',4',1"-Terphenyl-4-thiol (TPT, 97 %, Sigma Aldrich, refined by sublimation before usage) was taken from the freezer compartment and allowed to reach room temperature. A small amount of TPT was added under a nitrogen flow to the solvent and one vacuum nitrogen degassing cycle without the utilization of the heat gun was applied. A balloon filled with argon was connected to the flask and the reaction mixture was allowed to rest in a well-stirred silicon oil heating bath ($T_{\mathrm{Bath}} = 70 - 75\,°\mathrm{C}$) for one day.

The workup and the transfer of the specimen were conducted according to the procedure presented in the paragraph of the "Enhanced Coupling Density through Amino-Terminated Self-Assembled-Monolayers". The specimen was additionally rinsed once with ethyl acetate during the workup. The prior irradiation with low energy electrons (100 eV, $\sim$ 50 $\mathrm{mC\,cm^{-2}}$) was done with a FG 15/40 electron gun at a pressure better than $p < 3.5 \cdot 10^{-8}$ mbar. A silicon (100) wafer piece was used for the transfer of the PMMA-coated CNM. A thick and bare mica substrate was cleaned with ethanol from both sides, cleft in the middle and immersed into Millipore water to get rid of attached particles. The processed CNM was fished onto the freshly cleft mica surface, dried for at least thirty minutes and subsequently cut into several small samples of an appropriate size. By the gentle immersion into Millipore water the CNM detached from the mica and was transferred onto the target silicon nitride window, which exhibits a single orifice and is embedded in solid silicon chips. The Si_3N_4 silicon chips as well as sealed silicon chips were purchased from Silson Limited. The precise diameter of each orifice ($d \sim 7$ µm) was determined in advance through the survey of the taken respective HIM images with ImageJ 1.52a [77]. The specimen was allowed to dry over night.

A metal cylinder exhibiting outlets placed laterally at the bottom and an inlet at the top was set into a beaker. An acetone-resistant tube was plugged into the upper inlet and the end was put into another beaker. The elevated cylinder-containing beaker was filled with acetone, which was sucked through the tube into the second beaker. The acetone levels equalize due to the difference in the hydrostatic pressure. Several samples have been placed into a specifically designed specimen holder and the holder was put onto the cylinder. The sample-containing beaker was lowered and the other one was elevated leading to the complete immersion of the samples in acetone and to the dissolution of the PMMA. After one hour the procedure was reversed and the bare CNM specimens were allowed to dry.

The design of the utilized permeation cell and the procedure of mounting the specimen were adapted from Yang *et al.* [10]. Si_3N_4 silicon chips with a non-covered orifice and sealed silicon chips were used for the reference diffusion experiments and the investigation of the outgassing, respectively. An aqueous Tris-EDTA buffer (TE) solution at pH = 7, made from tris(hydroxymethyl)aminomethane (Tris, $\geq$ 99 %, Fisher Chemical) and ethylenediaminetetraacetic acid (EDTA, $\geq$ 99 %, Carl Roth GmbH & Co), was used to replace the 2-propanol in the compartments of the permeation container. Hydrogen-3 (^3H, tritiated water), carbon-14 (^{14}C, sodium bicarbonate) and phosphorus-32 (^{32}P, phosphoric acid) were bought from Hartmann Analytic GmbH. The corresponding amount of TE buffer solution with respect to the added volume of the tracer molecules and $V = 12.5$ µl of the overlaying mineral oil (M8410, CAS 8042-47-5, Sigma Aldrich) was removed from the donor and acceptor side. The donor compartment of the permeation cell was carefully mixed after the addition of the radioactive material. Two sets of experiments have been performed independently, one containing ^{3}H and ^{32}P and the other one ^{14}C and ^{32}P. Initial activities of $A(^{3}\mathrm{H}) = 2$ µCi, $A(^{14}\mathrm{C}) = 6$ µCi and $A(^{32}\mathrm{P}) = 1$ µCi were used for the diffusion experiments. The outgassing experiments contained only carbon-14 with starting activities of $A(^{14}\mathrm{C}) = 2, 4, 6, 8, 10$ µCi. The data acquisition was realized as follows. A volume of $V = 5$ µl was pipetted from the respective compartment and an amount of $V = 2.5$ ml of the LSC universal scintillation cocktail Rotiszint® eco plus from Carl Roth GmbH & Co. KG was added. The detection of the counts caused by the radioactive decay was done by utilizing a 1900 CA Tri-Carb liquid scintillation (Packard Instrument Company Incorporated) over a time period of ten minutes. The solution in both compartments was overlayed with mineral oil after the first taken data point. The following time-dependent concentrations of the radioisotopes were obtained in the same manner without the addition of extra mineral oil.

Fundamental Feasibility Check. An Au(300 nm)/mica composite from Georg Albert PVD-Coatings was utilized as a substrate. The cleaning of the substrate followed the reported method described in the paragraph of the "Complex Formation with L-Lysine-NTA". The following alkanethiols have been used after they reached room temperature: 1-Dodecanethiol (DDT, $\geq 98\,\%$, Aldrich Chemistry), 1-tetradecanethiol (TDT, $\geq 98\,\%$, Sigma Aldrich), 1-hexadecanethiol (HDT, 99 %, Sigma Aldrich), 1-octadecanethiol (ODT, 98 %, Sigma Aldrich) and 1-docosanethiol (DST, $\geq 98\,\%$, Tokyo Chemical Industry Co., Ltd.). The SAM was formed by the immersion of the cleaned composite into a 1 mM solution of the respective alkanethiol for one day. For HDT the concentration was 4 mM due to the spontaneous melting of the compound. To dissolve the DST molecules a treatment with an ultrasonic bath was necessary. The specimen was rinsed with ethanol, blown dry with nitrogen and stored under an argon atmosphere. The DST sample was additionally rinsed with n-hexane (analytical reagent grade, Fisher Scientific) to remove physisorbed molecules from the surface. The irradiation with low energy electrons (50 eV, 50 $\mathrm{mC\,cm^{-2}}$) was performed in the XPS system. The transfer of the samples followed the procedure described in the paragraphs of the "Enhanced Coupling Density through Amino-Terminated Self-Assembled-Monolayers" for DDT, TDT, HDT and DST and of the "Aqueous Diffusion Coefficients Determined by Radioactive Tracers" for ODT. The removal of the PMMA was done like reported in the last paragraph.

The samples for the conducted ODT's control experiments have been fabricated in principle in the same manner like above, but were irradiated within the system which is equipped with a FG 15/40 electron gun (100 eV, $\sim 50\,\mathrm{mC\,cm^{-2}}$) at a pressure of $p < 5.5 \cdot 10^{-8}$ mbar.

Detailed Study of 1-Octadecanethiol (ODT). The preparation and transfer of the samples was done like it is described in the previous paragraph of the "Fundamental Feasibility Check". The samples were irradiated with a FG 15/40 electron gun (100 eV, $\sim 50\,\mathrm{mC\,cm^{-2}}$) at a pressure of $p < 6.6 \cdot 10^{-8}$ mbar.

In the process of the fabrication of the samples for the SEM and TEM analyses 20 µl trifluoroacetic acid (TFA, $\geq 99\,\%$, Fisher Scientific) were added due to temporary copper contamination issues. However, it was validated that the TFA has no influence on the resulting ODT SAM itself. The samples were transferred onto TEM finder grids (R3.5/1, Au NH7 Quantifoil, Quantifoil Micro Tools GmbH). In this case, the imaging was done with a SEM, because the preferred HIM was under maintenance.

The substrate for the structural AFM investigation was cut into an octagonal shape with a diameter of $d \sim 8\,\mathrm{mm}$ and rinsed with ethanol, as well as Millipore water to get rid of remaining particles. The composite was blown dry in a nitrogen stream and immersed into the ethanolic ODT solution. The irradiation was performed inside the utilized AFM. Some specimens for the AFM bulge test were transferred without the additional fishing onto a freshly cleft mica substrate.

The gluing onto the home-made plastic sample holders (bulge test), onto the upper part of the stainless steel cup (gravimetric analysis), and onto the self-made oxygen-free copper holders (gas permeation) has been done with 2-K-epoxy resin adhesive (UHU® Plus Endfest 300, article number: 45735, UHU GmbH & Co. KG) and the samples were allowed to dry at least over night.

Fabrication of Mixed CNMs. The fabrication of the TPT specimen was performed according to the reported method in the paragraph "Aqueous Diffusion Coefficients Determined by Radioactive Tracers" without the additional usage of ethyl acetate. The exchange was performed by the immersion into a 1 mM ethanolic ODT solution. The different exchange times of the TPT SAM were achieved either by the subsequent and cumulative immersion into the exchange solution or by letting the sample rest for the complete period of time. The samples were cleaned with ethanol and blown dry by a nitrogen stream. The transfer was conducted following the reference of the previous paragraph.

C. Derivation of the Radioisotopes' Model

The following model has been developed in cooperation with Riko Korzetz and the listed symbols were used for the derivation of the radioisotopes' model.

C_D, C_A: concentrations in the donor and acceptor compartments at the membrane's surface, respectively
k: outgassing constant
D': apparent diffusion coefficient
K_L: liquid phase sorption coefficient
D: diffusion coefficient
A: effective diffusion membrane area
V: compartment volume
d: thickness of the membrane
C_0: concentration in the donor compartment at $t = 0$
f: correction factor
$C_{D,0}, C_{A,0}$: bulk concentrations in the donor and acceptor compartments, respectively
F, F_Ref: flux over the membrane and the open orifice, respectively
$C_{D,Ref}, C_{A,Ref}$: concentrations in the donor and acceptor compartments at the orifice's surface, respectively
a: radius of the orifice
Q: flow rate

Further subscripts

Int: intact part of the carbon nanomembrane
Def: defective part of the carbon nanomembrane
Tot: complete specimen
CNM: carbon nanomembrane itself
Obs: experimentally observable parameters

The time-dependent change in the concentration of the radioisotopes can be described by the combination of their corresponding diffusive and outgassing behavior as shown in equation (C.1). The tracer loss and the diffusive transport through the orifice are represented by the first and second term, respectively. When taking a look at the acceptor compartment, which is defined to be left-sided in this case, the algebraic sign of the equation is positive. It should be noted that D' describes the apparent diffusion coefficient, which is related to the diffusion coefficient D and the liquid phase sorption coefficient K_L within the solution-diffusion model via $D' = D \cdot K_\mathrm{L}$.

$$\frac{\mathrm{d}C_\mathrm{A/D}}{\mathrm{d}t} = -kC_\mathrm{A/D} \pm D' \frac{\partial C}{\partial x} \cdot \frac{A}{V} \tag{C.1}$$

The concentration difference across the orifice can be expressed as displayed in equation (C.2) assuming a linear concentration gradient across the membrane.

$$\begin{aligned} \frac{\mathrm{d}(C_\mathrm{D} - C_\mathrm{A})}{\mathrm{d}t} &= -k(C_\mathrm{D} - C_\mathrm{A}) - \frac{2D'A}{V} \frac{\partial C}{\partial x} \\ &\approx -k(C_\mathrm{D} - C_\mathrm{A}) - \frac{2D'A}{V} \frac{C_\mathrm{D} - C_\mathrm{A}}{d} \end{aligned} \tag{C.2}$$

In equation (C.3) the initial values are listed. The initial concentrations equal the one of the added radioisotopes in the donor compartment and zero in the acceptor compartment.

$$\begin{aligned} C_\mathrm{D}(t=0) &= C_0 \\ C_\mathrm{A}(t=0) &= 0 \end{aligned} \tag{C.3}$$

Therewith, a solution of the differential equation (C.2) can be obtained, which is given in equation (C.4).

$$C_\mathrm{A/D} = \frac{C_0}{2}\exp(-kt)\left[1 \mp \exp\left(-\frac{2D'A}{Vd}t\right)\right] \tag{C.4}$$

The concentration differences with respect to the membrane's surface and the bulk are not equal due to the effect of concentration polarization. To account for this effect a correction factor f was introduced as shown in equation (C.5).

$$C_\mathrm{D} - C_\mathrm{A} = f \cdot (C_\mathrm{D,0} - C_\mathrm{A,0}) \tag{C.5}$$

The subsequent paragraphs are devoted to the derivation of the correction factor. Within the solution, the flux through a membrane and an open orifice is proportional to the concentration gradient at every point (Fick's first law). Thus, the concentration difference to the bulk (i.e. the integral of the gradient) is also proportional to the flux. Based on this, the ratio of the fluxes of both systems can be derived from the respective concentration differences regarding to the bulk concentrations as shown in equation (C.6).

$$\frac{F}{F_\mathrm{Ref}} = \frac{C_\mathrm{D,0} - C_\mathrm{D}}{C_\mathrm{D,0} - C_\mathrm{D,Ref}} = \frac{C_\mathrm{A} - C_\mathrm{A,0}}{C_\mathrm{A,Ref} - C_\mathrm{A,0}} \tag{C.6}$$

Consequently, the concentration at the membrane's surface of the different compartments can be expressed like displayed in equation (C.7).

$$\begin{aligned} C_\mathrm{D} &= C_\mathrm{D,0} - (C_\mathrm{D,0} - C_\mathrm{D,Ref})\frac{F}{F_\mathrm{Ref}} \\ C_\mathrm{A} &= C_\mathrm{A,0} + (C_\mathrm{A,Ref} - C_\mathrm{A,0})\frac{F}{F_\mathrm{Ref}} \end{aligned} \tag{C.7}$$

The concentration difference in equation (C.8) results by the subtraction of the former two equations.

$$C_{\mathrm{D}} - C_{\mathrm{A}} = C_{\mathrm{D},0} - C_{\mathrm{A},0} - \left[(C_{\mathrm{D},0} - C_{\mathrm{A},0}) - (C_{\mathrm{D,Ref}} - C_{\mathrm{A,Ref}})\right] \frac{F}{F_{\mathrm{Ref}}} \tag{C.8}$$

The combination of the term for the concentration difference of equation (C.8) with the definition of the correction factor in equation (C.5) yields to equation (C.9).

$$f = \frac{C_{\mathrm{D}} - C_{\mathrm{A}}}{C_{\mathrm{D},0} - C_{\mathrm{A},0}} = 1 - \left(1 - \frac{C_{\mathrm{D,Ref}} - C_{\mathrm{A,Ref}}}{C_{\mathrm{D},0} - C_{\mathrm{A},0}}\right) \frac{F}{F_{\mathrm{Ref}}} \tag{C.9}$$

The strategy for calculating the position-dependent concentration through an orifice (Weber's disc) as it has been introduced in chapter 3, was employed to describe the concentration difference at the orifice's surface for which Radha *et al.* [191] demonstrated its applicability. Cylindrical coordinates have been used for the calculation and the area-averaged concentration gradient provides a simplified expression for the correction factor as shown in equation (C.10) to equation (C.13).

$$\left.\frac{\partial C}{\partial z}\right|_{z=0} = \frac{C_0}{\pi} \frac{1}{\sqrt{a^2 - r^2}} \tag{C.10}$$

$$\frac{\Delta C}{d} \approx \overline{\left.\frac{\partial C}{\partial z}\right|_{z=0}} = \frac{1}{A} \int_0^{2\pi} \int_0^a \left.\frac{\partial C}{\partial z}\right|_{z=0} \mathrm{d}r\mathrm{d}\phi = \frac{2C_0\,a}{A} = \frac{2}{\pi a} C_0 \tag{C.11}$$

$$\frac{C_{\mathrm{D,Ref}} - C_{\mathrm{A,Ref}}}{C_{\mathrm{D},0} - C_{\mathrm{A},0}} = \frac{\Delta C}{C_0} \approx \frac{2d}{\pi a} \tag{C.12}$$

$$f \approx 1 - \left(1 - \frac{2d}{\pi a}\right) \frac{F}{F_{\mathrm{Ref}}} \tag{C.13}$$

The ratio of the fluxes is obtainable from the last determined values of the experiment: The radioisotope's activity in the respective compartment of a specimen measurement is divided through the one of the reference measurement. Thus, the correction factor can be calculated. The final expression for calculating the time-dependent concentration in equation (C.14) originates from the simple modification of equation (C.4) with f.

$$C_{\mathrm{A/D}} = \frac{C_0}{2}\exp(-kt)\left[1 \mp \exp\left(-2f\frac{D'A}{Vd}t\right)\right] \tag{C.14}$$

In order to determine the ratio of the intact and total area of a partially defective specimen, the following approach was developed. It was assumed that the overall flow rate through the sample can be theoretically expressed by the sum of two separate terms as shown in equation (C.15). The first term describes the flow rate through the intact areas of the carbon nanomembrane, whereas the latter one displays it through the defective parts of the specimen. The apparent diffusion coefficients and concentration gradients are considered to be equal to the ones of a totally intact CNM sample for the aforementioned first case and of a reference utilizing an open orifice for the latter one. In this case each area has its own concentration gradient, which does not interfere with the other ones.

Because these gradients are not known, the difference in the concentration gradients was compensated by the usage of the correction factor simplifying them to an unified concentration difference over the membrane's thickness. Or in other words: the gradient across the membrane was calculated with the correction factor and the concentration difference in the bulk as shown above. Furthermore, the defective area can alternatively be written as the difference between the total and intact area.

$$\begin{aligned}
Q &= -\left(A_{\mathrm{Int}} D'_{\mathrm{CNM}} \frac{\partial C_{\mathrm{CNM}}}{\partial x} + A_{\mathrm{Def}} D'_{\mathrm{Ref}} \frac{\partial C_{\mathrm{Ref}}}{\partial x}\right) \\
&= -\left(A_{\mathrm{Int}} f_{\mathrm{Int}} D'_{\mathrm{CNM}} + A_{\mathrm{Def}} f_{\mathrm{Ref}} D'_{\mathrm{Ref}}\right) \frac{\Delta C}{d} \\
&= -\left[A_{\mathrm{Int}} f_{\mathrm{Int}} D'_{\mathrm{CNM}} + \left(A_{\mathrm{Tot}} - A_{\mathrm{Int}}\right) f_{\mathrm{Ref}} D'_{\mathrm{Ref}}\right] \frac{\Delta C}{d}
\end{aligned} \tag{C.15}$$

When performing the measurement with a partially defective specimen its total area is used. By utilizing the same approach like above an overall observable apparent diffusion coefficient, which describes the diffusion through intact and defective parts of the sample, can be determined as displayed in equation (C.16).

$$\begin{aligned}
Q &= -\left(A_{\mathrm{Tot}} D'_{\mathrm{Obs}}\right) \frac{\partial C}{\partial x} \\
&= -\left(A_{\mathrm{Tot}} f_{\mathrm{Obs}} D'_{\mathrm{Obs}}\right) \frac{\Delta C}{d}
\end{aligned} \tag{C.16}$$

Because both descriptions of the flow rate should be equal the rearrangement yields an expression for the ratio of the intact and total area in equation (C.17). The parameters $f_{\mathrm{Ref}} D'_{\mathrm{Ref}}$ and $f_{\mathrm{Int}} D'_{\mathrm{CNM}}$ are known from a reference measurement with an open orifice and from measurements with intact specimens of the same batch, respectively. $f_{\mathrm{Obs}} D'_{\mathrm{Obs}}$ is obtained from the current sample under investigation. The ratio of the sample's defective and total area is consequently given by the subtraction of the ratio $A_{\mathrm{Int}}/A_{\mathrm{Tot}}$ from one.

$$\begin{aligned}
-\left[A_{\mathrm{Int}} f_{\mathrm{Int}} D'_{\mathrm{CNM}} + \left(A_{\mathrm{Tot}} - A_{\mathrm{Int}}\right) f_{\mathrm{Ref}} D'_{\mathrm{Ref}}\right] \frac{\Delta C}{d} &= -\left(A_{\mathrm{Tot}} f_{\mathrm{Obs}} D'_{\mathrm{Obs}}\right) \frac{\Delta C}{d} \\
\frac{A_{\mathrm{Int}}}{A_{\mathrm{Tot}}} &= \frac{f_{\mathrm{Ref}} D'_{\mathrm{Ref}} - f_{\mathrm{Obs}} D'_{\mathrm{Obs}}}{f_{\mathrm{Ref}} D'_{\mathrm{Ref}} - f_{\mathrm{Int}} D'_{\mathrm{CNM}}} \\
\frac{A_{\mathrm{Def}}}{A_{\mathrm{Tot}}} &= 1 - \frac{A_{\mathrm{Int}}}{A_{\mathrm{Tot}}}
\end{aligned} \tag{C.17}$$

D. Scientific Publications and Contributions of the Author

2020 Dalpke, R., Dreyer, A., Korzetz, R., Dietz, K.-J. & Beyer, A. Selective Diffusion of CO_2 and H_2O through Carbon Nanomembranes in Aqueous Solution as Studied with Radioactive Tracers. *The Journal of Physical Chemistry Letters*, Manuscript ID: jz-2020-018217.
Manuscript Status: Submitted (2020).

Riedel, R., Frese, N., Yang, F., Wortmann, M., Dalpke, R., Rhinow, D., Hampp, N. & Gölzhäuser, A. Fusion of Purple Membranes triggered by Immobilization on Carbon Nanomembranes. *Langmuir*, Manuscript ID: la-2020-01902k.
Manuscript Status: Submitted (2020).

2019 Dalpke, R., Dreyer, A., Seidel, T., Beyer, A., Dietz, K.-J. & Gölzhäuser, A. Towards Biomimetic Carbon Nanomembranes. *Poster Contribution*, German Physical Society's Spring Conference of the Condensed Matter Section, Regensburg (2019).

Ahlenhoff, K., Koch, S., Emmrich, D., Dalpke, R., Gölzhäuser, A. & Swiderek, P. Electron-Induced Chemistry of Surface-Grown Coordination Polymers with Different Linker Anions. *Physical Chemistry Chemical Physics* **21**, 2351-2364. `https://doi.org/10.1039/C8CP07028H` (2019).

2017 Wortmann, M., Frese, N., Heide, A., Brikmann, J., Strube, O., Dalpke, R., Gölzhäuser, A., Moritzer, E. & Hüsgen, B. Examination of Interpenetrating Polymer Networks of Polyurea in Silicone Molds Arising during Vacuum Casting Processes. *Polymer-Plastics Technology and Engineering* **57**, 1524-1529. `https://doi.org/10.1080/03602559.2017.1410838` (2017).